arXiv:hep-ph/9910458v2 17 Mar 2000

ANL-HEP-PR-99-102
February 1, 2008

THE TRIANGLE ANOMALY IN TRIPLE-REGGE LIMITS *

Alan. R. White†

High Energy Physics Division
Argonne National Laboratory
9700 South Cass, Il 60439, USA.

Abstract

Reggeized gluon interactions due to a single quark loop are studied in the full triple-regge limit and in closely related helicity-flip helicity-pole limits. Triangle diagram reggeon interactions are generated that include local axial-vector effective vertices. It is shown that the massless quark triangle anomaly is present as a chirality-violating infra-red divergence in the interactions generated by maximally non-planar Feynman diagrams. An asymptotic dispersion relation formalism is developed which provides a systematic counting of anomaly contributions. The asymptotic amplitude is written as a sum over dispersion integrals of triple discontinuities, one set of which is unphysical and can produce chirality transitions. The physical-region anomaly appears in the generalized real parts, determined by multi-regge theory, of the unphysical discontinuities. The amplitudes satisfy a signature conservation rule that implies color parity is not conserved by vertices containing the anomaly. In the scattering of elementary quarks or gluons the signature and color parity of the exchanged reggeon states are such that the anomaly cancels. At lowest-order, it cancels in individual diagrams after the transverse momentum integrations are performed.

---

*Work supported by the U.S. Department of Energy, Division of High Energy Physics, Contracts W-31-109-ENG-38 and DEFG05-86-ER-40272

†arw@hep.anl.gov

1. INTRODUCTION

Multi-regge limits within QCD have the virtue that they are, a-priori, close to perturbation theory at large transverse momentum while in the infra-red transverse momentum region very strong constraints imposed by analyticity and t-channel unitarity must also be satisfied[1, 2]. Many calculations[3]-[9] have shown that if gluons and quarks are given a mass via spontaneous symmetry breaking the unitarity constraints are satisfied perturbatively, in an elegant and minimal manner, by reggeon diagrams containing only reggeized gluons and quarks. If there are circumstances in which the symmetry breaking can be removed smoothly we may hope to see an accompanying transition to reggeon diagrams containing hadrons and the pomeron with, ideally, a connection to perturbation theory maintained at large transverse momentum.

The purpose of this paper is to demonstrate that when quarks are massless many high-order reggeized gluon interactions contain an infra-red divergence that can be understood as the infra-red appearance[10] of the U(1) quark anomaly. Although, of course, QCD contains only vector interactions, in multi-regge limits effective vertices are generated by quark loops which involve products of γ-matrices. The full triple-regge limit[‡] is sufficiently intricate (as are the helicity-flip helicity-pole limits that we also study) that both the axial-vector couplings and the orthogonal momenta needed to generate the triangle anomaly are present. Since triple-regge vertices appear as components in a wide array of multi-regge reggeon diagrams[12] this is a new manifestation of the U(1) anomaly which we believe plays a crucial dynamical role in producing a transition to hadron and pomeron reggeon diagrams.

We present direct calculations[§] showing that the anomaly is present in the triple-regge six-reggeon interaction vertex obtained from the "maximally non-planar" Feynman diagrams that appear in three-to-three quark scattering. These diagrams contain a single quark loop and the anomaly appears because an unphysical singularity combination in which every quark propagator in the loop is on-shell approaches the asymptotic region. The configuration in which one quark in the loop carries zero momentum and undergoes a chirality transition produces the (infra-red) anomaly. There are, however, many obvious possibilities for a cancelation. We have to sum over the different choices for the quark that carries zero momentum, over all diagrams of this kind, and finally, over all other kinds of diagrams as well. While non-planar quark loop diagrams provide the essential analytic structure of regge cut couplings, other diagrams are needed for the reggeon Ward identity cancelations[12] that (indirectly) reflect the underlying gauge invariance. A-priori such cancelations might be expected to include cancelation of the anomaly. However, the reggeon Ward identities include gluon self-interaction contributions that can not produce the chirality transition involved in the anomaly divergence. As a result, reggeon Ward identities are violated by the anomaly and do not prevent it's occurrence. (In an abelian theory the corresponding Ward identities do produce a cancelation.)

[‡] This is a limit of three-to-three scattering amplitudes[11], not to be confused with the incorrectly named "triple-regge" limit of the one-particle inclusive cross-section that is actually a "non-flip helicity-pole" limit.

[§] In a companion paper[13] we present an abbreviated version of the central calculation together with a very brief overview of other arguments in this paper.

Chirality transitions are well-known to be produced by non-perturbative interactions, such as those due to instantons. From the point of view of the dispersion theory on which we ultimately base our analysis, the anomaly appears in the generalized real parts that multi-regge theory provides for perturbatively calculated unphysical asymptotic discontinuities. It is just because the multiple discontinuities are unphysical that they can contain chirality transitions. Our hope is to eventually show that, in appropriate circumstances, the chirality violating processes dominate the soft background to a hard scattering process and, in doing so, provide a fundamental origin for the parton model outside of leading-twist perturbation theory. However, a more immediate property that must first be established is that the chirality violation produced by a single reggeon interaction cancels in elementary scattering processes where it clearly should not appear. This certainly includes helicity conserving processes that have only perturbative QCD ingredients for accompanying interactions and may well extend to any process where the chirality violation can not be linked to (reggeized) gluon configurations with the quantum numbers of the winding-number current.

Since multi-reggeon "states" are virtual, exchanged, configurations that do not directly produce particle states, the chirality and reggeon Ward identity violation associated with the anomaly does not produce any fundamental conflict that requires a cancelation within a reggeon vertex. Rather such cancelations are secondary effects within the full scattering process that have to be traced. The number of Feynman diagrams contributing to even the lowest-order three-to-three quark scattering processes of the kind we study is very large ($O(100)$) and some diagrams, the maximally non-planar diagrams in particular, produce several anomaly contributions. Therefore, even though we make no attempt to calculate the full reggeon interaction vertex, understanding diagrammatically when the anomaly occurs and how and when the necessary cancelations take place would be very difficult.

Fortunately, we are able to systematically count all anomaly contributions by using the asymptotic dispersion relation formalism developed in [2] and [14]. In this formalism the full asymptotic amplitude is constructed as a relatively simple sum over dispersion integrals of multiple discontinuities. Multi-regge theory then allows the multiple discontinuities to be converted to amplitudes containing generalized real parts by introducing appropriate signature factors and, for the lowest-order amplitudes we consider, the signature factors have a particularly trivial form. A very important feature of the asymptotic dispersion relation we use, which is not present in the simpler case of multi-regge production processes, is that there is a set of unphysical triple discontinuities that contribute. Indeed we find that the anomaly appears only in the amplitudes given by multiple discontinuities of this kind obtained from the maximally non-planar diagrams and, also, the closely related diagrams required by reggeon Ward identities. Once the discontinuities involved have been isolated, the study of cancelations reduces to a discussion of signature and the symmetry properties of color factors.

The amplitudes that contain the anomaly have special analytic properties. In particular, they satisfy a very important signature conservation rule. (Although we do not discuss it in this paper, we expect this rule to lead to the even signature of the pomeron in hadronic reggeon diagrams.) The signature rule implies that the anomaly chirality transition be accompanied by a color parity violation and, most likely, requires that all reggeon states coupling to the anomaly carry anomalous color parity (not equal to the signature). For color zero reggeon states, anomalous color parity implies the quantum numbers of the winding-number current for either the complete state or a sub-component. In addition, color parity violation by the anomaly vertex requires a symmetric d-tensor and so requires at least SU(3) for the gauge group. When the external scattering states are elementary quarks (or gluons) anomalous color parity reggeon states can not appear and the anomaly cancels. At lowest-order, it cancels in individual diagrams after the transverse momentum integrations are performed.

Far more important, of course, is determining when the anomaly does not cancel. For high-order multi-regge amplitudes that have clusters of particles in initial and final states there is, as we briefly elaborate in Section 7, no reason for anomalous color parity reggeon states and the anomalous reggeon interactions to cancel and they are likely to be a pervasive phenomenon. However, the infra-red divergences are then suppressed by Ward identity zeroes of the accompanying interactions. Nevertheless, the associated ultra-violet effects of the anomaly should not be suppressed and we expect the consequence to be a power (rather than a logarithmic) violation of unitarity bounds.

Avoiding the violation of unitarity by the anomaly is, we believe, the core problem in finding the full multi-regge S-Matrix of QCD. Our proposal, outlined in [2], is that this can be achieved by enhancing the anomaly in the infra-red region so that the ultra-violet effects are dominated by infra-red divergences that can be absorbed into the definition of reggeon states. To achieve this is very subtle. The anomaly does produce infra-red divergences if an anomalous color parity "reggeon condensate" (with the quantum numbers of the winding-number current[¶]) is introduced. In the program outline we gave previously[12] we demonstrated that in a color superconducting phase of QCD (with the gauge symmetry broken from SU(3) to SU(2)) such a condensate can be consistently reproduced in all reggeon states by anomaly infra-red divergences. We also showed how the perturbative reggeon diagrams are replaced by diagrams containing hadrons and a Reggeon Field Theory (RFT) supercritical pomeron[2], with restoration of the full SU(3) symmetry producing, in principle, the RFT critical pomeron[15].

In [12] we assumed the existence of the anomaly. While the properties we assumed were essentially correct there are significant differences. Having understood the full structure of the anomaly we hope to implement our previously outlined program in detail in future papers. If we successfully obtain a unitary (reggeon) S-Matrix as we hope, it will be very close to perturbation theory, and the connection with the parton model should be clear. In effect, the non-perturbative properties of confinement and chiral symmetry breaking will be obtained as a consequence of regulating the anomaly so that unitarity is satisfied in the regge region.

In this paper, apart from brief discussions in Sections 2 and 7, we will not enlarge on what we believe to be the dynamical role of the anomaly divergences. Instead we will focus entirely on the technical problem of studying the asymptotic behavior of Feynman diagrams, setting up the necessary multi-regge formalism, and isolating the occurrence of the anomaly. We have organized the paper in a manner that we hope will allow a reader to extract some general understanding of our results without necessarily absorbing all of the underlying multi-regge theory. Section 2 is a general outline of the purpose of the paper and a summary of it's contents that, as far as possible, avoids technical language. Section 3 describes the triple-regge and related helicity-pole limits in terms of light-cone variables. Section 4 is devoted to the calculation, using light-cone co-ordinates, of triple-regge contributions from three specific diagrams. This allows us to illustrate how the anomaly occurs as an infra-red divergence of reggeon vertices. We concentrate on the kinematic structure of diagrams and ignore color factors until we have set up the necessary machinery to discuss cancelations. We study one diagram that obviously does not contain the anomaly, one that might have anomaly contributions but actually does not and one, a maximally non-planar diagram, that does. At the end of the Section we discuss how the anomaly contributions from maximally non-planar diagrams cancel. In Section 5 we develop the asymptotic dispersion relation and multi-regge formalism that ultimately allows us to systematically discuss all anomaly contributions. In Section 6 we study the complete set of double discontinuities and conclude that only those originating from maximally non-planar diagrams, and diagrams closely related by reggeon Ward identities, give amplitudes that contain the anomaly. We finally discuss the role of color factors in cancelations in Section 7. We then briefly discuss diagrams which give anomaly contributions that we do not expect to be canceled.

[¶] This "condensate" is actually a "wee-parton" contribution in a physical reggeon state, rather than a vacuum condensate and so need not be parity violating, as a true vacuum winding-number condensate surely would be.

2. OUTLINE AND SUMMARY

The triple-regge limit (and closely related helicity-flip helicity-pole limits[‖]) can be formulated as the high-energy, near-forward, scattering of three particles carrying light-like momenta P_1, P_2 and P_3 whose spacelike components are orthogonal to each other. This limit (defined precisely in the next Section) is discussed in [12] for some simple diagrams but otherwise has not been discussed in QCD. In this paper we will study Feynman diagrams of the kind illustrated in Fig. 2.1 in which the three particles scatter via gluon interactions involving a single quark loop - the solid circle.

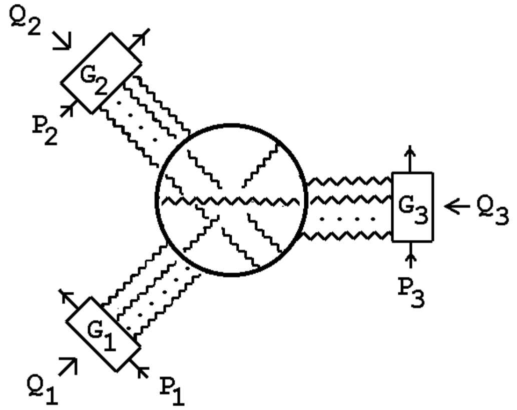

Fig. 2.1 The Class of Feynman Diagrams Studied

In most of our discussion the scattering particles will be single quarks and the couplings G_1, G_2 and G_3 will be the lowest-order elementary couplings. However, in discussing anomaly cancelations we will also allow these couplings to have more general properties, including the production and/or absorption of additional particles.

The quark loop initially contains a sufficiently large number of quark propagators that there are no ultra-violet divergences. At finite momentum, this loop also has no infra-red divergences, even when the quark mass is zero. If the gluons are massive, the gluon loops also have no divergence problems. For most of our analysis we will, for simplicity, set the gluon mass to zero. This means that the diagrams we study will formally have infra-red divergences at zero gluon transverse momentum, just where the anomaly divergence occurs. Ultimately the interplay between these divergences is crucial and has to be discussed in detail. (It is well-known that the gluon infra-red divergences cancel for reggeon states carrying zero t-channel color but do not produce confinement.) In Section 4 we will briefly mention using gluon mass(es)

[‖] A helicity-pole limit isolates the leading helicity amplitude that ultimately gives a physical particle amplitude.

to avoid anomaly cancelations. In the main body of the paper we simply ignore the divergences due to the zero mass of the gluon.

In the limits we consider the most important contributions come from regions of the gluon loop integrations where a number of the propagators in the quark loop and the scattering quark systems are either on-shell or close to on-shell. We will be particularly interested in diagrams for which, with appropriate quantum numbers in the t_i $(= Q_i^2)$ channels, all the relevant quark lines are precisely on-shell in the leading contribution. (We discuss below which propagators are involved.) If the propagator poles are used to carry out light-cone longitudinal momentum integrations the integrals over gluon loop momenta reduce to two-dimensional "transverse momentum" integrals. The leading contribution then has the form

$$\begin{aligned} P_{1+}\ P_{2+}\ P_{3+}\ \prod_{i=1}^{3} \int \frac{d^2k_{i1}d^2k_{i2}\ \cdots \delta^2(Q_i - k_{i1} - k_{i2} - \cdots)\ G_i(k_{i1}, k_{i2}, \cdots)}{k_{i1}^2 k_{i2}^2\ \cdots} \\ \times\ R(Q_1, Q_2, Q_3, k_{11}, k_{12}, \cdots) \end{aligned} \tag{2.1}$$

(Note that, in contrast to simpler multi-regge limits, the transverse momenta in each integral can not be taken to be in a common plane.)

Provided that $\alpha_i = 1 +\ O(g^2),\ i = 1, 2, 3$ we can write

$$\begin{aligned} P_{1+}\ P_{2+}\ P_{3+}\ &\sim\ S_{12}^{1/2}\ S_{23}^{1/2}\ S_{31}^{1/2} \\ &=\ (s_{13})^{(\alpha_1+\alpha_3-\alpha_2)/2}(s_{23})^{(\alpha_2+\alpha_3-\alpha_1)/2}(s_{12})^{(\alpha_1+\alpha_2-\alpha_3)/2}\ +\ O(g^2) \end{aligned} \tag{2.2}$$

where $S_{ij} = (P_i + P_j)^2$. This is the lowest-order triple-regge behavior for the amplitudes that interest us (and, in particular, potentially contain the anomaly). Consequently, the transverse momentum integrations, together with the gluon propagators and the external couplings G_i, are straightforwardly interpreted as the leading-order contribution of multi-reggeon states in which each gluon is regarded as a lowest-order reggeon. As illustrated in Fig. 2.2,

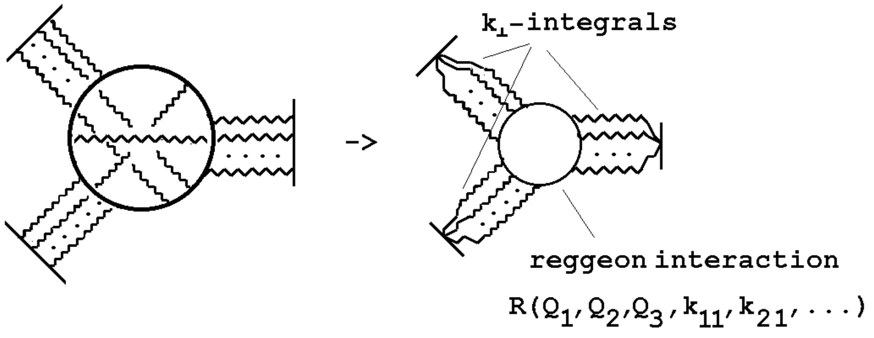

Fig. 2.2 Generation of a Reggeon Vertex

$R(Q_1, Q_2, Q_3, k_{11}, k_{21}, \cdots)$ can then be extracted as a "reggeon interaction vertex". In general, the lowest-order contribution to this vertex will survive as higher-order corrections add reggeization effects to the exchanged gluons and modify the G_i couplings. In particular if there is an infra-red divergence in the lowest-order vertex this would also be expected to survive as higher-order effects are added. Reggeon vertices appear in the reggeon diagrams describing a wide range of high-energy multi-regge processes[12]. Therefore the general structure of such vertices is very important. In particular any divergences that are present may have a dynamical significance going far beyond the low-order circumstances in which we initially discover them.

Since one propagator in the quark loop is placed on-shell for each gluon loop integration, only three of the original loop propagators are off-shell. The effective vertices produced by the longitudinal integrations contain, in general, both local and non-local components. By (our) definition, the local components are products of γ matrices that in some cases reduce to $\gamma_5\gamma$ couplings. Clearly, if there is an odd number of γ_5's then, a-priori, the U(1) triangle anomaly could be present in the reduced loop. Intrinsically, reggeon diagrams are most unambiguously defined at low transverse momentum. Therefore, we look for the infra-red manifestation of the anomaly as a divergence that is present when the quark mass vanishes[10]. This divergence requires that the remaining three off-shell quarks go on-shell (producing a complete loop of on-shell quarks). We will not be able to identify the full Lorentz structure but we will find the characteristic chirality violation. (At the end of Section 5 we identify the origin of the unphysical singularity configuration of on-shell quarks that is able to produce the chirality violation.) Note that analyticity properties of reggeon vertices imply that if the anomaly is present in the infra-red then it should also be present as an ultra-violet effect. We briefly discuss the nature and potential significance of such ultra-violet effects in Section 7.

Gauge-invariance relates diagrams of the form of Fig. 2.1 to other diagrams involving the triple-gluon coupling. We will make brief references to such diagrams in the context of reggeon Ward identity cancelations. However, we do not attempt to calculate reggeon vertices corresponding to all diagrams of a fixed-order. Rather we concentrate on demonstrating the presence of the anomaly in contributions from particular diagrams and on determining when and how such contributions cancel. The infra-red divergence we are looking for requires[10] a quark triangle Landau singularity and so diagrams of the kind we have isolated are the important ones. Most of our discussion will be concerned with the lowest-order diagrams, illustrated in Fig. 2.3, in which the scattering states are quarks and there are just two-gluons exchanged in each t-channel. This simplest set already contains $O(100)$ diagrams and so counting all possibilities will be a very difficult thing to do unless we have a very systematic procedure.

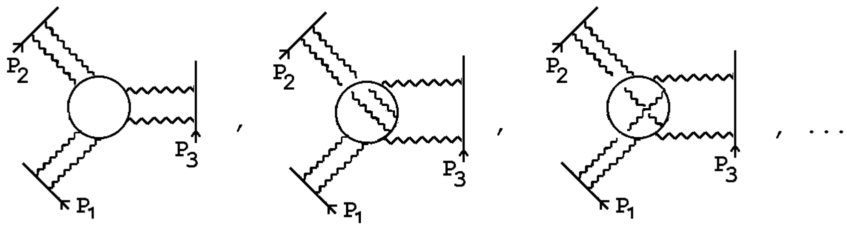

Fig. 2.3 Quark Scattering Diagrams with Two Gluons in each t_i-channel.

Two conceptually distinct calculational methods can be used to arrive at (2.1). The arguments for placing propagators on-shell are related but differ in important ways that we want to emphasize. The most popular calculational method is applied directly to Feynman diagrams and utilises light-cone co-ordinates (or Sudakov parameters). The large light-cone momenta are routed through a diagram and if a large momentum is carried by a propagator it must be on-shell, or close to on-shell, if it is not to (power) suppress the asymptotic behavior. If there is no corresponding intermediate state in which the propagator is on-shell then, in a leading-log calculation, only the close to on-shell configuration contributes and a real logarithm is generated. In high-orders a careful discussion of the closing of longitudinal integration contours in the complex plane is required, to make sure that the propagator pole involved can not be avoided by the distortion of an integration contour. In general, the contribution of a real, close to on-shell, configuration reflects the presence of a cross-channel branch-cut.

The second, much less intuitive, calculation method employs a dispersion relation[3] which contains discontinuities in which the relevant lines are specifically on-shell. Real amplitudes involving logarithms corresponding to close to on-shell configurations in a particular channel are reproduced by dispersion integrals over the intermediate states in the cross-channel that they are related to. The dispersion relation formalism generally has the advantage (particularly in a gauge theory) that fewer diagrams need to be calculated. In higher-orders, in principle, dispersion relations for production amplitudes must also be introduced. However, the simple relationship between the signature factors and discontinuities for regge amplitudes can be exploited[8] to short-cut, at least part of, such calculations. The dispersion relation approach sometimes has the disadvantage that a cancelation which manifests itself via the closing of a contour in the direct diagrammatic approach can appear as a more elaborate cancellation between discontinuities, dependent on signature and quantum number properties. For our purposes, however, the crucial feature of the dispersion relation method is that the ambiguity of which on-shell configurations contribute is resolved by the unambiguous process of taking the necessary discontinuities.

As we already implied, because we are interested in the low-order behavior of a large number of relatively complicated diagrams we will not attempt a complete diagrammatic analysis. In fact, although there are three distinct large momenta to be routed through diagrams, in the configuration that interests us the crucial quark loop carries finite momentum. This makes the ambiguity as to which quark propagators should be placed on-shell particularly serious. Fortunately, the asymptotic dispersion relation formalism developed in [2] and [14] provides a fundamental basis for calculating triple discontinuities and assembling them to form the complete asymptotic amplitude. We will see that the structure of multiple discontinuities, although involving subtleties crucial for the emergence of the anomaly, is relatively simple and that the problem of counting contributions from all diagrams becomes straightforward. Indeed, when the amplitude is regge-behaved, the relationship between discontinuities and the full amplitude is such that reggeon interaction vertices can be extracted from multiple discontinuities directly. The most important subtlety, for our purposes, is that the dispersion relation includes unphysical discontinuities that can contain the chirality transitions necessary for the anomaly to appear. In fact this feature can be regarded as the main consequence of the increased complexity of the triple-regge limit, compared to the multi-regge limits previously studied.

To illustrate the general idea behind using multi-regge theory to obtain amplitudes from multiple discontinuities we note that when the leading-order amplitude has the form of (2.1) discontinuities can be taken trivially using (2.2)

$$[Disc]_{s_{12}} \ \sim \ (s_{12})^{1/2} \ - \ (e^{-2\pi i} s_{12})^{1/2} \ = \ 2(s_{12})^{1/2} \tag{2.3}$$

Indeed if (2.1) were derived** as an asymptotic multiple discontinuity in s_{12}, s_{23} and s_{31} and the momentum behavior interpreted using (2.2), the asymptotic result has a trivial extension away from the discontinuity by including the phases due to the square-root branch-cuts in each of s_{12}, s_{23} and s_{31}. In particular the amplitude can be extended to negative values of the invariants where the amplitude is real and there are no discontinuities. Of course, (2.2) is only one possible way to write the large momentum factor $(P_{1+}P_{2+}P_{3+})$ in terms of large invariants. To justify this particular choice it is necessary to calculate higher-order corrections and see the appropriate reggeization effects appear. The asymptotic dispersion relation provides a sum over all allowed possibilities and multi-regge theory incorporates the higher-order corrections and generalizes the extension of the amplitude away from the discontinuities via the introduction of phases and signature factors.

As part of our effort to organize the paper to provide some benefit for a general reader we begin, in Section 3, by formulating the triple-regge limits we discuss in terms of light-cone kinematics. As a result, in Section 4 we are able to initially discuss some diagrams directly in terms of light-cone co-ordinate calculations without developing the multiple discontinuity formalism. This allow us to illustrate how the anomaly

---

[**] This particular multiple discontinuity is forbidden by the Steinmann relations, but for pedagogical reasons we ignore this for the moment.

occurs. We study all three diagrams shown explicitly in Fig. 2.3. As described in Appendix A, the anomaly appears as an infra-red divergence of the triangle diagram when an odd number of axial-vector couplings is present and a lightlike momentum and orthogonal spacelike momenta flow through the diagram - with the spacelike momentum scaled to zero. The first diagram of Fig. 2.3, fairly obviously, does not contain the anomaly since it generates only vector effective vertices. The second diagram contains a γ_5 effective vertex, but the necessary light-like momentum can not flow through the diagram. This illustrates the general point that, while several diagrams generate quark triangle reggeon vertices with the necessary effective axial-vector couplings, in most cases the longitudinal integrations produce additional effects that either prevent the occurence of the divergence, or lead to a cancelation.

The third diagram of Fig. 2.3 actually gives more than one reggeon interaction contribution containing the anomaly. When this diagram is redrawn as in Fig. 2.4,

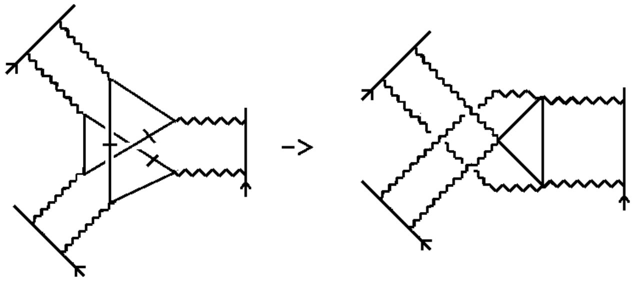

Fig. 2.4 A Diagram with an Anomaly Contribution.

the "maximally non-planar" property is apparent. (The couplings to the quark loop by the two gluons in the same t-channel are separated, in both directions around the loop, by couplings to gluons in the other two t-channels.) As we already alluded to above, this non-planarity property ensures that such diagrams unambiguously contribute to regge cut vertices. When the hatched lines are placed on-shell by the gluon loop longitudinal integrations a triangle diagram reggeon interaction is generated as shown. The local coupling component is shown in Fig. 2.5.

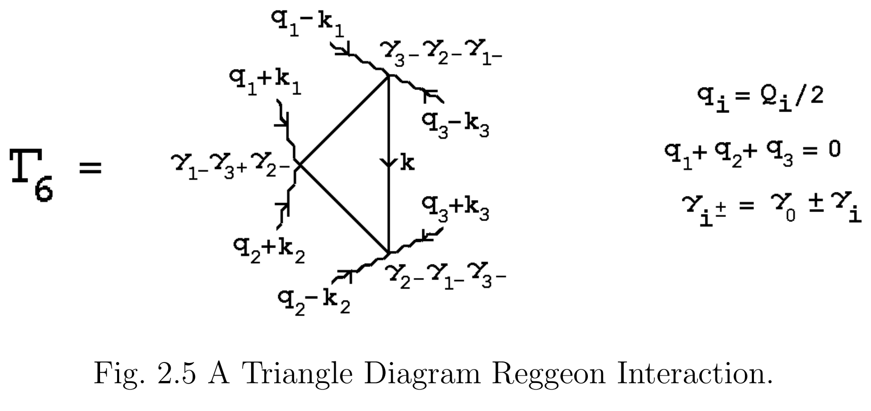
T_6 =
q_1-k_1
$\gamma_3-\gamma_2-\gamma_1-$
q_1+k_1
q_3-k_3
$\gamma_1-\gamma_3+\gamma_2-$
k
q_3+k_3
q_2+k_2
$\gamma_2-\gamma_1-\gamma_3-$
q_2-k_2
$q_i = Q_i/2$
$q_1+q_2+q_3 = 0$
$\gamma_{i\pm} = \gamma_0 \pm \gamma_i$

Fig. 2.5 A Triangle Diagram Reggeon Interaction.

In obtaining these local couplings we have used the special light-cone co-ordinates discussed in Appendix B. It is straightforward to show that the necessary γ_5 couplings are present within the products of γ-matrices shown.

To illustrate how the appropriate momentum configuration for the anomaly appears we first define the light-like vector

$$\underline{n}_{lc} ~=~ (1, cos\theta_{lc}~, sin\theta_{lc}~, 0) \tag{2.4}$$

and the orthogonal space-like vector

$$\underline{n}_{lc\perp} ~=~ (0, -sin\theta_{lc}~, cos\theta_{lc}~, 0) \tag{2.5}$$

We then take

$$\begin{aligned} q_1 + k_1 + q_2 + k_2 ~&=~ O(\mathsf{q})~\underline{n}_{lc\perp} \\ q_2 - k_2 + q_3 + k_3 ~&=~ l~\underline{n}_{lc} ~+~ O(\mathsf{q})~\underline{n}_{lc\perp} \\ q_1 - k_1 + q_3 - k_3 ~&=~ -~l~\underline{n}_{lc} ~+~ O(\mathsf{q})~\underline{n}_{lc\perp} \end{aligned} \tag{2.6}$$

We also take the loop momentum $k \sim O(\mathsf{q})$ and let $\mathsf{q} \to 0$ with

$$(q_1 - k_1) ~\to~ -~2l~(1,1,0,0)~, \qquad (q_2 - k_2) ~\to~ 2l~(1,0,1,0)~, \tag{2.7}$$

and

$$q_3 ~\to~ l~(0, 1-1, 0)~, \qquad k_3 ~\to~ l~(0, 1 - 2cos\theta_{lc}~, 1 - 2sin\theta_{lc}~, 0) \tag{2.8}$$

In the limiting configuration the momenta corresponding to the hatched lines of Fig. 2.4 are on-shell. Also

$$q_1^2 ~=~ q_2^2 ~=~ k_1^2 ~=~ k_2^2 \tag{2.9}$$

and only the lightlike momentum $k_{lc} ~=~ l~\underline{n}_{lc}$ flows through the triangle graph of Fig. 2.5. As a result, the anomaly divergence appears and gives

$$\Gamma_6 ~~\sim~~ \frac{(1 - cos\theta_{lc} - sin\theta_{lc})^2~l^2}{\mathsf{q}} \tag{2.10}$$

The momentum configuration (2.7) and (2.8) describes the physical scattering process illustrated in Fig. 2.6(a), where the time axis is vertical on the page. Fig. 2.6(a) is the basic process associated with the anomaly in the reggeon vertices obtained from the lowest-order graphs. The dashed lines indicate light-like ("wee parton") gluons, one incoming produced by an incoming quark and one outgoing that is absorbed by an outgoing quark. A zero-momentum quark (indicated by the open line) is emitted by the incoming wee-parton gluon, undergoes a chirality transition, and then is absorbed by the outgoing wee-parton gluon. The accompanying antiquark has it's incoming light-like momentum pointed along $\underline{n}_{lc}$ by scattering off a spacelike gluon. It then forward scatters off two more spacelike gluons before another scattering points it's lightlike momentum in the outgoing direction.

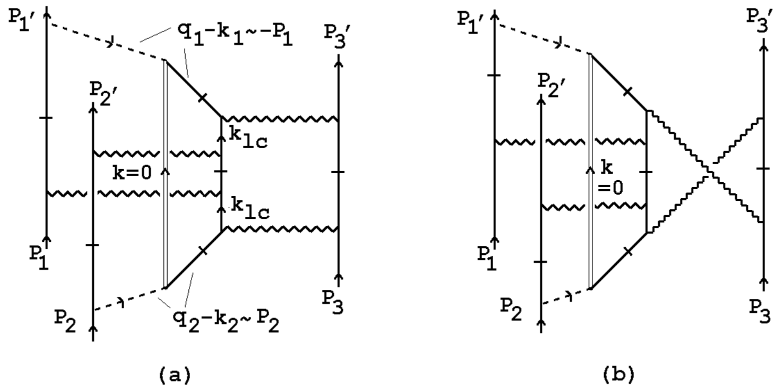

Fig. 2.6 Physical Scattering Processes Involving the Anomaly

c

The hatched lines are put on-shell in extracting the reggeon interaction. In the momentum configuration we have given, the hatched light-like antiquark states necessarily give the γ-matrix couplings shown in Fig. 2.5. However, it is clear from Fig. 2.6(a) that there is no physical intermediate state in the scattering process to which the corresponding on-shell propagators can contribute. It is essential that the amplitude with these lines on-shell is obtained by using multi-regge theory to extrapolate an amplitude away from an (unphysical) multiple discontinuity as we discussed above. That the initial and final quark/antiquark pair can have the net chirality due to effective axial couplings can be regarded as a consequence of the hatched lines having been placed on-shell in an unphysical region.

That the divergence occurs at $(q_1 - k_1)^2 = (q_2 - k_2)^2 = 0$ implies that it mixes with several other effects. Firstly, it mixes with the infra-red divergences due to the zero mass of the gluon that, in this paper, we are ignoring. More interesting are reggeon Ward identity zeroes that should occur in the reggeon vertex. The derivation[12] of the identities giving these zeroes combines regge pole factorization with the underlying gauge invariance Ward identities. Provided there are no transverse momentum singularities of the reggeon vertex involved, the zeroes should occur at $(q_1 - k_1)^2 = 0$ or $(q_2 - k_2)^2 = 0$, independent of any light-like momenta that are present. The zeroes result from cancelations that might be expected to also cancel the anomaly. As we have emphasized, the anomaly divergence can only be canceled by interactions that also contain the same quark loop divergence.

As we discuss in more detail in Section 6, the diagram giving the space-time scattering of Fig. 2.6(b) also contains the anomaly, and in an abelian theory would produce the Ward identity zeroes. Without color factors these two diagrams cancel, as required, at $(q_1 - k_1)^2 = 0$ and $(q_2 - k_2)^2 = 0$. Since the two diagrams have identical kinematic structure, this cancelation will include the anomaly. With color factors, however, the two wee-parton gluons can form a color octet state and in this case the two diagrams of Fig. 2.6 do not cancel. As illustrated in Fig. C6, the desired reggeon Ward identity is produced by the addition of a diagram in which an interaction involving the triple gluon coupling replaces the zero momentum quark exchange. The triple gluon diagram can not, however, produce the chirality transition of the anomaly and so the reggeon Ward identity necessarily fails when the light-like momentum configuration giving the anomaly dominates. When the external couplings G_1,G_2 and G_3 involve multiparticle states they also contain Ward identity zeroes that (unless they also contain the anomaly) will not be sensitive to the light-like momenta. We briefly discuss in Section 7 how, in this case, it can be that the anomaly does not cancel but the zeroes in the G_i suppress the infra-red divergence effects. The effects of the anomaly are then, primarily, in the ultra-violet transverse momentum region.

In lowest-order, although the reggeon Ward-identity fails so that the anomaly is present in the reggeon vertex, there is actually a relatively simple cancelation within each maximally non-planar Feynman diagram. In the diagram of Fig. 2.4, we could equally well place on-shell the lines that are hatched in the diagram of Fig. 2.7.

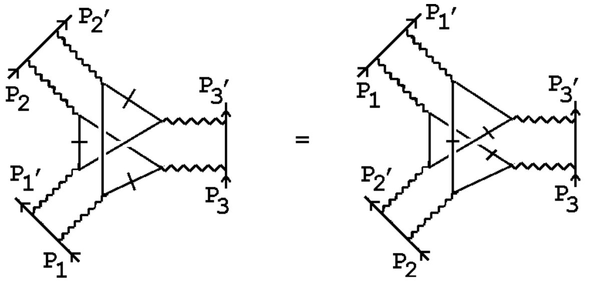

Fig. 2.7 An Alternative Set of On-shell Lines.

As we have shown in the figure, this new set of hatched lines can be related back to the original set simply by interchanging the role of P_1 and P_2, together with $k_1 \to -k_1$ and $k_2 \to -k_2$. In the process of Fig. 2.6 the incoming and outgoing wee parton gluons are correspondingly interchanged. As we discuss in Section 4, the interchange of the roles of 1 and 2 (together with $k_1 \to -k_1$ and $k_2 \to -k_2$) can be viewed as a parity transformation that produces a change of sign of the anomaly. However, the rest of the reggeon diagram is kinematically insensitive to this transformation. The large momentum factors also do not change sign and so if the color factors are appropriately symmetric, after the transverse momentum integrations are performed, there will be a cancelation between the two anomaly contributions. More generally, a cancelation is obtained after all maximally non-planar diagrams are added together. If the anomaly is canceled in the maximally non-planar diagrams then, as we discuss further in Section 6, the reggeon Ward identities ensure it's complete cancelation.

We can give an illustration of the physical amplitudes that we anticipate the anomaly divergence ultimately produces, and the relation to the parton model, as follows. The divergence (2.10) appears in the full triple-regge vertex. If amplitudes involving triple-regge vertices of this kind are first selected as reggeon amplitudes, with the anomaly divergence factored off, particle amplitudes will be obtained (essentially) by taking an additional (helicity-flip helicity-pole) limit in which $l \to 0$. In this case all the quarks and gluons in Fig. 2.6, apart from those exchanged in the central scattering, carry zero momentum. In higher-orders, and in appropriate circumstances, combinations of scatterings of the kind illustrated in Fig. 2.8 are produced. A finite momentum "parton scattering" takes place in the background of a zero momentum scattering via the anomaly. The parton scattering will be momentum conserving but will be (a component of) a Lorentz vector.

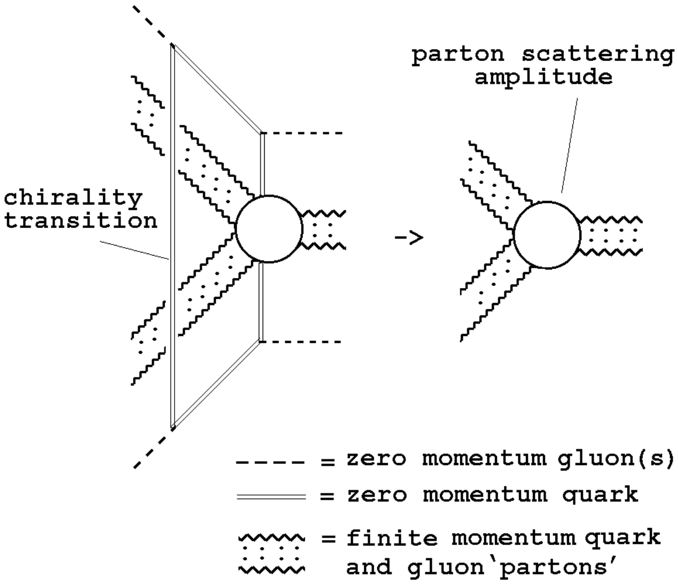
parton scattering amplitude
chirality transition
->
---- = zero momentum gluon(s)
= zero momentum quark
= finite momentum quark and gluon 'partons'

Fig. 2.8 Parton Scattering Within the Anomaly

To truly isolate such scatterings it is necessary to break the SU(3) gauge symmetry of QCD to SU(2). The zero momentum scattering should lie in the unbroken part of the gauge group while the parton scattering lies in the broken part. In addition the zero momentum gluons should carry the quantum numbers of the winding number current in each t-channel. That the reggeon diagrams of unbroken QCD can be constructed from such a starting point is the potential origin of the parton model referred to in the Introduction. In the unbroken theory the direction, within the gauge group, of the zero momentum scattering will be averaged over.

In Section 5 we describe the asymptotic dispersion relation that holds in the triple-regge limit. The physical-region triple discontinuities that appear are relatively simple. Using tree diagrams in which an internal line represents a channel discontinuity, the triple discontinuities are of three kinds.

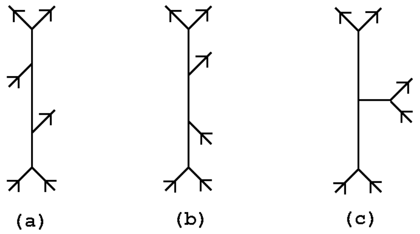

Fig. 2.9 Tree Diagrams for Triple Discontinuities

There are 24 of the first kind, illustrated in Fig. 2.9(a), that are related to one-particle inclusive cross-sections (via optical theorems). There are 12 contributions of the form of Fig. 2.9(b). The asymptotic dispersion relation also contains 12 triple discontinuities of the form of Fig. 2.9(c) which, unlike those of Fig. 2.9(a) and (b), do not occur in any of the physical regions. However, they contribute in a crucial way to the asymptotic behavior and are essential for the appearance of the anomaly.

The multi-regge Sommerfeld-Watson representations are quite different for the triple discontinuities of Fig. 2.9(a) and those of Fig. 2.9(b) and (c). The 24 combinations of the first kind break up into three sets in which the eight making up a set combine to form signatured amplitudes with three possible signatures. Each of the sets of Fig. 2.9(b) and (c) provide only four distinct signatured amplitudes leading to a "signature conservation" rule. This rule is superficially the same as the usual Gribov signature rule for the triple-regge vertices appearing in elastic scattering reggeon diagrams. However, it's origin is quite different. We anticipate that this signature rule will ultimately lead to the even signature property of the pomeron when we finally extract the physical S-Matrix from reggeon diagrams.

A major part of Section 5 is devoted to the hexagraph notation for counting the contribution of multiple discontinuities to the asymptotic dispersion relation. The hatched amplitudes of Fig. 2.4 and Fig. 2.7 correspond to distinct double discontinuities and hence to distinct hexagraphs. Section 6 has a very simple purpose and result. We study all contributions of diagrams of the form of Fig. 2.3 to a particular hexagraph (i.e. to a particular physical region double discontinuity) and look for the anomaly in the contributions to six-reggeon interactions. We show that only the double discontinuities originating from a maximally non-planar diagram give an amplitude that contains the anomaly, apart from the diagram that is closely related to the non-planar diagram by reggeon Ward identities. This implies that to fully discuss the cancelation of the anomaly we only have to add a relatively simple discussion of color factors to our discussion at the end of Section 4. This we do in Section 7. We also discuss processes in which the anomaly does not cancel but rather gives predominant ultra-violet effects.

3. KINEMATICS - TRIPLE-REGGE LIMITS

In order to extract the asymptotic behavior of Feynman diagrams using familiar light-cone techniques, we begin by formulating the triple-regge limits we study using light-cone momenta. In Section 5 we will relate this formulation of limits to the usual description of multi-regge limits in terms of angular variables.

3.1 Light-Cone Description of the Triple-Regge Limit

We consider the three-to-three scattering process illustrated in Fig. 3.1(a) and define momentum transfers Q_1, Q_2 and Q_3 as in Fig. 3.1(b).

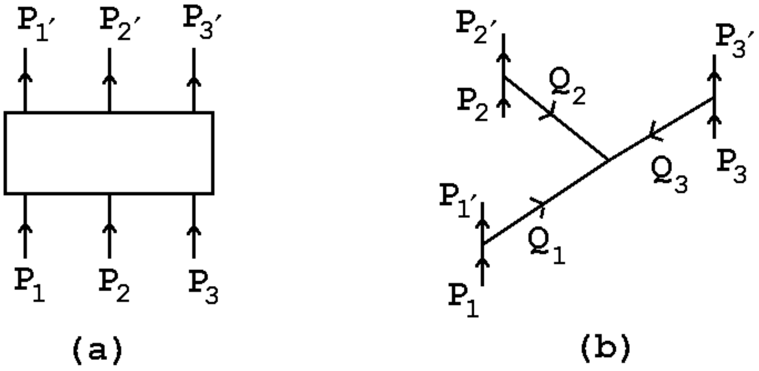

Fig. 3.1 Three-to-Three Scattering.

Consider first the "full triple-regge limit" in which each of P_1, P_2 and P_3 are taken large along distinct light-cones, with Q_1, Q_2 and Q_3 fixed, i.e.

$$\begin{aligned} P_1 &\to P_1^+ = (p_1, p_1, 0, 0)\ , \quad p_1 \to \infty \qquad & Q_1 &\to (\hat{q}_1, \hat{q}_1, q_{12}, q_{13}) \\ P_2 &\to P_2^+ = (p_2, 0, p_2, 0)\ , \quad p_2 \to \infty \qquad & Q_2 &\to (\hat{q}_2, q_{21}, \hat{q}_2, q_{23}) \\ P_3 &\to P_3^+ = (p_3, 0, 0, p_3)\ , \quad p_3 \to \infty \qquad & Q_3 &\to (\hat{q}_3, q_{31}, q_{32}, \hat{q}_3) \end{aligned} \tag{3.1}$$

Momentum conservation requires that

$$\hat{q}_1 + \hat{q}_2 + \hat{q}_3 = 0,\ \hat{q}_1 + q_{21} + q_{31} = 0,\ \hat{q}_2 + q_{12} + q_{32} = 0,\ \hat{q}_3 + q_{13} + q_{23} = 0 \tag{3.2}$$

and so there are a total of five independent q variables which, along with P_1, P_2 and P_3, give the necessary eight variables. (Obviously $P_{i'} = P_i - Q_i,\ i = 1, 2, 3$. Also we omit light-cone components of both the P_i and the Q_i that go to zero asymptotically, but are necessary to put the initial and final particles on mass-shell.)

In terms of invariants, writing $s_{ij} = (P_i + P_j)^2$, $s_{ij'} = (P_i - P_{j'})^2$ and $s_{i'j'} = (P_{i'} + P_{j'})^2$, the limit (3.1) gives

$$\begin{aligned} &s_{12} \sim s_{1'2'} \sim -s_{12'} \sim -s_{1'2} \rightarrow 2p_1p_2 \ , \\ &s_{23} \sim -s_{2'3} \rightarrow 2p_2p_3 \ , \quad s_{31} \sim s_{3'1} \rightarrow 2p_3p_1 \ , \end{aligned} \tag{3.3}$$

while for invariants of the form $s_{122'} = (P_1 + Q_2)^2 = (P_1 + P_2 - P_{2'})^2$

$$\begin{aligned} &s_{122'} \sim 2P_1.Q_2 \rightarrow 2p_1(\hat{q}_2 - q_{21}) \ , \\ &s_{133'} \sim 2P_1.Q_3 \rightarrow 2p_1(\hat{q}_3 - q_{31}) \ , \\ &s_{233'} \rightarrow 2p_2(\hat{q}_3 - q_{32}) \ , \quad s_{311'} \rightarrow 2p_3(\hat{q}_1 - q_{13}) \ , \ \cdots \end{aligned} \tag{3.4}$$

Note that there is no constraint on the relative magnitudes of the Q_i. They can lie in either a spacelike plane ($s - s$ in the notation of [11] and of Appendix D) or in a plane with a timelike component ($s - t$ in the same notation).

3.2 Light-Cone Description of Helicity-Flip Helicity-Pole Limits

We can take a "helicity-flip helicity-pole limit", in addition to the triple-regge limit, by also taking

$$\frac{s_{31}}{s_{133'} \ s_{311'}} \sim \frac{1}{(\hat{q}_3 - q_{31})(\hat{q}_1 - q_{13})} \rightarrow \infty \tag{3.5}$$

$$\frac{s_{32}}{s_{233'} \ s_{322'}} \sim \frac{1}{(\hat{q}_3 - q_{32})(\hat{q}_2 - q_{23})} \rightarrow \infty \tag{3.6}$$

Introducing the notation of Appendix B, this limit is therefore equivalent to taking

$$q_{21^-} = \hat{q}_2 - q_{21} = q_{31} - \hat{q}_3 \rightarrow 0 \tag{3.7}$$

$$q_{12^-} = \hat{q}_1 - q_{12} = q_{32} - \hat{q}_3 \rightarrow 0 \tag{3.8}$$

With this additional limit taken

$$\begin{aligned} &P_1 \rightarrow P_1^+ = (p_1, p_1, 0, 0) \ , \quad p_1 \rightarrow \infty \qquad Q_1 \rightarrow (q_{112-}, q_{112-}, q_{112-}, q_{13}) \\ &P_2 \rightarrow P_2^+ = (p_2, 0, p_2, 0) \ , \quad p_2 \rightarrow \infty \qquad Q_2 \rightarrow (q_{212-}, q_{212-}, q_{212-}, q_{23}) \\ &P_3 \rightarrow P_3^+ = (p_3, 0, 0, p_3) \ , \quad p_3 \rightarrow \infty \qquad Q_3 \rightarrow (q_{33}, q_{33}, q_{33}, q_{33}) \end{aligned} \tag{3.9}$$

where now the constraints of momentum conservation are

$$q_{112-} + q_{212-} + q_{33} = 0 \ , \quad q_{13} + q_{23} + q_{33} = 0 \tag{3.10}$$

giving three independent q variables. As our notation indicates, the helicity-flip limit is naturally expressed in terms of the light-cone variables introduced in Appendix B.

We can obviously also define additional helicity-pole limits by taking

$$\begin{aligned} q_{32^-} &= \hat{q}_3 - q_{32} = q_{23} - \hat{q}_1 \to 0 && (3.11) \\ q_{23^-} &= \hat{q}_2 - q_{23} = q_{13} - \hat{q}_1 \to 0 && (3.12) \end{aligned}$$

or

$$\begin{aligned} q_{13^-} &= \hat{q}_1 - q_{13} = q_{23} - \hat{q}_2 \to 0 && (3.13) \\ q_{31^-} &= \hat{q}_3 - q_{31} = q_{21} - \hat{q}_2 \to 0 && (3.14) \end{aligned}$$

corresponding to further sets of light-cone co-ordinates defined as in Appendix B. Note that for all three helicity-pole limits, the Q_i must lie in the $s - s$ region, i.e. a spacelike plane in which the euclidean constraint

$$|Q_i| + |Q_j| \geq |Q_k| \qquad \forall\, i, j, k \tag{3.15}$$

is satisfied. This is necessary for the helicity-flip limit to be a physical region limit. In fact the Q_i lie in the $s - s$ region provided only that q_{ij^-} are sufficiently small.

4. Calculation of Feynman Diagrams

In this Section we calculate directly contributions to the triple-regge limit from selected diagrams. We will not attempt to be complete in our discussion and will not include color factors. The counting of all contributions from all diagrams has to be done via the multiple discontinuity asymptotic dispersion relation formalism that we develop in Section 5. In anticipation of this formalism we first look for on-shell configurations that form intermediate states in the scattering and extract the corresponding reggeon interaction. We will show that the necessary axial triangle diagram appears in the contributions of a maximally non-planar diagram. However, when we subsequently locate the momentum configuration in which the anomaly divergence actually occurs we find that it is in a region where the discontinuities we have potentially evaluated are no longer present.

4.1 The Simple Planar Diagram

We begin with the first diagram of Fig. 2.3, which is also discussed in [12]. This planar diagram (almost obviously) contains no anomaly and, as we discuss shortly, will not contribute at all to the six-reggeon interaction if all-orders reggeization of quarks and gluons is exploited. Nevertheless, we begin with it since it is the simplest to evaluate and to use to illustrate our general methods. The notation we use is illustrated in Fig. 4.1.

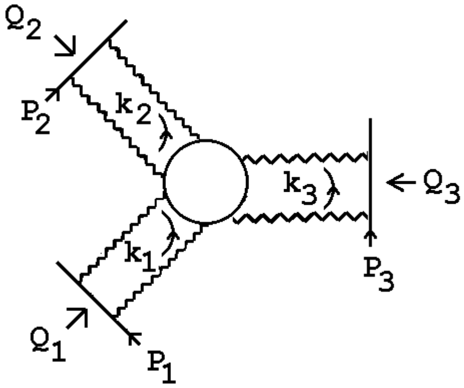

Fig. 4.1 The Simple Planar Diagram.

We will not specify the direction of the quark line but rather sum over both possibilities in the diagrams we discuss. Because we are interested in infra-red contributions from the central quark loop we can suppose that large momenta do not flow through this loop. We can then use directly, for each scattering quark, arguments (reviewed in Appendix C) that apply when a fast quark scatters off a slow system.

We begin by reducing each loop integral involving gluon propagators to a "transverse momentum" integral by carrying out longitudinal integrations. For a general diagram there will be an ambiguity as to which light-cone co-ordinates to use and also which quark propagators to use to perform longitudinal integrations. For Fig. 4.1, however, each gluon loop momentum naturally passes through only one line of the quark loop and there is no ambiguity as to how to proceed.

If we draw Fig. 4.1 as describing a physical scattering process with time in the upward vertical direction, as in Fig. 4.2,

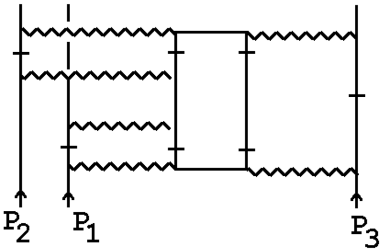

Fig. 4.2 A Physical Scattering Process.

it is clear that each of the quark propagators marked with a hatch can be naturally close to mass-shell and contribute to intermediate states as part of the scattering process. Since we are only looking for interesting contributions in this Section, we will not give a complete contour-closing argument as to whether a particular on-shell configuration is definitively present asymptotically. Rather if propagators are close to mass-shell during a scattering process we will take this as an indication that a leading asymptotic contribution may be obtained if these propagators are put on-shell by performing corresponding longitudinal momentum integrations.

Each loop integral has the form I_i illustrated in Fig. 4.3.

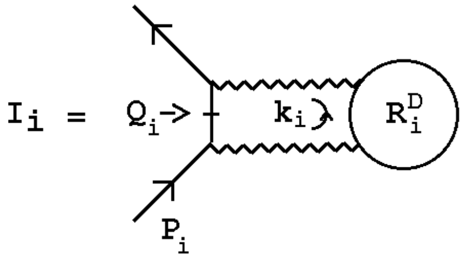

Fig. 4.3 The One Loop Integral I_i.

R_i^D denotes the remainder of the diagram besides the two gluon propagators shown. We choose a combination of conventional light-cone co-ordinates for each loop, i.e. (in the notation of Appendix B) k_{ii^+}, k_{ii^-} and $k_{i\perp}$, $i = 1, 2, 3$. In the limit $P_{i^+} \to \infty$, we can use (C.2) - (C.7) to approximate the initial and final state spinors by $\not{p}_{ii^+}/m$ and so write each of the three I_i (in Feynman gauge) in the form

$$\begin{aligned} I_i \;&=\; g^2 \int d^4k_i \left[\frac{\not{p}_{ii^+}}{m}\right] \gamma_\mu \, [\not{p}_i - \not{k}_i + m]^{-1} \, \gamma_\nu \left[\frac{\not{p}_{ii^+}}{m}\right] \left[\frac{g_{\mu\alpha}}{k_i^2}\right]\left[\frac{g_{\nu\beta}}{(Q_i-k_i)^2}\right] R^D_{i\alpha\beta} \\ \rightarrow \quad & g^2 \, \frac{p_{i^+}}{m} \int d^4k_i \; \delta\Big(k_{ii^-} - (k^2_{ii\perp} - m^2)/2p_{ii^+}\Big) \, \frac{1}{k_i^2 \; (Q_i-k_i)^2} \;\; R^D_{i\; i^-,i^-} \end{aligned} \tag{4.1}$$

As discussed above, we have replaced the hatched quark propagator of Fig. 4.3 by a δ-function. Using this δ-function to perform the k_{ii^-} integration we obtain

$$I_i \;=\; g^2 \, \frac{p_{ii^+}}{m} \int d^2k_{ii\perp} dk_{ii^+} \; \frac{1}{k^2_{ii\perp} \; (Q_{ii\perp} - k_{ii\perp})^2} \;\; R^D_{i\; i^-,i^-} \tag{4.2}$$

where we have used $k_{ii^-} \sim 1/p_{ii^+} \;\rightarrow 0$, together with $Q_{ii^-} = 0$, to eliminate the longitudinal momentum components in the gluon propagators.

For Fig. 4.1 the remaining k_{ii^+} integrations can be performed very simply. As illustrated in Fig. 4.4,

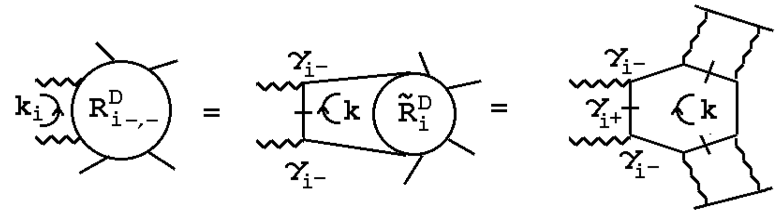

Fig. 4.4 $\quad R^D_{i\;-,-}$ for Fig. 4.1.

the two gluons in I_i are separated by the single quark line within R^D_i that carries the only dependence on k_{ii^+}. We again replace the hatched propagator for this line by the corresponding δ-function and use it to carry out the k_{ii+} integration, i.e. we write

$$\begin{aligned} \int dk_{ii^+} \; R^D_{i\;-,-} \;&=\; g^2 \int dk_{ii^+} \; \delta\Big((k_i + k)^2 - m^2\Big) \; \gamma_{i^-} \; [\; \gamma \cdot (k_i + k) \;] \; \gamma_{i^-} \; \tilde{R}^D_i \\ &=\; g^2 \int dk_{ii^+} \; \delta\Big(k_{ii^+}k_{i^-} + k_{i^+}k_{i^-} - (k_{i\perp} + k_{ii\perp})^2 - m^2\Big) \\ &\qquad \times \; \gamma_{i^-} \; [\gamma_{i^+} \cdot k_{i^-} + \cdots] \; \gamma_{i^-} \; \tilde{R}^D_i \\ &=\; g^2 \; \gamma_{i^-} \; \gamma_{i^+} \; \gamma_{i^-} \; \tilde{R}^D_i \;=\; g^2 \; \gamma_{i^-} \; \tilde{R}^D_i \end{aligned} \tag{4.3}$$

Using (4.1) - (4.3) for each of the k_i integrations, Fig. 4.1 gives the asymptotic amplitude

$$g^{12} \; \frac{p_{11^+}p_{22^+}p_{33^+}}{m^3} \; J_1(Q_1^2) J_1(Q_2^2) \; J_1(Q_3^2) \; \Gamma^v_{1^-2^-3^-}(Q_1, Q_2, Q_3) \tag{4.4}$$

where $J_1(Q^2)$ is the familiar two-dimensional integral (C.9) and $\Gamma^v_{1^-2^-3^-}(Q_1, Q_2, Q_3)$ can be identified with a particular component of the tensor that the triangle diagram contributes to the three-point function of three vector currents, i.e.

$$\Gamma^v_{1^-2^-3^-}(Q_1, Q_2, Q_3, m) = i \int \frac{d^4k \; Tr\{\gamma_{1^-} \; (\not{k} + m)\gamma_{2^-}(\not{k} + \not{Q}_2 + m)\gamma_{3^-}(\not{k} + \not{Q}_1 + m)\}}{(k^2 - m^2)([k + Q_2]^2 - m^2)([k + Q_1]^2 - m^2)} \tag{4.5}$$

Note that (4.4) has been derived in the full triple Regge limit (3.1) in which the Q_i do not lie entirely in the $k_{i\perp}$ plane. While the J_1 factors depend only on the corresponding Q_i^2, the triangle diagram factor $\hat{\Gamma}^v_{1^-2^-3^-}(Q_1, Q_2, Q_3, m)$ will have a dependence on the light-like momenta $\hat{q}_1, \hat{q}_2$ and $\hat{q}_3$ of (3.1). In the helicity-pole limit (3.9) the magnitudes of the light-like momenta are identified with one of the spacelike components of the Q_i. This limit can clearly be taken smoothly within $\hat{\Gamma}^v$.

A-priori, it is straightforward to choose the quantum numbers of the Q_i-channels so that the lowest-order contribution is associated with two-reggeon exchange in each channel (color zero would be the simplest). In this case, the $J_1(Q_i^2)$ factors would be associated with the two-reggeon state. However, as we remarked at the beginning of this sub-section, since Fig. 4.1 is planar, we expect that if reggeization effects are added it ultimately does not provide a coupling for two-reggeon states. We can briefly describe how this happens for Fig. 4.1 as follows.

We performed the k_{11^+}-integration by using the hatched propagator contained in $R^D_{1^-,-}$ as illustrated in Fig. 4.4. This integration can instead be written as an integral over the "missing mass" cross-energy

$$M^2 \;=\; (k_1 + Q_2)^2 \tag{4.6}$$

The singularities of $R^D_{1^-,-}$ are all on the positive axis in the M^2-plane and so the contour integration over M^2 could be closed to zero if the large M^2 behavior were appropriate. In the lowest-order diagram we are discussing this is provided by quark-antiquark exchange which is just divergent enough to prevent the contour closing. Therefore, the reggeon vertex can be written as an integral at infinity and it's main role will be to provide contributions that cancel less planar diagrams and produce reggeon Ward identity zeroes at zero transverse momentum points. It is well-known from studies[16] of QED that planar diagrams give contributions with very little analytic structure that, typically, can be written as contour integrals at infinity or equivalently as a subtraction in a dispersion relation. The presence of the planar diagram contributions can, in fact, be deduced by studying the non-planar contributions and demanding that the Ward identity constraints of gauge invariance be satisfied.

In higher-orders the quark-antiquark reggeization illustrated in Fig. 4.5 will appear.

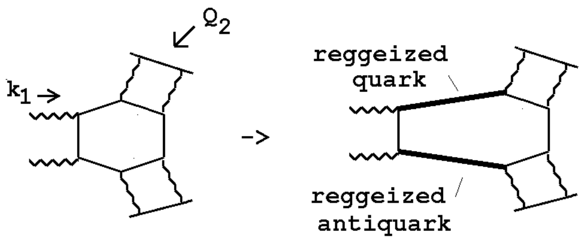

Fig. 4.5 Quark-Antiquark Reggeization

If the reggeization effects are summed to all orders (which does not destroy the validity of the low-order approximation) the reduced power behavior will allow the closing of the M^2 contour to give zero. Consequently the analytic structure of the triangle reggeon interaction we have extracted will disappear as higher-order contributions are included (in parallel with the well-known AFS cancelation[17]). We anticipate that only diagrams with sufficient non-planarity to prevent any possible contour closing will survive as reggeization effects are included. The reggeon Ward identities will appear as properties of these diagrams that follow from the shifting of integration variables that becomes allowed once reggeization effects are included.

The presence of the anomaly would, of course, be expected to interfere with integration shifts and could be found in the ultra-violet region this way. However, it is just because we expect this to be a very subtle issue that we have focussed on finding the anomaly in the infra-red region. While (4.4) and (4.5) demonstrate how, as a lowest-order approximation, the full four-dimensional triangle diagram can appear as an effective interaction in the triple-Regge limit, since only vector couplings, i.e. the γ_{i^-}, appear there is no possibility for the anomaly infra-red divergence.

We must proceed further to find diagrams that generate a reggeon interaction containing the effective γ_5 coupling necessary to produce the anomaly. For the next diagram we study a γ_5 coupling does appear. However, we then find that the correct tensor and momentum structure for the full anomaly divergence is still absent.

4.2 A Diagram With Some Non-planarity.

In all other diagrams besides that of Fig. 4.1 (apart from those that are simply twisted versions of this diagram) one or more of the gluon loop momenta flows through more than one line of the quark loop. This introduces an extra complexity in carrying out the integrations over the longitudinal gluon momenta. The next diagram we consider, the second shown in Fig. 2.3, introduces the minimal complexity of this kind. This diagram can be redrawn as in Fig. 4.6(a), or as in Fig. 4.6(b). There is just one gluon loop momentum, i.e. k_3, that flows through more than one line of the internal quark loop. The k_1 and k_2 longitudinal integrations are straightforward and can be performed in the same way as we did for the longitudinal integrations of Fig. 4.1. For k_3 there are two possible routes. The first is shown in Fig. 4.6(a). The second would be that shown in Fig. 4.6(b) if the external momentum flow was kept as in Fig. 4.1(a).

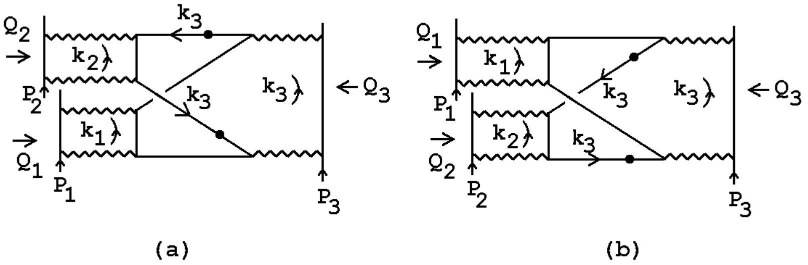

Fig. 4.6 (a) A Diagram With Some Non-planarity (b) The Same Diagram Redrawn.

If we route k_3 as in Fig. 4.6(a), then there are two possible quark propagators, each marked with a dot, that could be used to perform the k_{3+}-integration. If the time-ordering of the scattering process is essentially represented by Fig. 4.6(a), then it would appear that only the lower dotted propagator gives a quark state that can be part of an on mass-shell intermediate state. The upper dotted propagator appears to describe a virtual exchange that will be a long way from mass-shell. However, when the diagram is redrawn as in Fig. 4.6(b), in the scattering process now described, the role of the two propagators is interchanged. It is now the lower propagator that is virtual and far from mass-shell. Clearly the two contributions obtained by using the two possible propagators to perform the k_{3+}-integration must be added.

Consider first the contribution of the upper dotted propagator in Fig. 4.6(a). After the longitudinal k_1 and k_2 integrations have been performed we will be left with the box-diagram integral illustrated in Fig. 4.7.

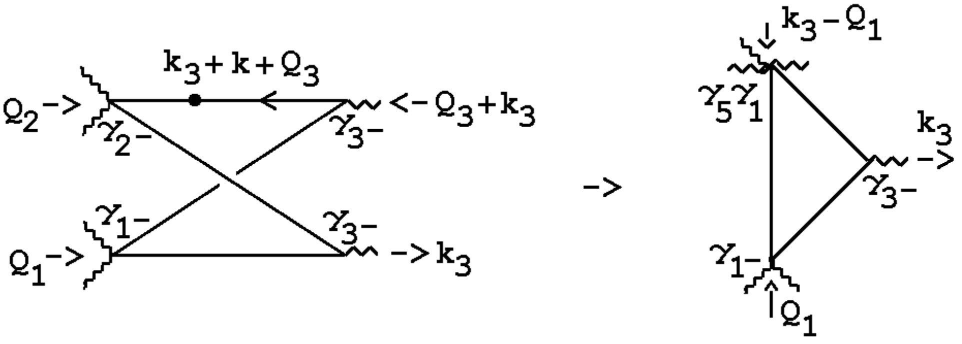

Fig. 4.7 The Box and Triangle Diagrams Generated by Fig. 4.6.

The k_{33-} integration can be done by again utilising the evaluation of Fig. 4.3. With the dotted propagator replaced by a δ-function, the relevant factors in the k_{33+} integration are

$$\begin{aligned}
&\int dk_{33^+}\ \delta\Big((k_3+k+Q_3)^2-m^2\Big)\ \gamma_{2^-}\ \Big((k_3+k+Q_3)\cdot\gamma+m\Big)\ \gamma_{3^-} \\
&\quad = \ \int dk_{33^+}\ \delta\Big((k_{3^-}+Q_{33^-})k_{33^+}+\cdots\Big) \\
&\qquad\qquad \times\ \gamma_{2^-}\ \Big((k_{3^-}+Q_{33^-})\cdot\gamma_{3^+}+\cdots\Big)\ \gamma_{3^-} \\
&\quad = \ \gamma_{2^-}\gamma_{3^+}\gamma_{3^-}\ \ +\ \ \cdots \\
&\quad = \ 2\ (\gamma_0-\gamma_2-\gamma_3)\ +\ 2\ i\gamma_5\gamma_1\ \ +\ \ \cdots
\end{aligned} \tag{4.7}$$

where, in the last line, we have used (C.21) to show that an axial γ_5-coupling is produced by the product of three γ-matrices. The omitted terms generate only what we call "non-local couplings". As elaborated in Appendix C, a non-local coupling is generated whenever the momentum dependence of the integrated propagator does not simply scale out of the integral, as it does for the part of (4.7) that we have written explicitly.

Focussing on the γ_5-interaction produced by (4.7), the asymptotic amplitude, with all longitudinal integrations performed, can be written as

$$\begin{aligned}
g^{12}\ \frac{p_{11^+}p_{22^+}p_{33^+}}{m^3}\ \int \frac{d^2\underline{k}_{11\perp}}{\underline{k}^2_{11\perp}(Q_1-\underline{k}_{11\perp})^2}\ \int \frac{d^2\underline{k}_{22\perp}}{\underline{k}^2_{22\perp}(Q_2-\underline{k}_{22\perp})^2}\ \int \frac{d^2\underline{k}_{33\perp}}{\underline{k}^2_{33\perp}(Q_3-\underline{k}_{33\perp})^2} \\
\int d^4k\ \ \frac{Tr\{\gamma_{1^-}(\not{k}+\not{Q}_1+m)\gamma_5\gamma_1\ (\not{k}+\not{k}_3+m)\gamma_{3^-}(\not{k}+m)\}}{(k-m^2)([k+Q_1]^2-m^2)([k+k_3]^2-m^2)}\qquad +\ \ \cdots
\end{aligned} \tag{4.8}$$

where $k_{33^-}=0$ and k_{33^+} is determined from the δ-function used in (4.7), and that part of the amplitude not written explicitly now contains either a vector coupling or a non-local coupling in place of the $\gamma_5\gamma_1$ coupling. If we again remove the $k_{ii\perp}$ integrations, the gluon propagators, and the p_{ii^+} dependence that are all associated with the three two-reggeon states, (4.8) gives a six-reggeon interaction containing the triangle diagram of Fig. 4.7, i.e.

$$\Gamma^a(Q_1,Q_3,k_{33\perp})\ =\ \int d^4k\frac{Tr\{\gamma_{1^-}(\not{k}+\not{Q}_1+m)\gamma_5\gamma_1\ (\not{k}+\not{k}_3+m)\gamma_{3^-}(\not{k}+m)\}}{(k-m^2)([k+Q_1]^2-m^2)([k+k_3]^2-m^2)}\ \ +\ \cdots \tag{4.9}$$

where we still have $k_{33^-}=0$ and k_{33^+} is to be determined by the mass-shell constraint of (4.7), thus giving the Q_3-dependence of (4.9).

Since $\Gamma^a(Q_1,Q_3,k_{33\perp})$ contains a γ_5 coupling, it is straightforward to identify it with a component of the triangle diagram tensor for an axial current and two vector currents. However, the maximal singularity associated with the anomaly requires specific momenta and tensor components to be present. We must have two tensor components that can project on to the same light-cone component - this would have to be γ_{1^-} and $\gamma_5\gamma_1$. The third vertex must then carry spacelike momentum of $O(\mathsf{q}) \to 0$, implying that we should take $k_3 \sim \mathsf{q} \to 0$. Finally a finite light-like momentum parallel to $\underline{n}_{1^-}$ must enter at the γ_5 vertex. But the light-cone component of Q_1 is orthogonal to $\underline{n}_{1^-}$. This conflict implies that a kinematical configuration producing the maximal anomaly divergence can not occur.

4.3 Alternative Light-Cone Co-ordinates and Absence of the Anomaly

We can give a direct argument that there is no anomaly in the full reggeon interaction produced by Fig. 4.6(a). This argument will be important for the general analysis of discontinuities in Section 6.

In Appendix B we have shown that light-cone co-ordinates and associated γ-matrices can be introduced using any two light-like momenta whose space components are orthogonal. The regge limit calculations of Appendix C demonstrate that equivalent results are obtained using such co-ordinates and we use various co-ordinates of this form elsewhere in the paper (including the discussion of helicity-pole limits in the previous Section.) In particular let us repeat our evaluation of Fig. 4.6(a), with k_3 routed as shown, but for the k_3 longitudinal integration use co-ordinates in which $\underline{n}_{2^+}$ and $\underline{n}_{3^+}$ are the basic light-like momenta. Our k_3 co-ordinates are now

$$k_{33^-} = k_{30} - k_{33}\ , \quad k_{32^-} = k_{30} - k_{32}\ , \quad k_{31}\ , \quad \tilde{k}_{23} = k_{32} + k_{33} - k_{30} \tag{4.10}$$

The k_{33^-} integration can again be performed using the evaluation of Fig. 4.3. However, instead of (4.7), the k_{32^-} integration of the upper dotted propagator of Fig. 4.6(a) gives

$$\begin{aligned}
&\int dk_{32^-}\ \delta\Big((k_3+k+Q_3)^2 - m^2\Big)\ \gamma_{2^-}\ \Big((k_3+k+Q_3)\cdot\gamma + m\Big)\ \gamma_{3^-} \\
&\quad = \int dk_{32^-}\ \delta\Big((k_{3^-}+Q_{33^-})k_{32^-} + \cdots\Big) \\
&\qquad\qquad \times \gamma_{2^-}\ \Big((k_{3^-}+Q_{33^-})\cdot\gamma_{2^-} + \cdots\Big)\ \gamma_{3^-} \\
&\quad = \gamma_{2^-}\gamma_{2^-}\gamma_{3^-} \ + \ \cdots \\
&\quad = 0 \ + \ \cdots
\end{aligned} \tag{4.11}$$

Now no local terms appear. Only omitted "non-local" terms are generated. Evaluation of the contribution from the lower dotted propagator in Fig. 4.6(a) will similarly give no local terms. While a distinction between the contributions of local and non-local couplings may be difficult to maintain in general (after integration), if we assume that the anomaly can appear only when an appropriate local γ_5 coupling is present. then we have demonstrated it's absence in the diagram of Fig. 4.6.

4.4 A Maximally Non-Planar Diagram

Finally we study the third diagram of Fig. 2.3. In this case there will be clear anomaly contributions which, when general external couplings are present, cancel only after all diagrams of this kind are summed. As illustrated in Fig. 2.4, this diagram has a "maximally non-planar" property - which produce a "maximal complexity" in terms of evaluating the longitudinal gluon momentum integrations.

The first point we note is that there is no natural choice for routing the gluon loop momenta through the internal quark loop. Each momentum flows through three quark propagators no matter in which direction we send it. As to which combinations of propagators can be simultaneously close to mass-shell, we note that if we draw the scattering as in Fig. 4.8(a) then

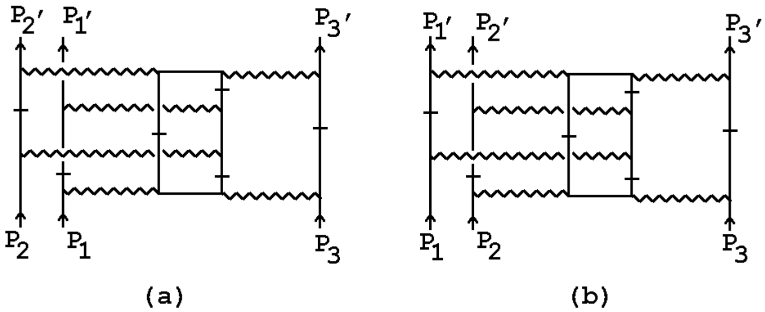

Fig. 4.8 Two Scattering Processes Described by the Diagram of Fig. 2.4

the hatched propagators can obviously be simultaneously close to mass-shell and produce intermediate states. However, if we redraw the diagram as in Fig. 4.8(b), an alternative set of hatched lines is naturally chosen. It is easy to check that the second set corresponds to the three loop propagators not hatched in Fig. 4.8(a). (These two contributions were already recognized in Section 2.) Note that the hatched lines in Fig. 4.8(a) correspond to taking a double discontinuity in s_{13} and $s_{2'3'}$ while the hatched lines in Fig. 4.8(a) correspond to taking a double discontinuity in s_{23} and $s_{1'3'}$. This will be an important distinction in the following.

There are further scattering processes described by the diagram we are discussing that involve interchanging ingoing and outgoing particles. For example, the processes of Fig. 4.9. Such contributions will be included separately in the multiple discontinuity formalism of the next two Sections. (In the language of the next Section, one maximally non-planar Feynman diagram contains discontinuities associated with several different hexagraphs.) In this sub-section we will discuss only the contribution of Fig. 4.8(a) in detail. After we have discussed Fig. 4.8(a), it will be obvious that the discussion immediately extends to Fig. 4.8(b) and that it also generalises to the corresponding contributions from the diagrams of Fig. 4.9.

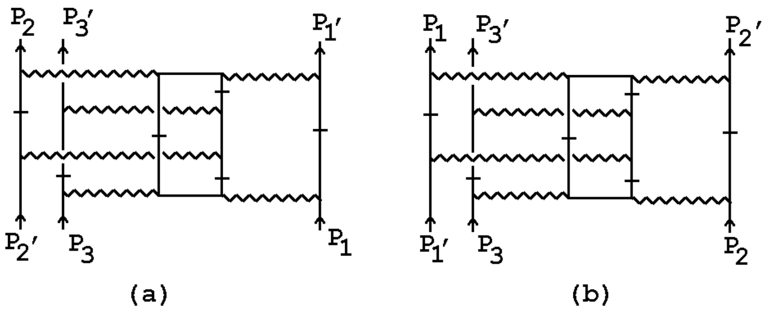

Fig. 4.9 Further Scattering Processes Described by the Diagram of Fig. 2.4

For reasons that will become apparent, it will be desirable to keep as much symmetry as possible in our kinematic analysis, even at the cost of using a more complicated labeling for momenta flowing along the quark loop lines. Therefore, we label the momentum flow into the internal quark loop of Fig. 4.8(a) as in Fig. 4.10, where the γ matrices that contribute in the triple-regge limit are also shown.

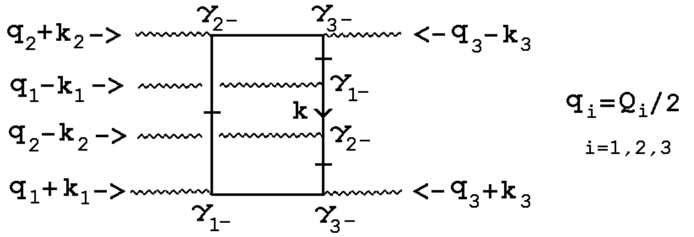

Fig. 4.10 The Quark Loop in Fig. 4.8(a).

This time we use the light-cone co-ordinates $(k_{i1-}, k_{i2-}, \tilde{\underline{k}}_{i\perp})$ to perform the k_1 and k_2 integrations and to evaluate the γ-matrix trace associated with the quark loop. For the k_3 integration we use conventional light-cone co-ordinates. The evaluation of the integral I_i of Fig. 4.3 can be used to perform the k_{11-}, k_{22-} and k_{3-} integrations. The remaining longitudinal integrations have to be carried out using δ-functions for propagators belonging to the internal quark loop, A-priori there are six different options for choosing the longitudinal k_i to be used to put the hatched lines in Fig. 4.10 on-shell. These possibilities are indicated schematically in Fig. 4.11

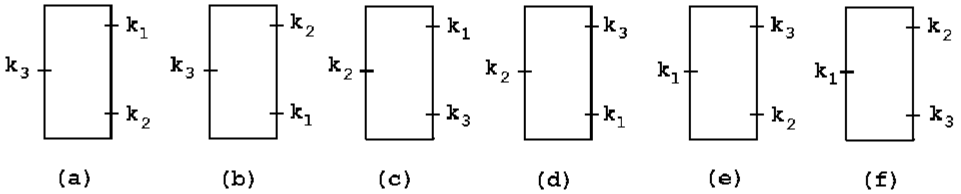

Fig. 4.11 Possible Choices of δ-function Integrations for Fig. 4.10.

We consider first which of the possibilities in Fig. 4.11 can generate the necessary local couplings. For the δ-function assignment of Fig. 4.11(b), we note that both the k_{12-} and the k_{21-} integrations will be analagous to (4.11) in that the potential point-coupling, involving the γ-matrix (within the numerator of the on-shell quark) that is multiplied by the momentum scaling the δ-function momentum, is eliminated by one of the adjacent γ-matrices. Hence no local coupling is produced. For Fig. 4.11(c) the k_{21-} integration similarly produces no local coupling. For Fig. 4.11(d) it is the k_{12-} and the k_{21-} integrations, for Fig. 4.11(e) the k_{12-} integration, and for Fig. 4.11(f) both the k_{12-} and k_{21-} integrations, that produce no local coupling. Consequently, with the light-cone co-ordinates we have chosen, only the δ-function assignment of Fig. 4.11(a) gives a contribution with local couplings from all three integrations.

For the δ-function assignment of Fig. 4.11(a) we route momenta through the quark loop of Fig. 4.10 as illustrated in Fig. 4.12

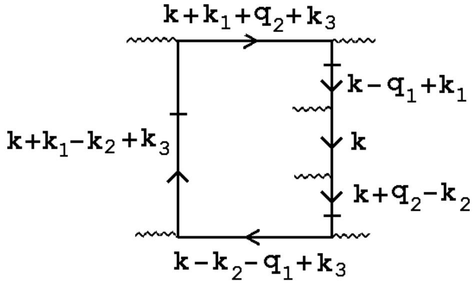

Fig. 4.12 Momentum Flow for the δ-function Assignment of Fig. 4.11(a).

We calculate the local couplings generated as follows.

$$\begin{aligned}\int dk_{12-}\ \delta\Big((k_1+k-q_1)^2-m^2\Big)\ \gamma_{3-}\ \Big((k_1+k-q_1)\cdot\gamma+m\Big)\ \gamma_{1-} \\ =\ \int dk_{12-}\ \delta\Big(k_{1-}\ k_{12-}+\cdots\Big) \\ \times\,\gamma_{3-}\ \Big(k_{1-}\cdot\gamma_{2-}+\cdots\Big)\ \gamma_{1-} \\ =\ \gamma_{3-}\gamma_{2-}\gamma_{1-}\ \ +\ \ \cdots\end{aligned} \tag{4.12}$$

$$\begin{aligned}
&\int dk_{21-}\delta\Big((k_2-k-q_2)^2-m^2\Big)\;\gamma_{2-}\;\Big((k_2-k-q_2)\cdot\gamma+m\Big)\;\gamma_{3-}\\
&\quad=\;\int dk_{21-}\;\delta\Big(k_{2-}k_{21-}+\cdots\Big)\\
&\qquad\qquad\times\gamma_{2-}\;\Big(k_{2-}\cdot\gamma_{1-}+\cdots\Big)\;\gamma_{3-}\\
&\quad=\;\gamma_{2-}\gamma_{1-}\gamma_{3-}\quad+\quad\cdots
\end{aligned}\tag{4.13}$$

$$\begin{aligned}
&\int dk_{33+}\;\delta\Big((k_3+k+k_1-k_2)^2-m^2\Big)\;\gamma_{1-}\;\Big((k_3+k+k_1-k_2)\cdot\gamma+m\Big)\;\gamma_{2-}\\
&\quad=\;\int dk_{33+}\;\delta\Big((k_{3-}+k_{13-}-k_{23-})k_{33+}+\cdots\Big)\\
&\qquad\qquad\times\gamma_{1-}\;\Big((k_{3-}+k_{13-}-k_{23-})\cdot\gamma_{3+}+\cdots\Big)\;\gamma_{2-}\\
&\quad=\;\gamma_{1-}\gamma_{3+}\gamma_{2-}\quad+\quad\cdots
\end{aligned}\tag{4.14}$$

In each case the dots indicate the contribution of additional non-local couplings. We defer the evaluation of the δ-functions for the moment. The triangle diagram structure of the local couplings is illustrated in Fig. 4.13,

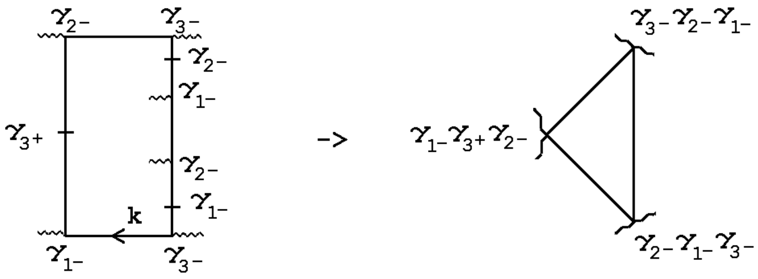

Fig. 4.13 Local couplings generated by the δ-function Assignment of Fig. 4.11(a).

With all longitudinal integrations performed, the asymptotic amplitude obtained from Fig. 4.8(a) can be written as

$$\begin{aligned}
&\qquad g^{12}\;\frac{p_{11+}\;p_{22+}\;p_{3+}}{m^3}\quad\times\\
&\int\frac{d^2\underline{k}_{112+}}{(q_1+\underline{k}_{112+})^2(q_1-\underline{k}_{112+})^2}\;\int\frac{d^2\underline{k}_{212}}{(q_2+\underline{k}_{212+})^2(q_2-\underline{k}_{212+})^2}\;\int\frac{d^2\underline{k}_{33\perp}}{(q_3+\underline{k}_{33\perp})^2(q_3-\underline{k}_{33\perp})^2}\\
&\int d^4k\;\frac{Tr\{\hat{\gamma}_{12}(\not{k}+\not{k}_1+\not{q}_2+\not{k}_3+m)\hat{\gamma}_{31}(\not{k}+m)\hat{\gamma}_{23}(\not{k}-\not{k}_2+\not{q}_1+\not{k}_3+m)\}}{([k+k_1+q_2+k_3]^2-m^2)(k^2-m^2)([k-k_2+q_1+k_3]^2-m^2)}\;+\;\cdots
\end{aligned}\tag{4.15}$$

where

$$\hat{\gamma}_{31}=\gamma_{3-}\gamma_{2-}\gamma_{1-}\;,\quad\hat{\gamma}_{23}=\gamma_{2-}\gamma_{1-}\gamma_{3-}\;,\quad\hat{\gamma}_{12}=\gamma_{1-}\gamma_{3+}\gamma_{2-}\tag{4.16}$$

and $k_{11-} = k_{22-} = k_{33-} = 0$, with k_{12-}, k_{21-} and k_{33+} still to be determined by δ-function constraints. That part of the amplitude not shown explicitly in (4.15) contains non-local couplings at one, or more, vertices of the triangle diagram.

Before extracting a reggeon interaction from (4.15) we first separate out a potential anomaly generating part. Using, again, the identity (C.21), we can write

$$\hat{\gamma}_{31} \ = \ \gamma^{-,+,-} \ + \ i\,\gamma^{-,-,-}\,\gamma_5 \tag{4.17}$$

$$\hat{\gamma}_{23} \ = \ \gamma^{+,-,-} \ + \ i\,\gamma^{-,-,-}\,\gamma_5 \tag{4.18}$$

$$\hat{\gamma}_{12} \ = \ \gamma^{-,-,-} \ - \ i\,\gamma^{-,-,+}\,\gamma_5 \tag{4.19}$$

where

$$\gamma^{\pm,\pm,\pm} \ = \ \gamma^{\mu} \cdot n_{\mu}^{\pm,\pm,\pm} \ , \qquad n^{\pm,\pm,\pm\mu} \ = \ (1, \pm 1, \pm 1, \pm 1) \tag{4.20}$$

To obtain the divergence (A.6) when $m = 0$, we must have a component of the axial-vector triangle diagram tensor $\Gamma^{\mu\nu\lambda}$ with $\mu = \nu$ having a lightlike projection and λ having an orthogonal spacelike projection. Since $\hat{\gamma}_{31}$ and $\hat{\gamma}_{23}$ have the same γ_5 component, this requirement is met if we choose the γ_5 component from all three of the $\hat{\gamma}_{ij}$. The finite light-like momentum involved must simply have a projection on $n^{-,-,-\mu}$. (We will discuss how this occurs shortly.) $n^{-,-,+\mu}$ provides a distinct spacelike component in the $\underline{n}_3$ direction. The anomaly infra-red divergence (like the ultra-violet anomaly) is also present in the corresponding tensor component of the triangle diagram for one axial and two vector currents. Since the vector part of $\hat{\gamma}_{12}$ is identical to the γ_5 component of $\hat{\gamma}_{31}$ and $\hat{\gamma}_{23}$, the requirements for this case are partially met when we take the γ_5 part of either $\hat{\gamma}_{31}$ or $\hat{\gamma}_{23}$ together with the vector parts of the remaining two $\hat{\gamma}_{ij}$. However, the necessary distinct spacelike component in the $\underline{n}_3$ direction is not present.

The three γ_5 couplings give the $(m = 0)$ reggeon interaction

$$\Gamma_6(q_1, q_2, q_3, \tilde{\underline{k}}_1, \tilde{\underline{k}}_2, \underline{k}_{3\perp}, 0) \ = $$
$$\int d^4k \frac{Tr\{\gamma_5 \gamma^{-,-,+}(\not{k} + \not{k}_1 + \not{q}_2 + \not{k}_3)\gamma_5 \gamma^{-,-,-} \ \not{k} \ \gamma_5 \gamma^{-,-,-}(\not{k} - \not{k}_2 + \not{q}_1 + \not{k}_3)}{(k + k_1 + q_2 + k_3)^2 \ k^2 \ (k - k_2 + q_1 + k_3)^2} \ + \ \cdots \tag{4.21}$$

where, again, we note that $k_{11-} = k_{22-} = k_{33-} = 0$ and that k_{12-}, k_{21-} and k_{33+} remain to be determined by the δ-functions of (4.12) - (4.14). (4.21) corresponds to the triangle diagram illustrated in Fig. 4.14.

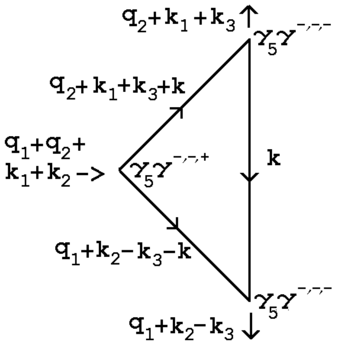

Fig. 4.14 The Triangle Diagram Corresponding to (4.21)

To see the maximal anomaly divergence we must be able to take the limit

$$(k_1+q_2+k_3)^2 \sim (q_1+q_2+k_1+k_2)^2 \sim (k_2+q_1-k_3)^2 \sim \mathbf{q}^2 \to 0 \tag{4.22}$$

of (4.21) with a finite light-like momentum flowing through the diagram that has a projection on $n^{-,-,-\mu}$. This momentum flow must also be consistent with the three mass-shell constraints determining k_{12-}, k_{21-} and k_{33+} respectively, i.e.

$$\begin{aligned}(k-q_1+k_1)^2 &= 0 && (4.23)\\ (k+q_2-k_2)^2 &= 0 && (4.24)\\ (k+k_1-k_2+k_3)^2 &= 0 && (4.25)\end{aligned}$$

To find momenta satisfying all of the required constraints, we first consider the limiting configuration in which $\mathbf{q}=0$ and ask whether this can be realized with the loop momentum $k \sim \mathbf{q} = 0$ (as discussed in Appendix A). It will be straightforward to subsequently add momenta that are $O(\mathbf{q})$.

We identify Fig. 4.14 with Fig. A2 by identifying $q_1+k_2-k_3$ with $\mathbf{q}_1$ and $q_1+q_2+k_1+k_2$ with $\mathbf{q}_2$. This requires that (in the limit $\mathbf{q} \to 0$)

$$q_1+q_2+k_1+k_2 = 0 \tag{4.26}$$

To satisfy (4.23) and (4.24) we take q_1-k_1 and q_2-k_2 lightlike, i.e.

$$\begin{aligned} q_1-k_1 &= (2l_{2-}, 2l_{2-}, 0, 0)\ , \quad q_2-k_2 = (2l_{1-}, 0, 2l_{1-}, 0)\\ => \quad \underline{q}_{112+} &= \underline{k}_{112+}\ , \quad \underline{q}_{212+} = \underline{k}_{212+}\end{aligned} \tag{4.27}$$

(using again the co-ordinates of Appendix B). Since the light-cone components of q_1+k_1 and q_2+k_2 can not cancel, satisfying (4.26) requires that

$$q_{12-} = -k_{12-} = l_{2-}\ , \quad q_{21-} = -k_{21-} = l_{1-} \quad \underline{q}_{112+} = -\underline{q}_{212+} \tag{4.28}$$

We then have

$$q_3 \ = \ -\,(q_1 + q_2) \ = \ -\,(l_{2^-} + l_{1^-}, l_{2^-}, l_{1^-}, 0) \tag{4.29}$$

and so for q_3 to have the form (3.1), we must have

$$l_{2^-} \ = \ - \ l_{1^-} \ = \ l \quad => \quad Q_3^2 \ = \ 4\ q_3^2 \ = \ -\,8\ l^2 \tag{4.30}$$

We choose l to be positive, we will discuss the implications of this shortly.

The most general light-cone momentum form for $q_1 + k_2 - k_3$ that has a projection on $n^{-,-,-\mu}$ and is orthogonal to $\underline{n}_3$ is

$$q_1 + k_2 - k_3 \ \sim \ \underline{n}_{lc} \ = \ (1, cos\theta_{lc}\ , sin\theta_{lc}\ , 0) \tag{4.31}$$

where θ_{lc} is arbitrary. Since $\underline{q}_{112+} + \ \underline{k}_{212+} = 0$, this requires that

$$\begin{aligned} (l,l,0,0) \ + \ (l,0,l,0) \ - \ (k_{33^+}, k_{31}, k_{32}, k_{33^+}) \ &\sim \ \underline{n}_{lc} \\ => \qquad k_3 = \ l\ (0, 1 - 2\ cos\theta_{lc}\ , 1 - 2\ sin\theta_{lc}\ , 0) & \end{aligned} \tag{4.32}$$

so that

$$(q_3 - k_3)^2 \ = \ 4q_3^2\ (1 - cos\theta_{lc})\ , \qquad (q_3 + k_3)^2 \ = \ 4q_3^2\ (1 - sin\theta_{lc}) \tag{4.33}$$

Finally, we must satisfy the last mass-shell condition (4.25). Writing

$$k_1 - k_2 + k_3 \ = \ -\,q_1 - k_2 + k_3 \ + \ 2\ \underline{q}_{112+} \tag{4.34}$$

and using (4.31) together with (4.32) we obtain

$$k_1 - k_2 + k_3 \ = \ -\,2l(1, cos\theta_{lc}\ , sin\theta_{lc}\ , 0) + 2q_{112-}(1,1,1,0) + 2q_{13}(0,0,0,1) \tag{4.35}$$

and so (4.25) becomes

$$2\ l\ q_{112-}\ (1 - cos\theta_{lc} - sin\theta_{lc}) = \ -\,q_1^2 \ = \ \underline{q}_{112+}^2 \ = \ q_{112-}^2 + q_{13}^2 \tag{4.36}$$

or, equivalently,

$$\begin{aligned} (q_1 + k_1)^2 \ = \ 4\ q_1^2 \ = \ Q_1^2 \ = \ (q_2 + k_2)^2 \ = \ 4q_2^2 \ = \ Q_2^2 & \\ = \ -\,8\ l\ q_{112-}\ (1 - cos\theta_{lc} - sin\theta_{lc}) & \end{aligned} \tag{4.37}$$

Note that as $Q_3^2 \ \sim \ l^2 \ \rightarrow \ 0$ then also $(q_1 + k_1)^2 \ \sim \ (q_2 + k_2)^2 \ \rightarrow \ 0$

(4.36) can apparently be satisfied for arbitrary q_1^2 by choosing q_{112-} and q_{13} appropriately. However, there is a subtlety. To give light-like intermediate states in which the scattering takes place as in Fig. 4.8(a) we must take $l > 0$. The time component of $k_1 - k_2 + k_3$, i.e.

$$-2l \ + \ 2q_{112-} \tag{4.38}$$

should also be positive. This requires $q_{112-} > l > 0$, but then (4.36) can only be satisfied if

$$q_{112-} \ < \ 2l(cos\theta_{lc} + sin\theta_{lc} - 1) \ < \ 2l(\sqrt{2} - 1) \ < \ l \tag{4.39}$$

so that (4.38) can not be positive. We conclude that if the mass-shell constraints that we have imposed are to be associated with taking discontinuities, then the anomaly can only occur simultaneously if the scattering process takes place in an unphysical region. As we will discuss at length in the next Section, there is indeed an unphysical region where the mass-shell constraints can give discontinuities and the anomaly can occur. That unphysical scattering processes must play a fundamental role in the occurrence of the anomaly should not be a surprise because of the chirality transition that has to be involved.

In fact, for $l < 0$ the momentum configuration we have arrived at does describe the scattering illustrated in Fig. 4.15(a), if this is interpreted as a space-time diagram with time directed up the page. This is the process already illustrated in Fig. 2.6(a) and it clearly is physical. The dashed lines carry light-like momentum while the open line is the quark carrying zero momentum ($k = 0$) in the anomaly configuration - this is the quark that, as explained in Appendix B, undergoes the chirality transformation. $l > 0$ gives the process illustrated in Fig. 4.15(b) which, however, is unphysical in that a spacelike gluon appears for longer than on-shell particles.

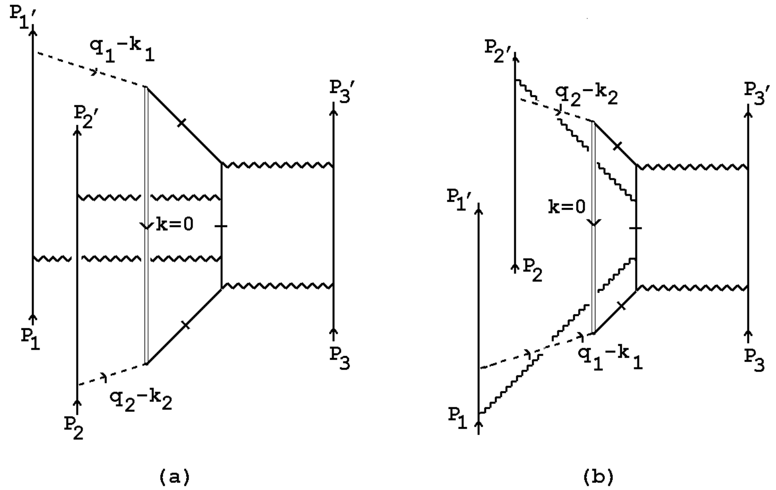

Fig. 4.15 Physical Scattering Processes Involving the Anomaly

The hatched lines in Fig. 4.15(a) are again on-shell and are the same lines that are hatched in Fig. 4.8(a). However, the on-shell lines can not give discontinuities in this configuration. Rather the asymptotic amplitude has to be interpreted as extrapolated away from wherever the discontinuities were taken, as discussed briefly in Section 2. As we will discuss further in the next Section, the dispersion and multi-regge theory that we develop will ultimately justify the initial calculation of a multiple discontinuity corresponding to Fig. 4.8(a) in one part of the physical region and then searching for the anomaly configuration in a different physical region (or different part of the same physical region) with the propagators giving the discontinuity kept on-shell. The important point, at this stage, is that the appropriate momentum configuration for the anomaly divergence does occur and the amplitude involved has reality properties.

To explicitly see the anomaly divergence we add a spacelike momentum of $O(\mathsf{q})$ orthogonal to both $\underline{n}_{lc}$ and $\underline{n}_3$ and let $\mathsf{q} \to 0$ with l fixed. For fixed $\underline{n}_{lc}$ we can choose

$$\underline{\mathsf{q}} \;\sim\; \pm\; \underline{n}_{lc\perp} \;=\; \pm\; (0, -sin\theta_{lc}\;, cos\theta_{lc}\;, 0) \qquad (4.40)$$

It is the component of $q_1 + q_2 + k_1 + k_2$ in this direction that contributes (k_3 can also have a component, but it does not contribute). To evaluate the form of the reggeon interaction (4.21) with $\mathsf{q} \to 0$ as in (4.40), we work in the frame in which the light cone momentum (4.31) can be identified with q_1^+ in (A.5). Projecting each of the $\gamma^{-,-,-\mu}$ on $\underline{n}_{lc}$ gives a factor

$$(1 - cos\theta_{lc} - sin\theta_{lc})^2 \qquad (4.41)$$

and so using (A.6) we obtain

$$\Gamma_6 \;\sim\; \frac{(1 - cos\theta_{lc} - sin\theta_{lc})^2\; l^2\; (q_1 + q_2 + k_1 + k_2) \cdot \underline{n}_{lc\perp}}{\mathsf{q}^2} \;\sim\; \frac{Q_3^2}{\mathsf{q}} \qquad (4.42)$$

which manifestly changes sign when $\underline{n}_{lc\perp} \to -\underline{n}_{lc\perp}$ with $\underline{n}_{lc}$ fixed.

Since contributions with both signs for $\underline{n}_{lc\perp}$ are present in the integral (4.15) of the reggeon interaction, the crucial question is whether there is a cancelation. It is fundamental that, since we integrate over θ_{lc}, the two possibilities are related by a parity transformation interchanging the 1 and 2 axes. The two possibilities are also related by reversing the space component in $\underline{n}_{lc}$ and keeping (4.40) as the orthogonal spacelike momentum. As we discuss in Appendix A, from either perspective the result is the same, the sign of the anomaly contribution is reversed.

In the lowest-order diagrams we have discussed the transverse momentum integrations are sufficient to produce a cancelation. We first integrate over k_3 so that there is a symmetry under $k_3 \leftrightarrow -k_3$. For $l \neq 0$ this is not sufficient to produce a symmetry under $\underline{n}_{lc\perp} \to -\underline{n}_{lc\perp}$. However, if we also integrate over k_1 and k_2 then since the external couplings are simple constants there will also be symmetry under

$q_i+k_i \leftrightarrow q_i-k_i,\ i=1,2$. If we then add the two contributions we have discussed from Fig. 4.8(a) and (b) then all contributions to the amplitude, apart from the anomaly, will be completely symmetric under $1 \leftrightarrow 2$. The antisymmetry of the anomaly then requires that it cancel.

In higher-orders the external reggeon couplings $G_h(q_i,k_i)$ aquire non-trivial momentum dependence. For fixed helicity h these couplings need not be symmetric under $q_i+k_i \leftrightarrow q_i-k_i$. To discuss cancelations in this case it is necessary to add the contributions from the twisted diagrams of Fig. 4.16

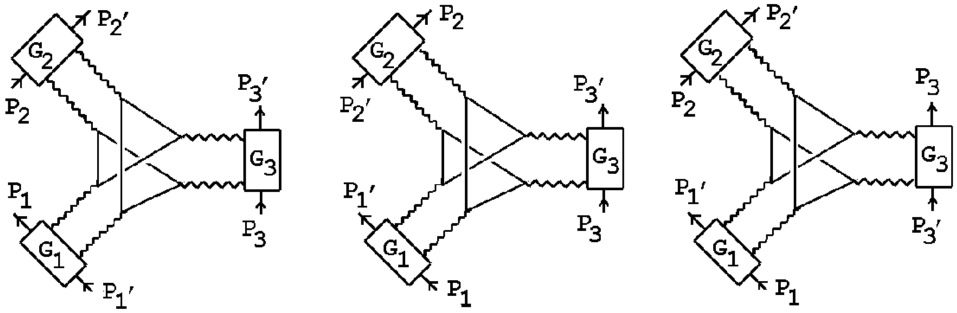

Fig. 4.16 Twisted Diagrams

and also to discuss the signature properties of the reggeon states. If the external couplings have sufficiently asymmetric transverse momentum dependence as might be expected, for example, if they contain the chirality violation produced by an instanton interaction, then the anomaly need not cancel. We will reserve a more extensive discussion of this for Section 7. Here we simply remark that, for elementary quark scattering, both the color factors and all three of the k_i-integrations are symmetric also in higher-orders when we sum over all diagrams of this form and so the anomaly cancelation continues to hold.

Finally, we note that a relatively trivial way to break the transverse momentum symmetries that cancel the anomaly in an individual diagram would be to introduce masses for some, or all, of the gluons. In particular, it would be sufficient if one of each of the pairs of gluons were massive and the other massless. The cancelation would be restored after the summation over all the diagrams of Fig. 4.16 unless the two gluons were distinguished by additional quantum numbers besides their mass. Introducing a gluon mass, of course, requires spontaneous symmetry breaking which would extend our analysis considerably. In fact, the symmetry breaking of the QCD gauge symmetry from SU(3) to SU(2), discussed at several points in this paper, does introduce a massive SU(2) singlet gluon and the required transverse momentum asymmetry is produced when this combines, not with a single massless gluon, but with three massless gluons carrying the quantum numbers of the winding-number current.

5. Multi-Regge Theory

In this Section we describe the asymptotic dispersion relation formalism, together with the multi-regge theory based on it, that is needed to systematically study the contribution of quark loops to triple-regge vertices in QCD. There will be some overlap with Section 4 of [12]. However, the treatment we gave in [12] is missing several crucial elements that we discuss here. As a result, we have made the following essentially self-contained.

5.1 Angular Variables: *s*- and *t*-channel Physical Regions

We begin with the introduction of the angular variables that provide the link between asymptotic limits taken in a direct, or "*s*-channel", and partial-wave analysis in various "cross-channels" or "*t*-channels". We use the variables $z_1, z_2, z_3, u_{12}, u_{23}$ and u_{31} corresponding to the "Toller Diagram" of Fig. 5.1 .

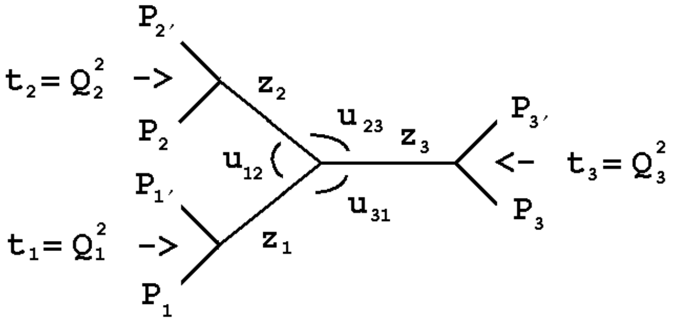

Fig. 5.1 A Toller Diagram for the Six-Particle Amplitude

The definition of these variables via standard Lorentz frames as well as complete expressions for invariant variables in terms of them, is given in Appendix D. We discuss their definition in three *t*-channel physical regions where the t_i are positive and in four *s*-channel physical regions where the t_i are negative. The variables introduced in the different regions are related by analytic continuation. The z_i (and the t_i) are independent variables but since $u_{ij} = e^{\,i\omega_{ij}} = e^{\,i(\nu_i-\nu_j)}$ where each ν_i is an azimuthal angle in the t_i-channel, we have

$$u_{12}\; u_{23}\; u_{31} \;=\; e^{\,i(\nu_1-\nu_2)}\; e^{\,i(\nu_2-\nu_3)}\; e^{\,i(\nu_3-\nu_1)} \;=\; 1 \tag{5.1}$$

Choosing any two of the u_{ij}, together with the t_i and the z_i, gives the appropriate eight independent variables. In the following we will take u_{31} and $u_{32} = u_{23}^{-1}$ as our independent variables and, for simplicity, relabel them as $u_1 = u_{31}$ and $u_2 = u_{32}$.

(5.1) then gives

$$u_{12} \; = \; \frac{u_2}{u_1} \tag{5.2}$$

This choice of u_{ij} variables is appropriate for discussing the particular multiple discontinuities or, in the classification we introduce below, the particular hexagraphs that we focus on in the following. As we will indicate, the alternative choices are appropriate for other hexagraphs.

In principle, since we will be considering the scattering of particles with spin (i.e. quarks) we should add additional azimuthal angles to describe the rotation of helicities. However, as we already saw in the last Section, for the lowest-order quark-gluon couplings there is (s-channel) helicity-conservation. It is trivial to carry out helicity projections and show that the lowest-order couplings are also helicity-independent. In discussing anomaly cancelations at the end of the last Section we saw that the higher-order helicity dependence of these couplings is important. However, we will discuss the consequences of this only qualitatively in Section 7. To keep our discussion in this Section as simple as possible we will treat the scattering quarks kinematically as if they were scalar particles. Also, since this Section will be concerned with abstract kinematics and analyticity properties, we will continue to ignore color (and any other) quantum numbers. In Section 7, both color quantum numbers and the existence of two helicities will be important when we discuss discrete C, P and T transformations on amplitudes. In this Section we will refer only to the CPT combination. Nevertheless the presence of both helicity and color should be kept in mind.

As we show in Appendix D, all invariants are polynomial functions of the $z_i = cos\ \theta_i$, the $sin\ \theta_i$ and the $cos\ \omega_{ij}$ ($u_{ij} = e^{i\ \omega_{ij}}$). The following approximations give the leading behavior when all the z_i are large and are easily derived from (D.17) and (D.18). These approximations will be sufficient for us to describe the behavior of invariants in the limits we discuss.

$$\begin{aligned} s_{122'} \sim s_{1'3'3} \sim -s_{1'22'} \sim -s_{13'3} \quad &\longrightarrow \quad 2\Big(\frac{t_1-4m^2}{t_1}\Big)^{\frac{1}{2}} \lambda^{\frac{1}{2}}(t_1,t_2,t_3)\ z_1 \\ &\sim \quad z_1 \end{aligned} \tag{5.3}$$

$$\begin{aligned} s_{233'} \sim s_{2'1'1} \sim -s_{2'33'} \sim -s_{21'1} \quad &\longrightarrow \quad 2\Big(\frac{t_2-4m^2}{t_2}\Big)^{\frac{1}{2}} \lambda^{\frac{1}{2}}(t_1,t_2,t_3)\ z_2 \\ &\sim \quad z_2 \end{aligned} \tag{5.4}$$

$$\begin{aligned} s_{311'} \sim s_{3'2'2} \sim -s_{3'11'} \sim -s_{32'2} \quad &\longrightarrow \quad 2\Big(\frac{t_3-4m^2}{t_3}\Big)^{\frac{1}{2}} \lambda^{\frac{1}{2}}(t_1,t_2,t_3)\ z_3 \\ &\sim \quad z_3 \end{aligned} \tag{5.5}$$

$$\begin{aligned} s_{13} \quad &\sim \quad s_{1'3'} \quad \sim \quad -\, s_{13'} \quad \sim \quad -\, s_{1'3} \quad \longrightarrow \\ &- \quad 4(t_1 - 4m^2)^{\frac{1}{2}}(t_3 - 4m^2)^{\frac{1}{2}}\Big[(1 - z_1^2)^{\frac{1}{2}}(1 - z_3^2)^{\frac{1}{2}}\Big(u_1 + \frac{1}{u_1}\Big) + \frac{t_3 + t_1 - t_2}{\sqrt{t_1}\sqrt{t_3}} z_1 z_3\Big] \\ &\sim \quad z_1\ z_3\ u_1\ [1 + O(\frac{1}{u_1})] \end{aligned} \tag{5.6}$$

$$\begin{aligned} s_{23} \quad &\sim \quad s_{2'3'} \quad \sim \quad -\, s_{23'} \quad \sim \quad -\, s_{2'3} \quad \longrightarrow \\ &- \quad 4(t_2 - 4m^2)^{\frac{1}{2}}(t_3 - 4m^2)^{\frac{1}{2}}\Big[(1 - z_2^2)^{\frac{1}{2}}(1 - z_3^2)^{\frac{1}{2}}\Big(u_2 + \frac{1}{u_2}\Big) + \frac{t_3 + t_2 - t_1}{\sqrt{t_2}\sqrt{t_3}} z_2 z_3\Big] \\ &\sim \quad z_2\ z_3\ u_2^{-1}\ [1 + O(u_2)] \end{aligned} \tag{5.7}$$

$$\begin{aligned} s_{12} \quad &\sim \quad s_{1'2'} \quad \sim \quad -\, s_{12'} \quad \sim \quad -\, s_{1'2} \quad \longrightarrow \\ &- \quad 4(t_1 - 4m^2)^{\frac{1}{2}}(t_2 - 4m^2)^{\frac{1}{2}}\Big[(1 - z_1^2)^{\frac{1}{2}}(1 - z_2^2)^{\frac{1}{2}}\Big(\frac{u_1}{u_2} + \frac{u_2}{u_1}\Big) + \frac{t_3 - t_1 - t_2}{\sqrt{t_1}\sqrt{t_2}} z_1 z_2\Big] \\ &\sim \quad z_1\ z_2\ (u_1/u_2)\ [1 + O(u_2/u_1)] \end{aligned} \tag{5.8}$$

$\lambda(t_1, t_2, t_3)$ is the familiar triangle function defined explicitly in (D.7). The branch-points at $\lambda(t_1, t_2, t_3) = 0$ in (5.3) - (5.5) play an important role when analytic continuation is discussed, both between the different physical regions and within a fixed s-channel physical region. Note that all invariants are unchanged when $u_1 \to 1/u_1, u_2 \to 1/u_2$.

In each of the three t-channels $t_i = Q_i^2 > 4m^2$ and $\lambda(t_1, t_2, t_3) > 0$. Also, in the particular channel that we refer to as the t_i channel

$$|Q_i| > |Q_j| + |Q_k| \tag{5.9}$$

The choice of signs in (5.3)-(5.5) is a convention which is irrelevant in the t-channels since

$$-1 \ \leq \ z_i \ \leq \ 1, \quad |u_i| \ = \ 1 \tag{5.10}$$

i.e. the z_i take both positive and negative values. Note, however, that the sign convention can be reversed by, for example, interchanging the role of Q_1 and Q_2 when introducing the variables via standard frames defined in the t_3-channel. This is discussed in Appendix D.

In each s-channel physical region there are four sub-regions[11] distinguished by the relative value of the t_i. There are three "$s-t$" regions in which $\lambda(t_1, t_2, t_3) > 0$ and one of the three t-channel constraints (5.9) is satisfied. The "$s-s$" region is the remaining part of the physical region in which $\lambda(t_1, t_2, t_3) < 0$. The relationship between the three t-channels and the sub-regions of one s-channel is illustrated topographically in Fig. D2. For our analysis of anomaly cancelations it is important that a change of sign of all the z_i is equivalent to a change of sign of $\lambda^{\frac{1}{2}}(t_1, t_2, t_3)$. This is apparent from (5.3) - (5.8).

Each of the three $s - t$ sub-regions of the four s-channel physical regions also has two distinct parts, in one of which the z_i each have a certain sign and the other in which they all have the opposite sign. This removes the antisymmetry of the signs in (5.3)-(5.5). Which part of the physical region corresponds to a particular set of signs of the z_i is a convention determined by the choice of sign for $\lambda^{\frac{1}{2}}(t_1, t_2, t_3)$. When the t_i satisfy the $s - t$ sub-region constraint the four s-channel physical regions are

$$\begin{array}{rl} i) & z_1,\ z_2,\ z_3\ \geq\ 1\ , \qquad z_1,\ z_2,\ z_3\ \leq\ -1\ , \quad |u_i|\ =\ 1 \\ & \text{the initial particles carry momenta } P_1, P_2 \text{ and } P_3 \\ ii) & -z_1,\ z_2,\ z_3\ \geq\ 1\ , \qquad -z_1,\ z_2,\ z_3\ \leq\ -1\ , \quad |u_i|\ =\ 1 \\ & \text{the initial particles carry momenta } P_{1'}, P_2 \text{ and } P_3 \\ iii) & z_1,\ -z_2,\ z_3\ \geq\ 1\ , \qquad z_1,\ -z_2,\ z_3\ \leq\ -1\ , \quad |u_i|\ =\ 1 \\ & \text{the initial particles carry momenta } P_1, P_{2'} \text{ and } P_3 \\ iv) & z_1,\ z_2,\ -z_3\ \geq\ 1\ , \qquad z_1,\ z_2,\ -z_3\ \leq\ -1\ , \quad |u_i|\ =\ 1 \\ & \text{the initial particles carry momenta } P_1, P_2 \text{ and } P_{3'} \end{array} \tag{5.11}$$

We will encounter subtleties associated with the doubling of the range of the z_i in individual physical regions at several points in the following. The physical region *i*) is that in which the limits of Section 2 are defined and in which the diagrammatic analysis of the last Section is carried out. That the discontinuities apparently evaluated in Fig. 4.8(a) are no longer present in the region where the anomaly occurs is a particular consequence of the separation of the physical region into two distinct parts.

In the $s - s$ sub-region the physical range of the z_i and u_i in the same four physical regions is

$$\begin{array}{rl} i) & -\infty\ <\ iz_i\ <\infty\ , \quad 0\ \leq\ u_1,\ u_2\ <\ \infty \\ ii) & -\infty\ <\ iz_i\ <\infty\ , \quad 0\ \leq\ -u_1,\ u_2\ <\ \infty \\ iii) & -\infty\ <\ iz_i\ <\infty\ , \quad 0\ \leq\ u_1,\ -u_2\ <\ \infty \\ iv) & -\infty\ <\ iz_i\ <\infty\ , \quad 0\ \leq\ -u_1,\ -u_2\ <\ \infty \end{array} \tag{5.12}$$

Clearly the kinematic structure of the s-channel physical regions is quite complicated. This is reflected in the variety of kinematic limits that can be taken. Nevertheless, all the limits are described by the same multi-regge theory.

5.2 Definition of Limits via Angular Variables

The full triple-regge limit is defined to be

$$z_1,\ z_2,\ z_3\ \rightarrow\ \infty\ , \quad t_1, t_2, t_3, u_1, u_2\ \ fixed \tag{5.13}$$

Helicity-pole limits are those in which one or two of the u_{ij} are taken either large or small. This can be, but need not be, combined with taking one or more of the z_i large.

We will distinguish two distinct helicity-pole limits involving u_1 and u_2. The first is

$$z_3,\ u_1,\ u_2\ \rightarrow\ \infty\ \ (\text{or } u_1, u_2 \rightarrow 0) \quad t_1, t_2, t_3, z_1, z_2\ \ fixed \tag{5.14}$$

When applied to the relevant discontinuity (with P_1 and P_2, and P_1' and P_2', respectively identified) this limit coincides with the familiar (incorrectly named) "triple-regge" limit of the one-particle inclusive cross-section. The second helicity-pole limit is

$$z_3,\ u_1,\ u_2^{-1}\ \rightarrow\ \infty\ \ (\text{or } u_1, u_2^{-1} \rightarrow 0) \quad t_1, t_2, t_3, z_1, z_2\ \ fixed \tag{5.15}$$

For reasons that will soon become apparent, we refer to the limit (5.14) as the "non-flip limit" and the limit (5.15) as the "helicity-flip limit". The helicity-pole limits are formulated in terms of the u_{ij} variables we have chosen and, as we discuss further below, they are controled by singularities in corresponding complex helicity planes directly related to angular momentum plane Regge singularitites. Clearly we can define corresponding limits for any choice of the u_{ij}.

In an $s{-}t$ part of an s-channel physical region the triple-regge limit is a physical limit but the helicity-pole limits are not. In the $s - s$ region both the triple-regge limit and the helicity-pole limits are physical. With the approximations (5.3) - (5.8) the inter-relation between the helicity-pole limits (5.14) and (5.15) and the triple-Regge limit (5.13) is apparent. It is also straightforward, using (3.4), to identify the triple-Regge limit (5.13) and the light-cone formulated limit (3.1). Clearly

$$P_1\ \sim\ z_1\ , \quad P_2\ \sim\ z_2\ , \quad P_3\ \sim\ z_3\ . \tag{5.16}$$

For the helicity non-flip limit (5.14) we have, from (5.3) - (5.8),

$$s_{12}\quad \sim \quad s_{1'2'}\ \sim\ \ -\, s_{12'}\ \sim\ \ -\, s_{1'2} \not\rightarrow \infty \tag{5.17}$$

$$s_{23}\quad \sim \quad -\, s_{2'3}\ \sim\ z_3\ u_2\ , \quad s_{31}\ \sim\ s_{3'1}\ \sim\ z_3\ u_1 \tag{5.18}$$

$$s_{122'}\ ,\ s_{133'}\ ,\ s_{233'} \not\rightarrow \infty\ . \quad s_{311'}\ \sim s_{3'22'}\ \sim\ z_3 \tag{5.19}$$

Because $s_{12} \not\rightarrow \infty$ we can not reproduce the non-flip limit (5.14) with the light-cone variables of (3.1). However, for the helicity limit (5.15), the behavior (5.17) is replaced by

$$s_{12}\ \sim\ s_{1'2'}\ \sim\ \ -\, s_{12'}\ \sim\ \ -\, s_{1'2}\ \sim\ u_1\ u_2^{-1} \tag{5.20}$$

Therefore, we can formulate the helicity-flip limit in terms of the variables of (3.1) as

$$P_1 \sim u_1 \ , \quad P_2 \sim u_2^{-1} \ , \quad P_3 \sim z_3 \ . \tag{5.21}$$

together with

$$\begin{gathered} q_{12^-} = \hat{q}_1 - q_{12} = q_{32} - \hat{q}_3 \to 0 \ , \quad q_{21^-} = \hat{q}_2 - q_{21} = q_{31} - \hat{q}_3 \to \\ \hat{q}_1 - q_{13} \not\to 0 \ , \quad \hat{q}_2 - q_{23} \not\to 0 \end{gathered} \tag{5.22}$$

We can also take the helicity-flip limit (5.15) in conjunction with the triple-regge limit so that

$$z_1, \ z_2, \ z_3, \ u_1 \, u_2^{-1} \ \to \ \infty \ , \quad t_1, t_2, t_3, \ \ \textit{fixed} \tag{5.23}$$

Note, from (5.6)-(5.8), that in this last limit

$$s_{23} \sim z_3 \, u_2^{-1} \ , \quad s_{31} \sim z_3 \, u_1 \ , \quad s_{12} \sim z_1 \, u_1 \, z_2 \, u_2^{-1} \tag{5.24}$$

and so if $z_1 \sim z_2 \sim z_3$ then

$$s_{23}, \ s_{13} \ << \ s_{12} \tag{5.25}$$

It is important to keep account of the t_1 and t_2 dependance in (5.3)-(5.8) when the limit (5.23) is taken with $t_1, t_2 \sim 0$. Therefore, using (3.5) and (3.6) we can write (for small q_{21^-}, q_{12^-})

$$u_1 \sqrt{t_1} \ + \ O(1) \ \sim \ \frac{s_{13}}{s_{133'} \ s_{311'}} \quad => \quad u_1 \ \sim \ \frac{1}{\sqrt{t_1} \ \ q_{21^-}} \tag{5.26}$$

$$u_2^{-1} \sqrt{t_2} \ + \ O(1) \ \sim \ \frac{s_{23}}{s_{233'} \ s_{322'}} \quad => \quad u_2^{-1} \ \sim \ \frac{1}{\sqrt{t_2} \ \ q_{12^-}} \tag{5.27}$$

As we will see below, the helicity-flip limit selects leading (flipped) helicities from the full triple-Regge vertex. (The non-flip limit similarly selects non-flipped leading helicities). (5.26) and (5.27) imply that while the helicity-flip is directly expressed as

$$q_{12^-} \ , \ q_{21^-} \ \to \ 0 \ , \qquad t_1 = q_1^2, \ t_2 = q_2^2, \ \textit{fixed} \tag{5.28}$$

this limit is also reached if

$$q_1^2 \ , \ q_2^2 \ \to \ 0 \ , \qquad q_{12^-}, \ q_{21^-}, \ t_3 \ \ \textit{fixed} \tag{5.29}$$

5.3 Dispersion Theory and Asymptotic Cut Structure

A fundamental ingredient for our multi-regge analysis is the existence[2, 14] of an “asymptotic dispersion relation” that breaks the full triple-regge asymptotic amplitude up into components that each have a distinct set of asymptotic cuts. The dispersion relation is written in z_1, z_2 and z_3 with t_1, t_2, t_3, u_1 and u_2 kept fixed. It is initially written with all the $t_i < 0$ and with $\lambda(t_1, t_2, t_3) > 0$ so that physical contributions are obtained from an $s-t$ region of each of the four s-channels. However, we expect the form of the dispersion relation to remain unchanged as we continue between s-channel sub-regions and also to the t_i-channels.

The most important feature[2, 14] is that the asymptotic cut structure of multiple discontinuities can be treated as if there were only normal threshold cuts satisfying the Steinmann relations. i.e. no double discontinuities in overlapping channels. This asymptotic structure, in turn, matches naturally with the asymptotic formulae obtained from multi-regge theory. At a fundamental level, this match is presumably a consequence of the close relationship between multi-regge analyticity and the primitive analyticity domains of field theory, i.e. the simple off-shell analyticity properties of field theory survive asymptotically on-shell[18]. In physical regions the asymptotic validity of the Steinmann relations can be derived within S-Matrix Theory by showing that the "bad boundary-values" in which a variety of complications due to higher-order singularities appear, are hidden in multi-regge limits. In the particular dispersion relation that we use in this paper an additional fundamental complication arises in that there are essential contributions from non-physical triple discontinuities.

The discontinuities involved are physical in two-four scattering processes, but not in the three-three processes we discuss. As a matter of principle, the presence of discontinuities outside the physical region, as well as their explicit form, can not be discussed directly from an S-Matrix starting-point. However, as we alluded to above, the dispersion relation can also be based on the field theory formalism of Generalised Retarded Functions, by starting with spacelike masses and utilising the primitive analyticity domains[18, 19]. The asymptotic structure of the dispersion relation should persist straightforwardly on-shell, with the standard discontinuity formulae holding. The triple discontinuities that are unphysical in our problem will appear directly in the field theory formulation just because they satisfy the Steinmann relations. As we will see, these discontinuities are manifestly present in Feynman diagrams and they are esssential to obtain consistent multi-regge behavior. In fact, as we have already noted several times, they are crucial for the appearance of the anomaly.

The Steinmann relations are not satisfied by individual Feynman graphs and it is a subtle feature that they emerge asymptotically. As a consequence the matching of multi-regge behavior with features of the graphs studied in the previous and succeeding chapters will also be subtle. In particular, as we noted above, in our discussion of the anomaly configuration of Fig. 4.15 we found that discontinuities present in one part of the physical region, and represented by Fig. 4.8(a), are no longer present in another part. A property that is only possible because of the violation of the Steinmann relations by the graphs involved. (The turning off of the branch-cuts involved requires the existence of simultaneous singularities in additional variables that are forbidden by the Steinmann relations.)

The dispersion relation gives the leading triple-regge behavior (up to powers) as a sum over triple discontinuity contributions allowed by the Steinmann relations, i.e. we can write

$$M(P_1,P_2,P_3,Q_1,Q_2,Q_3) \;=\; \sum_{\mathcal{C}} M^{\mathcal{C}}(P_1,P_2,P_3,Q_1,Q_2,Q_3) \;+\; M^0 \;, \qquad (5.30)$$

M^0 contains all non-leading triple-regge behavior, double-regge behavior, etc. and the sum is over all triplets $\mathcal{C}$ of three non-overlapping, asymptotically distinct, cuts. For each triplet $\mathcal{C}$ of cuts in invariants, say $\mathcal{C} = (s_1, s_2, s_3)$, we write

$$M^{\mathcal{C}}(P_1,P_2,P_3,Q_1,Q_2,Q_3) \;=\; \frac{1}{(2\pi i)^3} \int\limits_{\{s_i > s_{i0}, \forall i\}} ds_1' ds_2' ds_3' \; \frac{\Delta^{\mathcal{C}}(\underset{\sim}{t}, \underset{\sim}{u}, s_1', s_2', s_3')}{(s_1'-s_1)(s_2'-s_2)(s_3'-s_3)} \qquad (5.31)$$

where $\Delta^{\mathcal{C}}$ is the triple discontinuity

$$\Delta^{\mathcal{C}}(\underset{\sim}{t}, \underset{\sim}{u}, s_1, s_2, s_{n-3}) \;=\; \sum_{\epsilon} (-1)^{\epsilon} M(\underset{\sim}{t}, \underset{\sim}{w}, s_1 \pm i0, s_2 \pm i0, s_3 \pm i0), \qquad (5.32)$$

The sum over ϵ is over all combinations of $+$ and $-$ signs in (5.32) and $(-1)^{\epsilon}$ is positive when the number of $+$ signs is even. The integration region in (5.31) is bounded by finite, but arbitrary, values s_{i0} of the s_i and the asymptotic relation between the z_i, and s_i has to be used to change variables from the z_i back to the s_i. Because of the validity of the Steinmann relations, $\Delta^{\mathcal{C}}$ can be expressed in terms of normal phase-space integrals. Therefore, we can take multiple discontinuities simply by putting appropriate lines on mass-shell. (For the low-order Feynman diagrams we discuss the subtlety of the boundary values for the amplitudes in the discontinuity formulae[14] will not appear.)

5.4 Triple Discontinuities

If we consider only the z_i dependence, the asymptotic relations (5.3)-(5.8) reduce to

$$\begin{array}{rcccccccc}
s_{122'} & \sim & s_{1'3'3} & \sim & -\,s_{1'22'} & \sim & -\,s_{13'3} & \sim & z_1 \\
s_{233'} & \sim & s_{2'1'1} & \sim & -\,s_{2'33'} & \sim & -\,s_{21'1} & \sim & z_2 \\
s_{311'} & \sim & s_{3'2'2} & \sim & -\,s_{3'11'} & \sim & -\,s_{32'2} & \sim & z_3 \\
s_{13} & \sim & s_{1'3'} & \sim & -\,s_{13'} & \sim & -\,s_{1'3} & \sim & z_1\, z_3 \\
s_{23} & \sim & s_{2'3'} & \sim & -\,s_{23'} & \sim & -\,s_{2'3} & \sim & z_2\, z_3 \\
s_{12} & \sim & s_{1'2'} & \sim & -\,s_{12'} & \sim & -\,s_{1'2} & \sim & z_1\, z_2
\end{array} \qquad (5.33)$$

As we discussed in Section 2, the triple discontinuities are of three kinds corresponding to the tree diagrams of Figs. 2.9(a), (b) and (c). These are the distinct possibilities consistent with the Steinmann relations. An example of the Fig. 2.9(a) kind is

$$\mathcal{C}_a \;=\; (s_{13}, s_{2'3'}, s_{11'3}) \tag{5.34}$$

From (5.33), the invariants of $\mathcal{C}_a$ are large and positive when

$$z_1z_3,\;\; z_2z_3,\;\; z_3\;\; >> 1 \quad \leftrightarrow \quad z_1,\;\; z_2,\;\; z_3\;\; >> 1 \tag{5.35}$$

giving a unique product of (asymptotic) z_i half-axes lying in the first part of the i) physical region in (5.11). All triplets of the Fig. 2.9(a) kind similarly correspond to a unique product of (asymptotic) z_i half-axes. There are 6 possible combinations of initial and final subenergies so there are 6 triple discontinuities of this kind in each physical region, three in each part, making a total of 24.

A triplet having the form of Fig. 2.9(b) is

$$\mathcal{C}_b \;=\; (s_{13}, s_{2'3'}, s_{123}) \tag{5.36}$$

Since

$$s_{123} \;=\; s_{31} \;+\; s_{12} \;+\; s_{23} \;-\; 3m^2 \tag{5.37}$$

(where m is the mass of the scattering particles) the cut in s_{123} will be distinguished from the asymptotic cuts in s_{31} and s_{23} only when s_{12} is large. Consequently, the contribution of the s_{123} cut, as a distinct asymptotic cut, is effectively as a cut in s_{12} (particularly in the helicity-pole limit discussed below in which $s_{12} >> s_{13}, s_{23}$). In the following, therefore, we will use (5.8) also as an approximation for s_{123}. In this case, the invariants of $\mathcal{C}_b$ are large and positive when

$$z_1z_3,\;\; z_2z_3,\;\; z_1z_2\;\; >> 1 \quad \leftrightarrow \quad z_1,\;\; z_2,\;\; z_3\;\; >> 1\;, \quad z_1,\;\; z_2,\;\; z_3\;\; << -1 \tag{5.38}$$

Now there are two regions for each triplet, one in each part of the relevant physical region. A closely related complication is that the invariants in the triplet

$$\mathcal{C}_{b'} \;=\; (s_{1'3'}, s_{23}, s_{1'2'3'}) \tag{5.39}$$

are also real and positive in the two regions of (5.35). The two sets of cuts $\mathcal{C}_b$ and $\mathcal{C}_{b'}$ both satisfy the Steinmann relations. Since they are asymptotically equivalent the multi-regge representations we derive will not be able to distinguish between them. (Their existence, however, is another feature that is crucial for the potential appearance of the anomaly.) If we start from Feynman graphs each triple discontinuity has to be computed separately and added to the dispersion relation. All triple discontinuities of this kind similarly occur in equivalent pairs and also appear in both parts of the physical region involved. Since each triplet is again characterised by an initial and final subenergy there are 24 in total, or twelve equivalent pairs - three in each physical region.

A triplet of the Fig. 2.9(c) kind is

$$\mathcal{C}_c \;=\; (s_{13}, s_{2'3'}, s_{1'2}) \tag{5.40}$$

These three invariants are not all positive in any physical region. However, they are all positive if

$$z_1z_3,\; z_2z_3,\; -z_1z_2 \;>>1 \;\leftrightarrow\; -iz_1,\; -iz_2,\; iz_3 \;>>1\,,\;\; iz_1,\; iz_2,\; -iz_3 \;<<-1 \tag{5.41}$$

Therefore each triplet of this kind gives two unphysical region contributions (on the asymptotic imaginary axes) to the asymptotic dispersion relation. For the discontinuities to have physical intermediate states, the invariants should satisfy one of the constraints

$$s_{13} \;\geq (\sqrt{s_{2'3'}}+\sqrt{s_{1'2}})^2\;, \quad s_{2'3'} \;\geq (\sqrt{s_{13}}+\sqrt{s_{1'2}})^2\;, \quad s_{1'2} \;\geq (\sqrt{s_{2'3'}}+\sqrt{s_{13}})^2 \tag{5.42}$$

This separates the triple discontinuity (5.40) into three components in each of the physical regions. This separation is clearly well-defined in the (helicity-pole) limit in which one of the invariants is much larger than the other two and this will be sufficient for our purposes. The triplet

$$\mathcal{C}_{c'} \;=\; (s_{1'3'}, s_{23}, s_{12'}) \tag{5.43}$$

is asymptotically equivalent to the triplet $\mathcal{C}_c$. Indeed, apart from their occurrence in unphysical regions, the triplets of the Fig. 2.9(c) kind share all the doubling and pair-wise equivalence properties of the Fig. 2.9(b) kind. We will see that the two kinds have closely related asymptotic representations.

Each of the asymptotic equivalences we have discussed identifies initial and final state discontinuities. Such discontinuities typically arise from distinct contributions in individual Feynman graphs. However, the multi-regge theory we will develop requires the multiple discontinuities to be closely related. Note that when the physical range for the z_i is pure imaginary, in an $s-s$ sub-region, each unphysical triple discontinuity region asymptotes to the real axes on which a physical region appears in the $s-t$ subregions. This will mean that the standard definition of signatured amplitudes can be applied for the unphysical triplets in the $s-s$ regions.

5.5 Hexagraph Notation for Triple Discontinuities

To develop our multi-regge analysis we introduce a "hexagraph" notation[2, 14] for classifying the triple discontinuities. The hexagraphs link each triple discontinuity to a particular t-channel and determines it's contribution to asymptotic behavior via a Sommerfeld-Watson representation. Our inclusion of the unphysical triple discontinuities will involve conventions that may appear somewhat arbitrary but it will be clear that the asymptotic representations we eventually obtain for both the Fig. 2.9(b) and the Fig. 2.9(c) triple discontinuities are essentially independent of how they are mapped onto the hexagraph formalism.

The full sum over triple discontinuities in (5.30) is broken up into partial sums forming a hexagraph amplitude. Each hexagraph amplitude M^H contains a sum of triple discontinuity integrals, i.e.

$$M^H = \sum_{\mathcal{C} \epsilon H} M^{\mathcal{C}}(P_1, P_2, P_3, Q_1, Q_2, Q_3), \tag{5.44}$$

where the sum is over all triplets $\mathcal{C}$ of asymptotic cuts in which each cut is an "allowable discontinuity" of the hexagraph H.

The hexagraphs associated with a particular Toller diagram are obtained by redrawing the tree diagram in all possible ways (in a plane) with the internal lines drawn as horizontal lines and the internal vertices drawn separately, with relative angles of 120^o, and joined to the horizontal lines. For the Toller diagram of Fig. 5.1 we draw an initial hexagraph, say the first graph of Fig. 5.2, and then form the additional graphs of Fig. 5.2 by cyclical rotation of the t_i-channels.

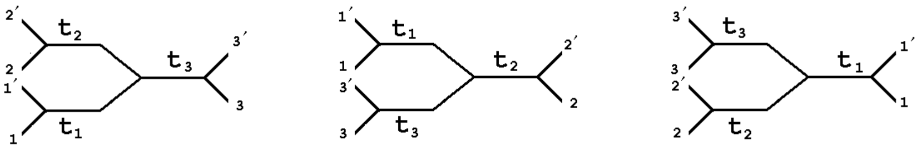

Fig. 5.2 Hexagraphs Related by Cyclical Rotation of the t_i-channels

Hexagraphs have many uses in addition to the classification of discontinuities that we describe below. One of the simplest is that, as we noted above, an independent set of angular variables (and their conjugate angular momentum and helicity variables) can be put in one-to-one correspondence with the lines of the graph[††]. The z_i (and conjugate J_i) variables can be associated with the horizontal lines while an independent set of the u_{ij} can be associated with the sloping lines. Helicity-pole limits can then also be associated directly with a hexagraph. For the first hexagraph of Fig. 5.2 (and all those of Fig. 5.3) the u_1 and u_2 variables used above are naturally associated with the sloping lines, while for the other two graphs in Fig. 5.2 one of the alternative choices of the u_{ij} is appropriate.

[††] Although we will make only minimal reference to it in this paper, this correspondence plays a vital role in all aspects of the multi-regge theory for a general multiparticle amplitude.

We form a further set of hexagraphs from each of those shown in Fig. 5.2 by making twists (of one half of the graph relative to the other) about each of the horizontal lines of the graph. In Fig. 5.3 we have shown again the first hexagraph of Fig. 5.2 together with the seven hexagraphs related to it by twisting. Twisting also the other two hexagraphs in Fig. 5.2 gives a total of $(2 \times 2 \times 2 = 8) \times 3 = 24$ which is the total number of hexagraphs associated with the Toller diagram of Fig. 5.1.

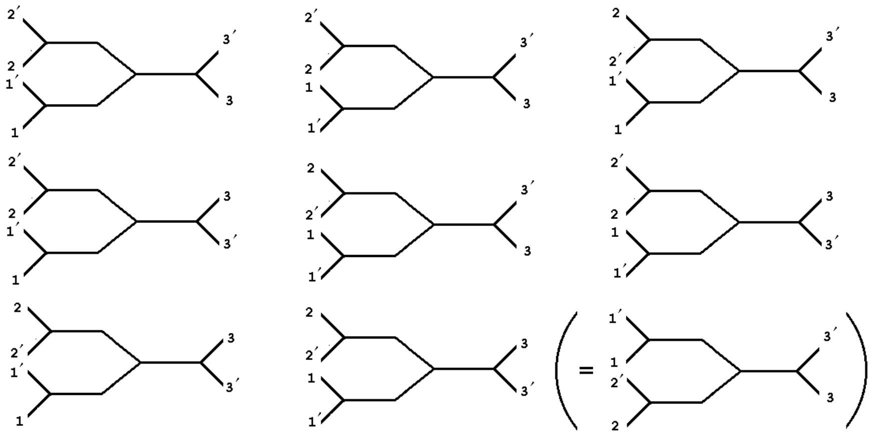

Fig. 5.3 Eight Hexagraphs Related by Twisting

The multiple discontinuities associated with a particular hexagraph all appear in (or, in the case of the unphysical discontinuities, are associated with) the same part of a particular s-channel physical region, which we therefore associate directly with the graph. The physical region involved is obtained by regarding the external scattering particles as entering from the bottom of the hexagraph and exiting at the top. (In a loose way, the hexagraph represents a time-ordering in the scattering with the time axis vertical on the page.) Each hexagraph is also associated with a particular t-channel. This channel is obtained by interpreting the graph as representing a scattering in which external particles enter from the left of the hexagraph and exit to the right. A twist of a hexagraph produces a change of s-channel, but leaves the t-channel unchanged.

Each of the three hexagraphs in Fig. 5.2 is associated with the same part of the same s-channel which, with the conventions we have chosen, is $z_1, z_2, z_3 \geq 1$, i.e. the first part of region i) of (5.11). The first is associated with the t-channel in which $|Q_3| > |Q_1| + |Q_2|$, as are all the graphs of Fig. 5.3. The second and third graphs in Fig. 5.2 are associated, repectively, with the t-channels in which $|Q_2| > |Q_1| + |Q_3|$ and $|Q_1| > |Q_3| + |Q_2|$. Twisting similarly generates all the other graphs associated with these t-channels giving, finally, 3 hexagraphs for each part of each s-channel and 8 hexagraphs for each t-channel.

The partial-wave analysis that follows this sub-section, introducing complex angular momenta and helicities, is carried out in the t-channel. A twist gives a change of sign of the z_i (and, if it exists, the u_i) associated with the chosen line and so is associated with signature. We do not distinguish scattering processes related by a CPT transformation which interchanges all incoming particles with all outgoing particles. We could equally well regard the s-channel scattering particles as entering from the top of the diagram and the t-channel scattering particles as entering from the right of the diagram. (Although, as we noted at the beginning of this Section, it is important to note that there are helicities and color quantum numbers that distinguish the amplitudes related by a CPT transformation.)

In Fig. 5.3 we have also shown the CPT reversed version of the last hexagraph to emphasize that the associated s-channel is the same as that of the first hexagraph, but with the 1 and 2 t-channels interchanged. As a result, although our choice of an initial hexagraph appears to treat the 1 and 2 channels differently, this distinction is removed (up to a sign convention) once we have formed the complete set of graphs. That the combination of twists in all three channels does not result in a new s-channel is the same phenomenon, already noted, that (in an $s-t$ sub-region) there are two distinct z_i-plane regions in each s-channel in (5.11). A change of the sign of all three z_i is equivalent to remaining in the same physical region and changing the sign of $\lambda^{\frac{1}{2}}(t_1,t_2,t_3)$ or, equivalently, interchanging the role of 1 and 2 in the t_3-channel associated with this set of hexagraphs. (In an $s-s$ sub-region, the effect is equivalent to the (parity) transformation of inverting, in space, the triangle formed by Q_1, Q_2 and Q_3. This is the same parity transformation that we discussed as relevant for anomaly cancelations in the previous Section.)

The rules for associating cuts with hexagraphs are as follows. A cut of a hexagraph is any path drawn through the graph (along internal lines), that enters and exits only between non-horizontal lines. This cut defines an invariant channel corresponding to all the particles emitted above (or absorbed below) the cut. An asymptotic cut is an "allowable discontinuity" of a hexagraph if it is asymptotically equivalent to a cut of the hexagraph. The cuts of the first hexagraph of Fig. 5.3 are shown in Fig. 5.4, together with the corresponding allowable discontinuities To include unphysical discontinuities in the hexagraph formalism we adopt the convention that a cut passing through a vertex via only the sloping lines (the last cut in Fig. 5.4) induces a reversal of incoming and outgoing particles on one or other of the two parts of the cut separated by the vertex. (We believe this convention will generalise appropriately to more complicated hexagraps, but we have not studied this in detail.)

To form a triplet $\mathcal{C}$ the three cuts must be "asymptotically distinct" from each other and also satisfy the Steinmann relations. A first triplet formed from the cuts of Fig. 5.4 is the set $\mathcal{C}_a$ in (5.34) above and a second triplet is $\mathcal{C}_b$ in (5.36). The asymptotically equivalent triplet $\mathcal{C}_{b'}$ is also present, as are the triplet $\mathcal{C}_c$ involving the unphysical cut $s_{1'2}$ and the asymptotically equivalent triplet $\mathcal{C}_{c'}$. Up to asymptotic equivalence one of each of the three kinds of triplets identified in Fig. 2.9 is associated with the hexagraph we have chosen. For $\mathcal{C}_b$ and $\mathcal{C}_{b'}$ we associate only the triple discontinuity in region $z_1, z_2, z_3 > 1$ with the hexagraph. (The triple discontinuity in $z_1, z_2, z_3 < -1$ is associated with the hexagraph obtained by three twists.) For $\mathcal{C}_c$ and $\mathcal{C}_{c'}$ we associate only the triple discontinuity in the region $Imz_1, Imz_2, -Imz_3 > 1$ with the hexagraph (with the triple discontinuity in $Imz_1, Imz_2, -Imz_3 < -1$ associated with the hexagraph obtained by three twists.)

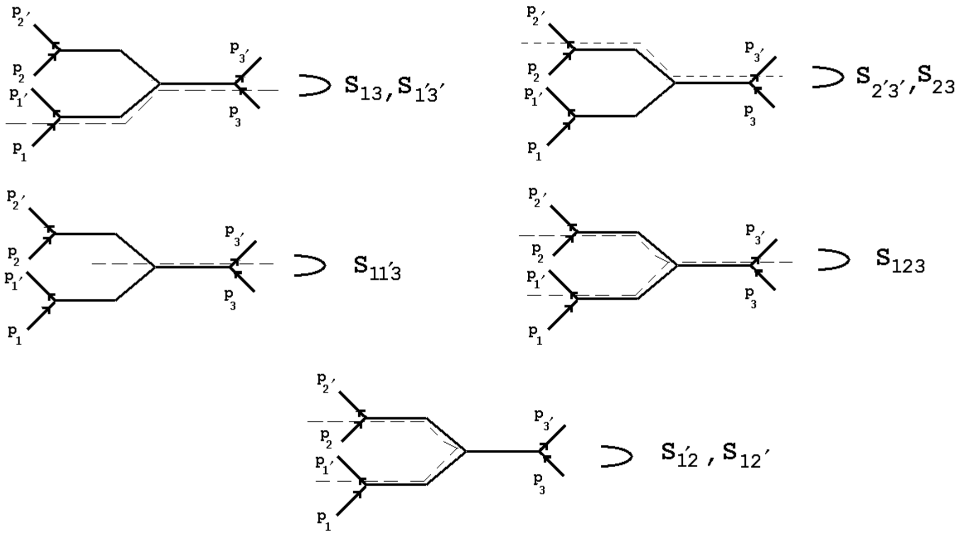
$p_{2'}$
p_2
$p_{1'}$
p_1
$p_{3'}$
p_3
$\supset s_{13}, s_{1'3'}$
$\supset s_{2'3'}, s_{23}$
$\supset s_{11'3}$
$\supset s_{123}$
$\supset s_{1'2}, s_{12'}$

Fig. 5.4 Cuts and Allowable Discontinuities for the First Hexagraph of Fig. 5.3.

If we now consider the last hexagraph of Fig. 5.3 (associated with the regions $z_1, z_2, z_3 \leq -1$ and $Imz_1, Imz_2, -Imz_3 < -1)$) the triplet $\mathcal{C}_a$ is replaced by

$$\mathcal{C}_{a'} \;=\; (s_{1'3'}, s_{23}, s_{11'3'}) \tag{5.45}$$

The triplets $\mathcal{C}_b, \mathcal{C}_{b'}, \mathcal{C}_c$ and $\mathcal{C}_{c'}$ again appear. However, as we stated above, we keep only the triple discontinuities in $z_1, z_2, z_3 < -1$ and $Imz_1, Imz_2, -Imz_3 < -1$. With the convention that we have adopted for the unphysical discontinuities, the initial and final state double discontinuity $(s_{13}, s_{2'3'})$ characterises all three kinds of triplets and can therefore be used to identify the hexagraph. We will use this identification in the next Section. Consequently, if the hatched lines of Fig. 4.8(a) are placed on-shell by taking discontinuities in (s_{13} and $s_{2'3'}$) then the amplitude obtained is associated with the hexagraph of Fig. 5.4.

In summary, there are three asymptotically distinct sets of cuts uniquely associated with each hexagraph. The triplet having the form of $\mathcal{C}_a$ determines the product of z_i axes to be associated with the hexagraph (the $s_{ijk'}$ invariant involved must be positive) and also the invariants used to describe the remaining cuts. The remaining cuts are each pairwise equivalent and appear in two parts of a physical region. Consequently, from the total of 24 hexagraphs there are 48 asymptotically distinct triple discontinuities contributing to the dispersion relation.

For $M^{\mathcal{C}_a}$ we can write straightforwardly

$$M^{\mathcal{C}_a} \;=\; \frac{1}{(2\pi i)^3}\int \frac{ds'_{13}ds'_{2'3'}ds'_{11'3}\Delta^{\mathcal{C}_a}(\underset{\sim}{t},\underset{\sim}{u},s'_{13},s'_{2'3'},s'_{11'3})}{(s'_{13}-s_{13})(s'_{2'3'}-s_{2'3'})(s'_{11'3}-s_{11'3})} \tag{5.46}$$

where the integration region can be taken as $\{z_1, z_2, z_3 \; > z_0\}$. It follows from the representation (5.46) that for small $s_{13}, s_{2',3'}$ and $s_{11'3}$, $M^{\mathcal{C}_a}$ can be expanded as

$$M^{\mathcal{C}_a} \;=\; \sum_{m,n,r=0}^{\infty} c^a_{mnr}\; s^m_{13}\; s^n_{2'3'}\; s^r_{123} \tag{5.47}$$

where the c^a_{mnr} are functions of the u_i and t_i only. The analogues of $M^{\mathcal{C}_a}$ for each of the hexagraphs have analagous representations and expansions. The expansion (5.47) places an important constraint on our partial-wave analysis in the next sub-section.

For $M^{\mathcal{C}_b}$ we can write

$$M^{\mathcal{C}_b} = \frac{1}{(2\pi i)^3}\int \frac{ds'_{13}ds'_{2'3'}ds'_{123}\Delta^{\mathcal{C}_b}(\underset{\sim}{t},\underset{\sim}{u},s'_{13},s'_{2'3'},s'_{123})}{(s'_{13}-s_{13})(s'_{2'3'}-s_{2'3'})(s'_{123}-s_{123})} \tag{5.48}$$

but the integration region has two components, $(\{z_1, z_2, z_3 \; > z_0\})$ contributing to one hexagraph and $(\{z_1, z_2, z_3 \; < -z_0\})$ contributing to the other. For small $s_{13}, s_{2'3'}, s_{123}$, (5.48) gives the expansion

$$M^{\mathcal{C}_b} \;=\; \sum_{m,n,r=0}^{\infty} c^b_{mnr}\; s^m_{13}\; s^n_{2'3'}\; s^r_{11'3} \tag{5.49}$$

This expansion has strong implications for the partial-wave expansions that we discuss next. $M^{\mathcal{C}_{b'}}$ has an identical representation to $M^{\mathcal{C}_b}$. $M^{\mathcal{C}_c}$ and $M^{\mathcal{C}_{c'}}$ have analagous representations to (5.48) but with the integration regions $\{Im\ z_1, Im\ z_2, -Im\ z_3 \; > Im\ z_0\}$ and $\{Im\ z_1, Im\ z_2, -Im\ z_3 \; < -Im\ z_0\}$. The expansions corresponding to (5.49) will have the same strong implications.

5.6 Partial-Wave Expansions

To develop the multi-regge theory associated with the Toller diagram of Fig. 5.1 we begin by writing a partial-wave expansion for each set of hexagraph amplitudes that are related by twisting and, therefore, have the same t-channel. For the set of amplitudes corresponding to the hexagraphs of Fig. 5.3 we write

$$\sum_{H} M^{H}(z_1, z_2, z_3, u_1, u_2) = \sum_{\substack{J_1, J_2, J_3 = 0 \\ |n_1| \leq J_1, |n_2| \leq J_2 \\ |n_1 + n_2| \leq J_3}}^{\infty} d^{J_1}_{0,n_1}(z_1)\, d^{J_2}_{0,n_2}(z_2)\, d^{J_3}_{-n_1-n_2,0}(z_3)\, u_1^{n_1} u_2^{n_2} a_{\underset{\sim}{J},\underset{\sim}{n}} \tag{5.50}$$

Our analysis will be focussed on the sub-series in (5.50) with $n_1, -n_2 > 0$ and $n_2, -n_1 > 0$. In our notation n_1 and $-n_2$ are center-of-mass helicities in the t_3-channel. Therefore, if n_1 and n_2 have opposite signs, this corresponds to same sign "t-channel" helicities and therefore (at "zero mass" $\equiv t_1$ or $t_2 = 0$)) to opposite sign "s-channel" helicities. For this reason, we will refer to amplitudes with opposite signs for n_1 and n_2 as "helicity-flip" amplitudes.

Writing (5.50) for $M^{\mathcal{C}_a}$ we can compare the expansion obtained with the expansion (5.47). In the same leading-power approximation that gives (5.3) - (5.8), we can write

$$\begin{aligned} d^{J_1}_{0,n_1}(z_1)\, d^{J_2}_{0,n_2}(z_2)\, d^{J_3}_{-n_1-n_2,0}(z_3)\, u_1^{n_1} u_2^{n_2} \quad &\sim \quad z_1^{J_1} z_2^{J_2} z_3^{J_3} u_1^{n_1} u_2^{n_2} \\ &= \quad (z_1 z_3 u_1)^{J_1} (z_2 z_3 u_2^{-1})^{J_2} z_3^{J_3 - J_1 - J_2}\; u_1^{n_1 - J_1}\; u_2^{J_2 - n_2} \end{aligned} \tag{5.51}$$

Using (5.3) - (5.7) we can therefore write

$$\begin{aligned} d^{J_1}_{0,n_1}(z_1)\, d^{J_2}_{0,n_2}(z_2)\, d^{J_3}_{-n_1-n_2,0}(z_3)\, u_1^{n_1} u_2^{n_2} \quad &\sim \quad (s_{13})^{J_1} (s_{2'3'})^{J_2} (s_{11'3})^{J_3 - J_1 - J_2} \\ &\qquad \times c_a(u_1, u_2) \end{aligned} \tag{5.52}$$

Since we must have a non-negative power of $s_{11'3}$ to obtain a term in the expansion (5.47), we see that we must have

$$J_3 \; \geq \; J_1 + J_2 \tag{5.53}$$

We can repeat this last discussion for $M^{\mathcal{C}_b}$ by rewriting (5.51) as

$$\begin{aligned} & d^{J_1}_{0,n_1}(z_1)\, d^{J_2}_{0,n_2}(z_2)\, d^{J_3}_{-n_1-n_2,0}(z_3)\, u_1^{n_1} u_2^{n_2} \\ & \quad \sim \quad (z_1 z_3 u_1)^{(J_3 + J_1 - J_2)/2} (z_2 z_3 u_2^{-1})^{(J_3 + J_2 - J_1)/2} (z_1 z_2 u_1 u_2^{-1})^{(J_1 + J_2 - J_3)/2} u_1^{n_1 - J_1} u_2^{J_2 - n_2} \\ & \quad \sim \quad (s_{13})^{(J_3 + J_1 - J_2)/2} (s_{2'3'})^{(J_3 + J_2 - J_1)/2} (s_{123})^{(J_1 + J_2 - J_3)/2} \quad \times \; c_b(u_1, u_2) \end{aligned} \tag{5.54}$$

where we have used (5.8) for s_{123} ($\sim s_{12}$) instead of (5.5). Now the requirement of a non-negative power for s_{123} implies that terms in (5.49) can contribute only to those terms in (5.50) with

$$J_3 \; \leq \; J_1 \; + \; J_2 \tag{5.55}$$

Sinc the invariants in $M^{\mathcal{C}_c}$ have the same asymptotic form (apart from a sign) as those in $M^{\mathcal{C}_b}$ this last argument applies directly to $M^{\mathcal{C}_c}$. We see, therefore, that the asymptotic contributions of the triple discontinuities $M^{\mathcal{C}_b}$ and $M^{\mathcal{C}_c}$ ($M^{\mathcal{C}_{b'}}$ and $M^{\mathcal{C}_{c'}}$) appear in a distinct part of the partial-wave expansion (5.50) to that of $M^{\mathcal{C}_a}$. As a result, the Sommerfeld-Watson representation discussed in the next sub-section is very different in the two cases.

An additional requirement for (5.54) to correspond to a term in (5.47) is that the powers of the invariants in (5.54) must be integer. This places a further restriction on the partial-waves that $M^{\mathcal{C}_b}$ and $M^{\mathcal{C}_c}$ can contribute to. In fact, if we constrain $J_1+J_2-J_3$ to be an even integer, then no further constraint on the J_i is required (other than that they be positive integers). This is equivalent to the signature constraint

$$\tau_1\tau_2\tau_3 \ = \ 1 \tag{5.56}$$

where at this stage $\tau_i \ = \ \pm 1$ when J_i is *even/odd.* For this signature constraint on partial-wave amplitudes to be matched by the definition of signature via triple discontinuities that we give below, it must be that sum of the triple discontinuities $M^{\mathcal{C}_b}$ and $M^{\mathcal{C}_{b'}}$ is symmetric with respect to the two parts of the physical region where they appear. Similarly the sum of $M^{\mathcal{C}_c}$ and $M^{\mathcal{C}_{c'}}$ must be symmetric with respect to the two regions in which they appear.

Note that if we consider leading helicity physical amplitudes (i.e. with $|n_i| = J_i, \ i = 1, 2$) then if $n_1, n_2 > 0$, necessarily

$$J_3 \ \geq \ n_1 \ + \ n_2 \ = \ J_1 \ + \ J_2 \tag{5.57}$$

Consequently $J_3 < J_1 + J_2$ is only possible for (leading) helicity-flip amplitudes. It was observed by Detar and Weis[20], in their study many years ago of the dual-model triple-Regge vertex, that the terms in the vertex with (essentially) the sets of cuts $M^{\mathcal{C}_b}$ and $M^{\mathcal{C}_c}$ contribute to partial-wave amplitudes satisfying inequalities of the form (5.55). However, the S-W formalism that we use was not developed at the time of the Detar and Weis paper.

5.7 Signature and the Sommerfeld-Watson Representations

As in elementary Regge theory, it is necessary to introduce signature before making Froissart-Gribov (F-G) continuations of partial-wave amplitudes and introducing Sommerfeld-Watson (S-W) representations. We define signatured hexagraph amplitudes

$$
\begin{aligned}
M^{H,\underset{\sim}{\mathcal{T}}} &= M^{H,(\tau_1,\tau_2,\tau_3)} \\
&= \frac{1}{8}\Big[\, M^{H} \;+\; \tau_1 M^{\mathcal{T}_1 H} \;+\; \tau_2 M^{\mathcal{T}_2 H} \;+\; \tau_3 M^{\mathcal{T}_3 H} \;+\; \tau_1\tau_2 M^{\mathcal{T}_1\mathcal{T}_2 H} \\
&\qquad +\; \tau_2\tau_3 M^{\mathcal{T}_2\mathcal{T}_3 H} \;+\; \tau_3\tau_1 M^{\mathcal{T}_3\mathcal{T}_1 H} \;+\; \tau_1\tau_2\tau_3 M^{\mathcal{T}_1\mathcal{T}_2\mathcal{T}_3 H} \,\Big]
\end{aligned}
\tag{5.58}
$$

where $\tau_i = \pm 1$, and $\mathcal{T}_i H$ is the hexagaph obtained from the hexagraph H by a twist about the ith horizontal line. The full amplitude, or rather the sum over hexagraph amplitudes, is recovered as a sum over signatured amplitudes, i.e.

$$
\sum_{\underset{\sim}{\mathcal{T}}} M^{H,\,\underset{\sim}{\mathcal{T}}} = M^{H} + M^{\mathcal{T}_1 H} + M^{\mathcal{T}_2 H} + M^{\mathcal{T}_3 H} + M^{\mathcal{T}_1\mathcal{T}_2 H} + M^{\mathcal{T}_2\mathcal{T}_3 H} + M^{\mathcal{T}_3\mathcal{T}_1 H} + M^{\mathcal{T}_1\mathcal{T}_2\mathcal{T}_3 H}
\tag{5.59}
$$

For hexagraph amplitudes of the form $M^{\mathcal{C}_a}$ and $M^{\mathcal{C}_b}$, (5.58) is a simple generalisation of the analytic definition of signature for elastic scattering amplitudes, where combinations of amplitudes with right and left-hand cuts are formed. For $M^{\mathcal{C}_c}$ amplitudes it becomes the standard definition in the $s - s$ region.

In writing the initial dispersion relation (5.30) we are, of course, assuming a generalization of the usual crossing relation that there is a single analytic function that connects all the physical region amplitudes. When quark quantum numbers and helicities are involved, there are additional subtleties in the crossing relation. These subtleties are resolved if we assume that our analytic definition of signatured amplitudes in (5.58) is equivalent to the following alternative "group-theoretic" definition of signature. Beginning with an N-point amplitude in a particular s-channel, we form the positive (or negative) signatured amplitude, with respect to a particular internal line of a Toller diagram, by adding (or subtracting) the amplitude obtained by making a complete CPT transformation on all external particles connected (through the diagram) to one end of the internal line. The fully signatured amplitude is formed by carrying out this procedure for all internal lines of the Toller diagram. In this way, signature is introduced at the amplitude level without introducing spectral components. It is an operation defined directly on the external states and so is often easier to implement. Although the equivalence of the two definitions has only been proven in the simplest cases, we have no reason to doubt that the equivalence is true in general. To understand the implications of signature for phases etc. it is, of course, essential to utilise the analytic formulation.

In a t-channel the twisting process does not involve interchanging incoming and outgoing particles. Therefore, a signature twist becomes a CP rather than a CPT

transformation. The charge conjugation part of the transformation will eventually be very important for our discussion of the anomaly. However, if we ignore quantum numbers then a signature twist is effectively a t-channel parity transformation of the final state relative to the initial state. In order to have three independent parity transformations, we must have a dependence on invariants that involve directly the momenta at the central vertex, i.e. the Q_i. In Fig. 5.4, only $s_{11'3}$ has this property. This is why only triplets of the $\mathcal{C}_a$ kind produce three independent signatures.

The S-W transform of (5.50) is obtained by converting the sums over n_1, n_2, and J_3 to integrals. Initially this process is carried out with z_1 and z_2 small, although we will then use the representation to discuss large z_1 and z_2. The conversion of sums over n_1, n_2, to integrals effectively represents most of the asymptotic cuts as cuts in the u_1 and u_2 planes and therefore is most naturally carried out in the $s - s$ region where large u_1 and u_2 is part of the physical regions.

The treatment of that part of the expansion satisfying (5.53) is straightforward. This contains $M^{\mathcal{C}_a}$ together with the corresponding contribution from all the hexagraphs of Fig. 5.3. To illustrate the structure of the S-W transform we first omit the complications due to signature and (effectively) assume a F-G continuation can be made for $M^{\mathcal{C}_a}$ alone. Because the definition of $d^J_{n,0}$ changes non-analytically at $n = 0$ we must make separate continuations for $n_1, n_2, n_1 + n_2 \gtrless 0$. For $n_1, -n_2, n_1 + n_2 \geq 0$, we can write

$$\begin{aligned} M^{\mathcal{C}_a} = \; & \frac{1}{(2\pi)^3} \int_{>} \frac{dn_1 \; (u_1)^{n_1}}{\sin \pi n_1} \int_{<} \frac{dn_2 \; (u_2)^{n_2}}{\sin \pi n_2} \\ & \times \sum_{\substack{N_1 = J_1 - |n_1| = 0 \\ N_2 = J_2 - |n_2| = 0}}^{\infty} \int_{C_{N_1+N_2}} \frac{dJ_3 \;\; d^{J_3}_{n_1+n_2,0}(z_3)}{\sin \pi (J_3 - n_1 + n_2)} d^{J_1}_{0,n_1}(z_1) d^{J_2}_{0,n_2}(z_2) \;\; a_{\mathcal{C}_a, \underset{\sim}{J}, \underset{\sim}{n}, \underset{\sim}{>}} \end{aligned} \tag{5.60}$$

where each integration contour is asymptotically parallel to the imaginary axis and chosen to reproduce the partial-wave sum when closed in the appropriate half-plane (because of the symmetry under $u_1 \to u_1^{-1}, u_2 \to u_2^{-1}$, $n_1 \leq 0, n_2 \geq 0$ gives an identical contribution). The contour $C_{N_1+N_2}$ imposes (5.53) i.e.

$$J_1 + J_2 \;=\; N_1 + n_1 + N_2 - n_2 \leq J_3 \tag{5.61}$$

and so has the form shown in Fig. 5.5. The $>$ and $<$ labels for the n_i integrals indicate that they reproduce the associated positive/negative helicity sums.

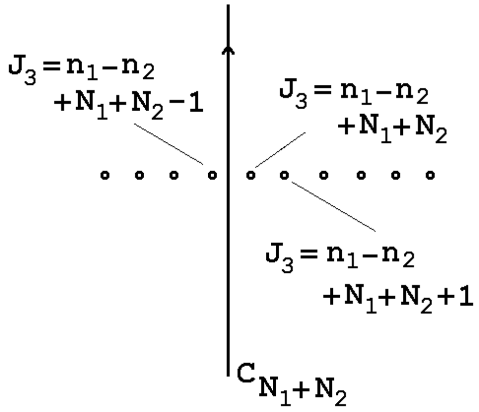

Fig. 5.5 The Contour in the J_3 Plane.

For small z_i, $i = 1, 2$, a twist in the ith channel corresponds to $u_i \to \; -u_i$ and $z_i \to \; -z_i$. For small z_i, and integer $j_i - |n_i| = N_i$,

$$d^{J_i}_{0,n_i}(-z_i) \; = \; (-1)^{J_i - n_i} d^{J_i}_{0,n_i}(z_i) \tag{5.62}$$

Consequently for $M^{\mathcal{C}_a}$ we can adapt (5.60) to represent the sum over amplitudes involving twists in the 1 and 2 channels by making the replacement

$$(u_i)^{n_i} d^{J_i}_{0,n_i}(z_i) \;\; \to \;\; (u_i)^{n_i} d^{J_1}_{0,n_i}(z_i) \; + \; \tau_i \, (-u_i)^{n_i} d^{J_i}_{0,n_i}(-z_i) \qquad i = 1, 2 \tag{5.63}$$

A twist in the 3 channel is more complicated since $d^{J_3}_{n_1+n_2,0}(z_3)$ depends on n_1 and n_2 as well as J_3. For amplitudes that already have specific τ_1 and τ_2 signatures, we can introduce signature for $z_3 \to -z_3$ by writing

$$d^{J_3}_{n_1+n_2,0}(z_3) \;\; \to \;\; d^{J_3}_{n_1+n_2,0}(z_3) \; + \;\; \tau_3 \tau_1 \tau_2 (-1)^{N_1+N_2} d^{J_3}_{n_1+n_2,0}(-z_3) \tag{5.64}$$

Of course, we also write

$$a_{\mathcal{C}_a, \underset{\sim}{J}, \underset{\sim}{n}, \underset{\sim}{>}} \;\; \to \;\; a_{\mathcal{C}_a, \underset{\sim}{J}, \underset{\sim}{n}, \underset{\sim}{>}, \underset{\sim}{\tau}} \tag{5.65}$$

The construction of signatured F-G continuations $a_{\mathcal{C}_a, \underset{\sim}{J}, \underset{\sim}{n}, \underset{\sim}{>}, \underset{\sim}{\tau}}$ that are equal to the physical partial-waves at "right-signature" points (i.e. J_i = even/odd for $\tau_i = +/-$, $i = 1, 2, 3$) is described in detail in [2].

The S-W transform of that part of the expansion (5.50) that satisfies (5.55), and so contains both $M^{\mathcal{C}_b}$ and $M^{\mathcal{C}_c}$, requires extra discussion. When (5.55) is satisfied at physical points, n_1 and n_2 will generally have opposite signs. (For leading helicities this must be the case, as we noted above.) Consider that part of (5.50) with $n_1, -n_2, n_1 + n_2 \geq 0$. (5.55) becomes

$$N_1 + n_1 + N_2 - n_2 - J_3 \; = \; \textit{even integer} \; \geq \; 0 \tag{5.66}$$

Temporarily ignoring the full signature problem, we can write

$$
\begin{aligned}
M^{\mathcal{C}_b} =& \frac{1}{(2\pi)^3} \int dn_1 dn_2 (u_1)^{n_1} (u_2)^{n_2} \sum_{\substack{N_1,N_2=0 \\ N_1+N_2 \ even}}^{\infty} d^{N_1+n_1}_{0,n_1}(z_1)\; d^{N_2-n_2}_{0,n_2}(z_2) \\
& \int_{C_{J_3}} \frac{dJ_3 \qquad\qquad d^{J_3}_{n_1+n_2,0}(z_3)}{\sin\pi(n_1+n_2)\sin\frac{\pi}{2}(J_3-n_1-n_2\sin\frac{\pi}{2}(n_1-n_2-J_3)} \quad a_{\mathcal{C}_b,\underset{\sim}{J},\underset{\sim}{n},\underset{\sim}{>}}
\end{aligned}
\tag{5.67}
$$

(The symmetry under $u_1 \to u_1^{-1}, u_2 \to u_2^{-1}$ implies that $n_1 \leq 0, n_2 \geq 0$ gives an identical contribution.) The integration contours are again asymptotically parallel to the imaginary axis and the contour C_{J_3} is as shown in Fig. 5.6.

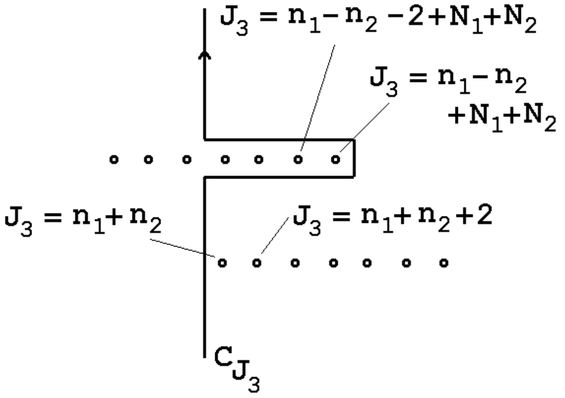

Fig. 5.6 The C_{J_3} Contour.

This contour now imposes (5.66). Poles at negative integer n_2 are produced when the poles at $J_3 - n_1 + n_2 - N_1 - N_2 =$ *even integer* < 0 collide with those at $J_3 - n_1 - n_2 =$ *even integer* ≥ 0 . As always the $\gtrless$ labels on $a_{\mathcal{C}_b,\underset{\sim}{J},\underset{\sim}{n},\underset{\sim}{>},\underset{\sim}{\mathcal{T}}}$ refer to distinct F-G continuations made for distinct combinations of helicity signs.

(5.67) gives both even and odd values of n_1 and n_2. Consequently (5.63) can again be used to introduce signature in the 1 and 2 channels. Since we must impose (5.56), we need not add any further signature effects. However, we note that the arguments of two of the denominator sine factors in (5.67) are already restricted to even integer physical values. Therefore, each term in the signatured form of (5.67) could be modified by a phase factor of the form $(-1)^E$ where E is (equivalently) either of these sine function arguments. In principle the uniquenes of the F-G continuation resolves this anbiguity. We will resolve it by determining the appropriate asymptotic phases of signatured Regge pole amplitudes. We will find that this phase provides the crucial distinction between the contribution of the physical region discontinuities of the $M^{\mathcal{C}_b}$ (and $M^{\mathcal{C}_{b'}}$) kind and the unphysical region discontinuities of the $M^{\mathcal{C}_c}$ (and $M^{\mathcal{C}_{c'}}$) kind.

5.8 Regge Behavior

The Steinmann relations imply that for the hexagraph amplitudes with physical region asymptotic cuts, these cuts are completely represented by signatured S-W integrals. Consequently, for $M^{\mathcal{C}_a}$ and $M^{\mathcal{C}_b}$ the sums over $N_1 = J_1 - n_1$ and $N_2 = J_2 - |n_2|$ should be uniformly convergent in the Regge asymptotic region with the limits and sums in the S-W representations liberally interchangeable. For the anomaly to appear in a physical region in the configuration of Fig. 4.15(a) then it has to be due a physical region singularity appearing in an amplitude that has cuts only in a cross-channel or unphysical region. As we elaborate further below, the anomaly can appear in this way in $M^{\mathcal{C}_c}$ (and $M^{\mathcal{C}_{c'}}$) amplitudes, where it has to produce a divergence of the N_1 and N_2 sums. A-priori, it would appear that the anomaly could also appear in the $M^{\mathcal{C}_b}$ (and $M^{\mathcal{C}_{b'}}$) amplitudes, since they are so similar to the $M^{\mathcal{C}_c}$ amplitudes. However, we will give arguments below that this is not the case.

For fixed N_1 and N_2, the integrals over n_1 and n_2 can be treated as integrals over either n_1 and n_2 or J_1 and J_2. Consequently asymptotic expansions can be obtained as either $z_1, z_2 \to \infty$ or as $u_1\ (u_1^{-1}), u_2\ (u_2^{-1}) \to \infty$ by pulling contours to the left (right) in the complex plane in the conventional manner. In this way, each of the triple-regge and helicity-pole limits defined above can be studied. The replacement of the $d^J_{n,0}$ by second-type representation functions proceeds in direct parallel with elementary regge theory. (This is a technical necessity to ensure that a genuine asymptotic expansion is obtained but we will not describe it here. For our purposes it is sufficient to assume that we simply pick up the leading power behavior of the $d^J_{n,0}(z)$ of the form z^J, as contours.)

The most important point for studying limits via the S-W transform is that (by analytically continuing t-channel unitarity equations in all complex angular momentum and helicity planes) it can be shown that the regge singularities of $a_{\mathcal{C},\underset{\sim}{J},\underset{\sim}{n},\underset{\sim}{>}} = a_{\mathcal{C},\underset{\sim}{>}}(J_3, n_1, n_2, N_1, N_2, t_1.t_2, t_3)$ occur at fixed values of the J_i. In particular, Regge poles at $J_i = \alpha_i = \alpha(t_i)$ occur in $a_{\mathcal{C},>,>}(J_3, n_1, n_2, N_1, N_2, t_1.t_2, t_3)$ (the F-G continuation made from $n_1, n_2 > 0$) at

$$n_1 = \alpha_1 - N_1\ , \quad n_2 = \alpha_2 - N_2\ , \quad J_3 = \alpha_3 \tag{5.68}$$

In $a_{\mathcal{C},>,<}(J_3, n_1, n_2, N_1, N_2, t_1.t_2, t_3)$ (the continuation from $n_1, -n_2 > 0$) the regge singularities occur at

$$n_1 = \alpha_1 - N_1\ , \quad -n_2 = \alpha_2 - N_2\ , \quad J_3 = \alpha_3 \tag{5.69}$$

etc. We will first study the contributions of regge poles to the S-W integral and then discuss the (minor) differences when the regge poles are replaced by regge cuts.

In the triple-regge limit, regge poles give contributions to each of the terms in the double sums in (5.60) and (5.67). We initially omit the denominator sine factors since they are modified by the introduction of signature. We can then write the triple regge pole contribution to $M^{\mathcal{C}_a}$ via (5.60) as

$$\begin{aligned} M^{\mathcal{C}_a} \underset{\substack{z_1,z_2,\\ z_3,\to\infty}}{\sim} \quad & z_1^{\alpha_1} z_2^{\alpha_2} z_3^{\alpha_3} \sum_{N_1,N_2=0}^{\infty} \Big[\; u_1^{\alpha_1-N_1} u_2^{\alpha_2-N_2} \beta^a_{\alpha_1,\alpha_2,\alpha_3,N_1,N_2} + \\ & u_1^{-\alpha_1+N_1} u_2^{\alpha_2-N_2} \beta^a_{-\alpha_1,\alpha_2,\alpha_3,N_1,N_2} \; + \; u_1^{\alpha_1-N_1} u_2^{-\alpha_2+N_2} \beta^a_{\alpha_1,-\alpha_2,\alpha_3,N_1,N_2} \\ & + u_1^{-\alpha_1+N_1} u_2^{-\alpha_2+N_2} \beta^a_{-\alpha_1,-\alpha_2,\alpha_3,N_1,N_2} \; \Big] \end{aligned} \tag{5.70}$$

where $\beta^a_{\alpha_1,\alpha_2,\alpha_3,N_1,N_2}$ is the Regge-pole residue of the "non-flip" F-G amplitude $a_{\mathcal{C},>,>}(J_3,n_1,n_2,N_1,N_2,t_1.t_2,t_3)$ at $J_i = \alpha_i, \ i = 1,2,3$ and $n_i = J_i - N_i, \ i = 1,2$ and $\beta^a_{-\alpha_1,\alpha_2,\alpha_3,N_1,N_2}$ is the corresponding residue of the "helicity-flip" F-G amplitude $a_{\mathcal{C},<,>}(J_3,n_1,n_2,N_1,N_2,t_1.t_2,t_3)$. Because of the symmetry under $u_1 \to 1/u_1, u_2 \to 1/u_2$, the first and last sums in (5.70) can be identified, as can the second and third. When the hexagraph containing $M^{\mathcal{C}_a}$ is part of a larger hexagraph this symmetry is, in general, not present.

The contribution of Regge poles to $M^{\mathcal{C}_b}$ (and $M^{\mathcal{C}_b}$), in the triple-Regge limit, has less structure than (5.70). From (5.67) we obtain

$$\begin{aligned} M^{\mathcal{C}_b} \underset{\substack{z_1,z_2,\\ z_3,\to\infty}}{\sim} \quad & z_1^{\alpha_1} z_2^{\alpha_2} z_3^{\alpha_3} \sum_{N_1+N_2 even} \Big[u_1^{-\alpha_1+N_1} u_2^{\alpha_2-N_2} \beta^b_{-\alpha_1,\alpha_2,\alpha_3,N_1,N_2} \\ & \qquad + \; u_1^{\alpha_1-N_1} u_2^{-\alpha_2+N_2} \beta^a_{\alpha_1,-\alpha_2,\alpha_3,N_1,N_2} \Big] \end{aligned} \tag{5.71}$$

Again the symmetry under $u_1 \to 1/u_1, u_2 \to 1/u_2$ implies that (in this case) the two terms in (5.71) can be identified. $M^{\mathcal{C}_c}$ has an identical contribution but with, of course, $\beta^b_{\pm\alpha_1,\pm\alpha_2,\alpha_3,N_1,N_2} \;\to\; \beta^c_{\pm\alpha_1,\pm\alpha_2,\alpha_3,N_1,N_2}$.

To obtain the behavior of the full amplitude in the triple-regge limit we add $M^{\mathcal{C}_a}$, $M^{\mathcal{C}_b}$ and $M^{\mathcal{C}_c}$ $M^{\mathcal{C}_{b'}}$ and $M^{\mathcal{C}_{c'}}$, together with the analagous contributions corresponding to the additional hexagraphs illustrated in Fig. 5.2. These contributions will have the same form as (5.70) and (5.71) but with the indices $1,2$ and 3 cyclically rotated. Finally, the twisted graphs also have to be added by incorporating signature factors. Before discussing signature in detail, it will be useful to first discuss the contribution of regge poles in helicity-pole limits.

The non-flip helicity-pole limit (5.14) picks out only the first term of the first (and identical third) sum in (5.70) i.e.

$$M^{\mathcal{C}_a} \underset{\substack{u_1, u_2, \\ z_3, \to \infty}}{\sim} (z_1u_1)^{\alpha_1} \, (z_2u_2)^{\alpha_2} \, z_3^{\alpha_3} \, \beta^a_{\alpha_1,\alpha_2,\alpha_3,0,0} \tag{5.72}$$

There is no triple-regge contribution from $M^{\mathcal{C}_b}$ or $M^{\mathcal{C}_c}$ in this limit. In the helicity-flip limit each of $M^{\mathcal{C}_a}$, $M^{\mathcal{C}_b}$, and $M^{\mathcal{C}_c}$ give contributions, i.e.

$$M^{\mathcal{C}_{a,b,c}} \underset{\substack{u_1, 1/u_2, \\ z_3, \to \infty}}{\sim} (z_1u_1)^{\alpha_1} \, (z_2u_2^{-1})^{\alpha_2} z_1^{\alpha_3} \beta^{a,b,c}_{\alpha_1,-\alpha_2,\alpha_3,0,0} \tag{5.73}$$

We see that distinct leading helicity amplitudes, i.e. non-flip and flip, contribute in the distinct helicity-pole limits while the complete series of both amplitudes contribute in the full triple-regge limit. This explains why we refer to (5.14) and (5.15) respectively as non-flip and helicity-flip limits. Note that in both limits the dependence on both z_1 and z_2 is determined by the u_1 and u_2 dependence. This is necessary for the amplitudes to be directly expressible in terms of invariants, as we see in the next sub-section.

5.9 Asymptotic Analytic Structure

We can now discuss how the cuts of $M^{\mathcal{C}_a}$, $M^{\mathcal{C}_b}$, and $M^{\mathcal{C}_c}$ are represented asymptotically in triple-regge formulae. Again we discuss regge poles in detail. We will then illustrate how the discussion generalises to regge cuts. Similarly to the rewriting of (5.51) in the form (5.52), we can use (5.3) - (5.7) to write

$$\begin{aligned} \beta^a_{\alpha_1,\alpha_2,\alpha_3,0,0} \, (z_1u_1)^{\alpha_1}(z_2u_2)^{\alpha_2} z_3^{\alpha_3} &= \beta^a_{\alpha_1,\alpha_2,\alpha_3,0,0} \, (z_1z_3u_1)^{\alpha_1}(z_1z_3u_2)^{\alpha_2} \, (z_3)^{\alpha_3-\alpha_1-\alpha_2} \\ &\sim \beta^a_{\alpha_1,\alpha_2,\alpha_3,0,0} \, (s_{13})^{\alpha_1}(s_{2'3'})^{\alpha_2}(s_{11'3})^{\alpha_3-\alpha_1-\alpha_2} \end{aligned} \tag{5.74}$$

showing how (5.72) represents the cuts of $M^{\mathcal{C}_a}$ in both the non-flip helicity-pole limit and the full triple-Regge limit. The non-leading helicity terms in (5.70) that contribute in the triple-regge limit are represented in terms of invariants by writing

$$u_1^{-N_1} \; u_2^{-N_2} \;\sim\; \left(\frac{s_{133'} \;\, s_{311'}}{s_{13}}\right)^{N_1} \left(\frac{s_{2'33'} \;\, s_{3'22'}}{s_{23}}\right)^{N_2} \tag{5.75}$$

The result is a power series expansion in terms of the invariants $s_{133'}, s_{311'}, s_{2'33'}, s_{3'22'}$ in which the Steinmann relations determine there are no singularities. Therefore this series is convergent and the cut structure is fully represented by (5.74). Similarly to (5.74) we can write

$$\begin{aligned}\beta^a_{\alpha_1,-\alpha_2,\alpha_3,0,0}\ (z_1u_1)^{\alpha_1}(z_2u_2^{-1})^{\alpha_2}z_3^{\alpha_3} &= \beta^a_{\alpha_1,-\alpha_2,\alpha_3,0,0}\ (z_1z_3u_1)^{\alpha_1}\left(\frac{z_2z_3}{u_2}\right)^{\alpha_2}(z_3)^{(\alpha_3-\alpha_1-\alpha_2)}\\ &\sim \beta^a_{\alpha_1,-\alpha_2,\alpha_3,0,0}\ (s_{13})^{\alpha_1}(s_{2'3'})^{\alpha_2}(s_{11'3})^{\alpha_3-\alpha_1-\alpha_2}\end{aligned} \tag{5.76}$$

to see the cuts of $M^{\mathcal{C}_a}$ also represented in the helicity-flip limit and in helicity-flip contributions to the triple-Regge limit.

For the helicity-flip contribution from $M^{\mathcal{C}_b}$ we utilise (5.8) and write

$$\begin{aligned}&\beta^b_{\alpha_1,-\alpha_2,\alpha_3,0,0}\ (z_1u_1)^{\alpha_1}(z_2u_2^{-1})^{\alpha_2}z_3^{\alpha_3}\\ &\quad= \beta^b_{\alpha_1,-\alpha_2,\alpha_3,0,0}\ (z_1z_3u_1)^{(\alpha_1+\alpha_3-\alpha_2)/2}\left(\frac{z_2z_3}{u_2}\right)^{(\alpha_2+\alpha_3-\alpha_1)/2}\left(\frac{z_1z_2u_1}{u_2}\right)^{(\alpha_1+\alpha_2-\alpha_3)/2}\\ &\quad\sim\ \beta^b_{\alpha_1,-\alpha_2,\alpha_3,0,0}\ (s_{13})^{(\alpha_1+\alpha_3-\alpha_2)/2}(s_{2'3'})^{(\alpha_2+\alpha_3-\alpha_1)/2}(s_{123})^{(\alpha_1+\alpha_2-\alpha_3)/2}\end{aligned} \tag{5.77}$$

showing how the cuts of $M^{\mathcal{C}_b}$ are represented in the helicity-flip limit and in helicity-flip contributions to the triple-Regge limit. For $M^{\mathcal{C}_c}$ we write, in close analogy,

$$\begin{aligned}&\beta^c_{\alpha_1,-\alpha_2,\alpha_3,0,0}\ (z_1u_1)^{\alpha_1}(z_2u_2^{-1})^{\alpha_2}z_3^{\alpha_3}\\ &\quad\sim\ \beta^c_{\alpha_1,-\alpha_2,\alpha_3,0,0}\ (s_{13})^{(\alpha_1+\alpha_3-\alpha_2)/2}(s_{2'3'})^{(\alpha_2+\alpha_3-\alpha_1)/2}(s_{1'2})^{(\alpha_1+\alpha_2-\alpha_3)/2}\end{aligned} \tag{5.78}$$

To add signature factors to (5.74) note that for $J_i - |n_i| = N_i = 0$

$$\frac{(u_i)^{n_i}d^{J_1}_{0,n_i}(z_i)\ +\ \tau_i\ (-u_i)^{n_i}d^{J_i}_{0,n_i}(-z_i)}{sin\pi n_i}\ \underset{u_i,\, z_i\,\to\,\infty}{\sim}\ |u_iz_i|^{J_i}\left[\frac{1+\tau_ie^{i\pi J_i}}{sin\pi J_i}\right] \tag{5.79}$$

and

$$\frac{d^{J_3}_{n_1+n_2,0}(z_3)+\tau_3\tau_1\tau_2d^{J_3}_{n_1+n_2,0}(-z_3)}{sin\pi(J_3-J_1-J_2)}\ \underset{z_3\,\to\,\infty}{\longrightarrow}\ |z_3|^{J_3}\left[\frac{1+\tau_1\tau_2\tau_3e^{i\pi(J_3-J_1-J_2)}}{sin\pi(J_3-J_1-J_2)}\right] \tag{5.80}$$

Therefore the signatured form of the S-W representation (5.67) will give (5.74) multiplied by a factor

$$\left[\frac{1+\tau_1e^{i\pi\alpha_1}}{sin\pi\alpha_1}\right]\left[\frac{1+\tau_2e^{i\pi\alpha_2}}{sin\pi\alpha_2}\right]\left[\frac{1+\tau_1\tau_2\tau_3e^{i\pi(\alpha_3-\alpha_1-\alpha_2)}}{sin\pi(\alpha_3-\alpha_1-\alpha_2)}\right] \tag{5.81}$$

giving

$$\beta^a_{\alpha_1,\alpha_2,\alpha_3,0,0}\left[\frac{(s_{13})^{\alpha_1}+\tau_1(-s_{13})^{\alpha_1}}{sin\pi\alpha_1}\right]\left[\frac{(s_{2'3'})^{\alpha_2}+\tau_2(-s_{2'3'})^{\alpha_2}}{sin\pi\alpha_2}\right] \times \left[\frac{(s_{11'3})^{\alpha_3-\alpha_1-\alpha_2}+\tau_1\tau_2\tau_3(-s_{11'3})^{\alpha_3-\alpha_1-\alpha_2}}{sin\pi(\alpha_3-\alpha_1-\alpha_2)}\right] \tag{5.82}$$

This expression now represents the leading helicity (non-flip) triple-regge contribution of the sum of amplitudes corresponding to the eight hexagraphs appearing in Fig. 5.3.

Each hexagraph can be identified with a term in (5.82), with the phase appropriately representing the cut structure. It is therefore straightforward to take discontinuities in (5.82) and to recover a single hexagraph amplitude (5.74), e.g.

$$[Disc]_{s_{13}} = 2\,\beta^a_{\alpha_1,\alpha_2,\alpha_3,0,0}\,(s_{13})^{\alpha_1}\left[\frac{(s_{2'3'})^{\alpha_2}+\tau_2(-s_{2'3'})^{\alpha_2}}{sin\pi\alpha_2}\right] \times \left[\frac{(s_{11'3})^{\alpha_3-\alpha_1-\alpha_2}+\tau_1\tau_2\tau_3(-s_{11'3})^{\alpha_3-\alpha_1-\alpha_2}}{sin\pi(\alpha_3-\alpha_1-\alpha_2)}\right] \tag{5.83}$$

$$[Disc]_{s_{13}}\,[Disc]_{s_{2'3'}} = 4\,\beta^a_{\alpha_1,\alpha_2,\alpha_3,0,0}\,(s_{13})^{\alpha_1}(s_{2'3'})^{\alpha_2} \times \left[\frac{(s_{11'3})^{\alpha_3-\alpha_1-\alpha_2}+\tau_1\tau_2\tau_3(-s_{11'3})^{\alpha_3-\alpha_1-\alpha_2}}{sin\pi(\alpha_3-\alpha_1-\alpha_2)}\right] \tag{5.84}$$

$$[Disc]_{s_{13}}\,[Disc]_{s_{2'3'}}[Disc]_{s_{11'3}} = 8\,\beta^a_{\alpha_1,\alpha_2,\alpha_3,0,0}\,(s_{13})^{\alpha_1}(s_{2'3'})^{\alpha_2}(s_{11'3})^{\alpha_3-\alpha_1-\alpha_2} \tag{5.85}$$

Note that for a reggeized gluon with $\alpha_i = 1 + O(g^2)$

$$sin\pi\alpha_2 \sim sin\pi(\alpha_3-\alpha_1-\alpha_2) \sim O(g^2) \tag{5.86}$$

and since $\tau_i = -1\ \forall\ i$, each discontinuity reduces the amplitude by $O(g^2)$. With two reggeon states in each channel $\tau_i = -1\ \forall\ i$. In this case the leading terms in each of the square brackets in (5.81) cancel and taking discontinuities does not introduce extra powers of g^2.

Moving on to the contributions to $M^{\mathcal{C}_b}$ obtained from the signatured form of (5.67). As we noted earlier, for the signature constraint (5.56) to also emerge from the hexagraph definition of signature, then it has to be that the sum of the amplitudes $M^{\mathcal{C}_b}$ and $M^{\mathcal{C}_{b'}}$ is equal in the two physical regions in which they appear, as must also be the amplitudes $M^{\mathcal{C}_c}$ and $M^{\mathcal{C}_{c'}}$. As we emphasized, the regge amplitudes we discuss can not distinguish the contribution of asymptotically equivalent cuts. In the following, therefore, we identify $M^{\mathcal{C}_b}$ with the sum of $M^{\mathcal{C}_b}$ and $M^{\mathcal{C}_{b'}}$.

Since we only have two signature factors to add, (5.81) is replaced by

$$\frac{[1+\tau_1 e^{i\pi\alpha_1}+\tau_2 e^{i\pi\alpha_2}+\tau_1\tau_2 e^{i\pi(\alpha_1+\alpha_2)}]}{[sin\pi(\alpha_1-\alpha_2)sin\frac{\pi}{2}(\alpha_2+\alpha_3-\alpha_1)sin\frac{\pi}{2}(\alpha_1+\alpha_2-\alpha_3)]} \tag{5.87}$$

After adding the term corresponding to (5.67) from $n_1+n_2<0$, we obtain the factor

$$\frac{[1+\tau_1 e^{i\pi\alpha_1}+\tau_2 e^{i\pi\alpha_2}+\tau_1\tau_2 e^{i\pi(\alpha_1+\alpha_2)}]}{[sin\frac{\pi}{2}(\alpha_1+\alpha_3-\alpha_2)sin\frac{\pi}{2}(\alpha_2+\alpha_3-\alpha_1)sin\frac{\pi}{2}(\alpha_1+\alpha_2-\alpha_3)]} \tag{5.88}$$

The interpretation of the phases in terms of cut structure is now more subtle. The τ_1 twist of the hexagraph containing $M^{\mathcal{C}_b}$ sends $s_{123}\to -s_{123}$ in addition to $s_{13}\to -s_{13}$. The corresponding triple-regge behavior should therefore be

$$\begin{aligned}(-s_{13})^{(\alpha_1+\alpha_3-\alpha_2)/2}&(s_{2'3'})^{(\alpha_2+\alpha_3-\alpha_1)/2}(-s_{123})^{(\alpha_1+\alpha_2-\alpha_3)/2}\\ &= e^{i\pi\alpha_1}(s_{13})^{(\alpha_1+\alpha_3-\alpha_2)/2}(s_{2'3'})^{(\alpha_2+\alpha_3-\alpha_1)/2}(s_{123})^{(\alpha_1+\alpha_2-\alpha_3)/2}\end{aligned} \tag{5.89}$$

which is the phase-factor corresponding to the τ_1 term in (5.88). This phase is due to the contribution of two cuts rather than the conventional single cut, as was the case for $M^{\mathcal{C}_a}$. The τ_2 twist gives the analagous result and explains the τ_2 term in (5.88). Because of the signature constraint (5.56) we have $\tau_1\tau_2\equiv\tau_3$. We can obtain the corresponding phase for the $\tau_1\tau_2$ term if we multiply by $e^{i\pi(\alpha_3-\alpha_1-\alpha_2)}$. The presence or absence of a phase of this kind is the ambiguity in (5.67) that we discussed at the end of sub-section 5.5. Invoking this phase, we can write the analogue of (5.82) as

$$\begin{aligned}\beta^b_{\alpha_1,-\alpha_2,\alpha_3,0,0}\Big[\,&(s_{13})^{(\alpha_1+\alpha_3-\alpha_2)/2}(s_{2'3'})^{(\alpha_2+\alpha_3-\alpha_1)/2}(s_{123})^{(\alpha_1+\alpha_2-\alpha_3)/2}\\ &+\ \tau_1(-s_{13})^{(\alpha_1+\alpha_3-\alpha_2)/2}(s_{2'3'})^{(\alpha_2+\alpha_3-\alpha_1)/2}(-s_{123})^{(\alpha_1+\alpha_2-\alpha_3)/2}\\ &\quad+\ \tau_2(s_{13})^{(\alpha_1+\alpha_3-\alpha_2)/2}(-s_{2'3'})^{(\alpha_2+\alpha_3-\alpha_1)/2}(-s_{123})^{(\alpha_1+\alpha_2-\alpha_3)/2}\\ &\qquad+\ \tau_3(-s_{13})^{(\alpha_1+\alpha_3-\alpha_2)/2}(-s_{2'3'})^{(\alpha_2+\alpha_3-\alpha_1)/2}(s_{123})^{(\alpha_1+\alpha_2-\alpha_3)/2}\,\Big]\\ &\qquad\Big/\ [sin\frac{\pi}{2}(\alpha_1+\alpha_3-\alpha_2)sin\frac{\pi}{2}(\alpha_2+\alpha_3-\alpha_1)sin\frac{\pi}{2}(\alpha_1+\alpha_2-\alpha_3)]\end{aligned} \tag{5.90}$$

which is now the sum of the leading helicity-flip triple-regge contributions of cuts of the form of $M^{\mathcal{C}_b}$ in the hexagraphs of Fig. 5.3. (Note that we can assign the τ_i factors in many different ways using the relations $\tau_1\tau_2\tau_3=1$ and $\tau_i^2=1,\ i=1,2,3$). If we assume that $\beta^b_{\alpha_1,-\alpha_2,\alpha_3,0,0}$ is real then the phases of the four terms in (5.90) naturally represent the four possible cut structures. There are only four terms because of the equalities leading to the signature constraint.

Taking discontinuities in (5.90) (bearing in mind asymptotic equivalence)

$$[Disc]_{s_{13}}\ [Disc]_{s_{2'3'}} \;=\; 2\ \beta^{b}_{\alpha_1,-\alpha_2,\alpha_3,0,0}\ (s_{13})^{(\alpha_1+\alpha_3-\alpha_2)/2}(s_{2'3'})^{(\alpha_2+\alpha_3-\alpha_1)/2} \times\ \frac{(s_{123})^{(\alpha_1+\alpha_2-\alpha_3)/2}}{sin\frac{\pi}{2}(\alpha_1+\alpha_1-\alpha_3)} \tag{5.91}$$

and the triple discontinuity is

$$[Disc]_{s_{13}}\ [Disc]_{s_{2'3'}}[Disc]_{s_{123}} \;=\; 8\ \beta^{b}_{\alpha_1,-\alpha_2,\alpha_3,0,0}\ (s_{13})^{(\alpha_1+\alpha_3-\alpha_2)/2}(s_{2'3'})^{(\alpha_2+\alpha_3-\alpha_1)/2} \times\ (s_{123})^{(\alpha_1+\alpha_2-\alpha_3)/2} \tag{5.92}$$

Note that because

$$sin\frac{\pi}{2}(\alpha_i+\alpha_j-\alpha_k) \;=\; sin\frac{\pi}{2}(1+O(g^2)) \;=\; 1+O(g^4) \tag{5.93}$$

taking discontinuities, in lowest-order, simply introduces factors of 2 as in (2.3). This simplicity holds for the leading helicity amplitude and (because the azimuthal angle sums are convergent) also for the full triple-regge amplitude. Using (2.2) we see that in lowest-order each of the amplitudes in (5.90) is pure imaginary.

Finally we come to the unphysical triplets of the form $M^{\mathcal{C}_c}$. The regge behavior obtained from $M^{\mathcal{C}_c}$ has to have essentially the same form as that obtained from $M^{\mathcal{C}_b}$. However, with the appropriate choice of the phase ambiguity in (5.67) we can obtain, instead of (5.90), the triple-regge amplitude

$$\begin{aligned}\beta^{c}_{\alpha_1,-\alpha_2,\alpha_3,0,0}\Big[\ & (s_{13})^{(\alpha_1+\alpha_3-\alpha_2)/2}(s_{2'3'})^{(\alpha_2+\alpha_3-\alpha_1)/2}(-s_{12})^{(\alpha_1+\alpha_2-\alpha_3)/2} \\ &+\ \tau_1(-s_{13})^{(\alpha_1+\alpha_3-\alpha_2)/2}(s_{2'3'})^{(\alpha_2+\alpha_3-\alpha_1)/2}(s_{12})^{(\alpha_1+\alpha_2-\alpha_3)/2} \\ &+\ \tau_2(s_{13})^{(\alpha_1+\alpha_3-\alpha_2)/2}(-s_{2'3'})^{(\alpha_2+\alpha_3-\alpha_1)/2}(s_{12})^{(\alpha_1+\alpha_2-\alpha_3)/2} \\ &+\ \tau_3(-s_{13})^{(\alpha_1+\alpha_3-\alpha_2)/2}(-s_{2'3'})^{(\alpha_2+\alpha_3-\alpha_1)/2}(-s_{12})^{(\alpha_1+\alpha_2-\alpha_3)/2}\ \Big] \\ &\Big/\ [sin\frac{\pi}{2}(\alpha_1+\alpha_3-\alpha_2)sin\frac{\pi}{2}(\alpha_2+\alpha_3-\alpha_1)sin\frac{\pi}{2}(\alpha_1+\alpha_2-\alpha_3)]\end{aligned} \tag{5.94}$$

Again we have only four terms because of the signature constraint.

Note that both (5.90) and (5.94) are symmetric with respect to α_1, α_2 and α_3 and that more generally the breaking of cyclic symmetry by our choice of hexagraphs has been restored. Full expansions of the form of (5.71) still reflect the hexagraphs used in their derivation. However, this is no more than a choice of variables to expand in. Also, neither (5.90) nor (5.94) has any t-channel poles when any of the α_i pass through integer values. Indeed, any relationship between analytic structure and the hexagraph formalism used has essentially been lost. The asymptotic structure of the $M^{\mathcal{C}_b}$ and $M^{\mathcal{C}_c}$ amplitudes has no preference for the t-channel in which the partial-wave analysis is carried out. Ultimately this goes back to the constraint (5.55) which, in fact, is satisfied symetrically. Note, however, that the denominator in both (5.90) and (5.94) does appear to produce unphysical poles in the α_i. The $M^{\mathcal{C}_b}$ and $M^{\mathcal{C}_c}$ amplitudes have to combine to cancel these poles. This is a consistency condition which clearly requires the presence of the unphysical triple discontinuities in the dispersion relation.

5.10 Regge Cuts

(5.82) and (5.90) contain the contribution of Regge poles only. To replace a Regge pole by the Regge cut corresponding to a two-reggeon state is straightforward in principle but in practise can be quite complicated. However, for odd-signature reggeized gluons with $\alpha \sim 1$ it is relatively simple to describe the first-order approximation. For example, replacing the Regge pole in the 1 channel in (5.82) by an even signature two-reggeon state gives,

$$\begin{aligned}
\left[\frac{(s_{13})^{\alpha_1}+(-s_{13})^{\alpha_1}}{sin\pi\alpha_1}\right] \;\longrightarrow\; & \int \frac{d^2k}{sin\pi\alpha(k^2)sin\pi\alpha((Q_1-k)^2)} \\
& \times \left[\frac{(s_{13})^{(\alpha(k^2)+\alpha(Q_1-k)^2-1)}+(-s_{13})^{(\alpha(k^2)+\alpha(Q_1-k)^2-1)}}{sin\pi(\alpha(k^2)+\alpha(Q_1-k)^2-1)}\right] \\
\sim \;& \int \frac{d^2k}{(k^2)(Q_1-k)^2}\;\; [\; s_{13}\;] \left[1+O(g^2)\right] \\
\sim \;& J_1(Q_1^2)\;\; [\; s_{13}\;] \left[1+O(g^2)\right]
\end{aligned} \tag{5.95}$$

Similarly

$$\begin{aligned}
[Disc]_{s_{13}} \;\longrightarrow\; & \int \frac{d^2k}{sin\pi\alpha(k^2)sin\pi\alpha((Q_1-k)^2)}(s_{13})^{(\alpha(k^2)+\alpha(Q_1-k)^2-1)} \\
\sim \;& J_1(Q_1^2)\;\; [\; s_{13}\;] \left[1+O(g^2)\right]
\end{aligned} \tag{5.96}$$

Analagous changes occur if we replace any of the other Regge pole contributions in the foregoing by Regge cuts. The isolated power behavior corresponding to a regge pole is replace by a continuum integral of the power behavior involved together with a corresponding replacement of signature factors. Apart from this, all the above discussion of hexagraph contributions, analytic structure of triple-regge, helicity-flip, and helicity non-flip, amplitudes goes through in complete parallel for amplitudes containing general multi-reggeon states in each t-channel.

To give another specific example that is directly relevant for our discussion of anomaly amplitudes, we consider the first term in (5.94). If each of the regge poles is replaced by a two-reggeon state we obtain

$$
\begin{aligned}
&\prod_i \int \frac{d^2k_i}{sin\pi\alpha(k_i^2)sin\pi\alpha((Q_i-k_i)^2)} \\
&\beta^c_{[\alpha(k_1^2)+\alpha((Q_1-k_1)^2)-1],-[\alpha(k_2^2)+\alpha((Q_2-k_2)^2)-1],[\alpha(k_3^2)+\alpha((Q_3-k_3)^2)-1],0,0}(k_1,k_2,k_3,Q_1,Q_2,Q_3) \\
&\Big[\ (s_{13})^{[\alpha(k_1^2)+\alpha((Q_1-k_1)^2)+\alpha(k_3^2)+\alpha((Q_3-k_3)^2)-\alpha(k_2^2)-\alpha((Q_2-k_2)^2)-1]/2} \\
&\qquad (s_{2'3'})^{[\alpha(k_3^2)+\alpha((Q_3-k_3)^2)+\alpha(k_2^2)+\alpha((Q_2-k_2)^2)-\alpha(k_1^2)-\alpha((Q_1-k_1)^2)-1]/2} \\
&\qquad\quad (-s_{12})^{[\alpha(k_1^2)+\alpha((Q_1-k_1)^2)+\alpha(k_2^2)+\alpha((Q_2-k_2)^2)-\alpha(k_3^2)-\alpha((Q_3-k_3)^2)-1]/2}\Big] \Big/ \\
&\Big[[sin\frac{\pi}{2}[\alpha(k_1^2)+\alpha((Q_1-k_1)^2)+\alpha(k_3^2)+\alpha((Q_3-k_3)^2)-\alpha(k_2^2)+\alpha((Q_2-k_2)^2)] \\
&\quad sin\frac{\pi}{2}[\alpha(k_3^2)+\alpha((Q_3-k_3)^2)+\alpha(k_2^2)+\alpha((Q_2-k_2)^2)-\alpha(k_1^2)+\alpha((Q_1-k_1)^2)] \\
&\quad sin\frac{\pi}{2}[\alpha(k_1^2)+\alpha((Q_1-k_1)^2)+\alpha(k_2^2)+\alpha((Q_2-k_2)^2)-\alpha(k_3^2)+\alpha((Q_3-k_3)^2)]\Big] \\
&\underset{g^2\to 0}{\sim}\quad (s_{13})^{1/2}(s_{2'3'})^{1/2}(s_{1'2})^{1/2}\prod_i \int \frac{d^2k_i}{k_i^2(Q_i-k_i)^2}\ \beta^c_{1,-1,1,0,0}(k_1,k_2,k_3,Q_1,Q_2,Q_3)
\end{aligned}
\tag{5.97}
$$

The last line can be identified directly with the general reggeon diagram amplitude (2.1) so that $\beta^c_{1,-1,1,0,0}(k_1,k_2,k_3,Q_1,Q_2,Q_3)$ is identified with the reggeon vertex $R(k_1,k_2,k_3,Q_1,Q_2,Q_3)$. More specifically, the last line of (5.97) can also be identified with reggeon diagram amplitudes such as (4.15) discussed in the last Section. From (5.96) and (5.97) it is clear that the simple leading order properties of discontinuities that follows from (5.93) hold for regge cut as well as regge pole amplitudes.

In general, as we have already emphasized, we expect amplitudes containing regge cuts (i.e. multi-reggeon states) in any channel to have the non-planarity properties necessary to produce simultaneous right and left hand cuts in integrated invariants. This will lead to closely related right and left hand cuts in external invariants. Comparing (5.90) and (5.94) we see that for fixed s_{13} and $s_{2'3'}$ the two contributions provide right and left-hand cuts in the $s_{1'2} \sim z_1 z_2$ plane. We anticipate, and in the next Section will find, that amplitudes containing regge cuts in each channel will have closely related cuts of this kind and so if they contribute to $M^{\mathcal{C}_b}$ they will typically contribute also to $M^{\mathcal{C}_c}$. Indeed, in many respects the $M^{\mathcal{C}_c}$ amplitudes provide the additional four amplitudes that would need to be added to the $M^{\mathcal{C}_b}$ amplitudes to obtain a complete set of signatured amplitudes with no signature constraint. However, the analytic relationship between the the asymptotic cuts and the angular invariants in which signature properties are necessarily determined prevents such a relationship. Also we will see that the anomaly can consistently appear in the $M^{\mathcal{C}_c}$ amplitudes but not the $M^{\mathcal{C}_b}$ amplitudes.

5.11 Dimensions of Reggeon Interactions

Next we note a crucial difference between (5.76) and (5.77) that is vital for the appearance of the triangle anomaly. First we set

$$\alpha_1 \ = \ \alpha_2 \ = \ \alpha_3 \ = \ 1 \tag{5.98}$$

corresponding to the contribution of (multi-)gluon reggeon states. We then compare the momentum dimension of (5.76) and (5.77). For (5.76) we obtain

$$(s_{13})^{\alpha_1}(s_{2'3'})^{\alpha_2}(s_{11'3})^{\alpha_3-\alpha_1-\alpha_2} \ \equiv \ [s]^{1+1-1} \ = \ [s] \tag{5.99}$$

while for (5.77) we obtain

$$(s_{31})^{(\alpha_1+\alpha_3-\alpha_2)/2}(s_{23})^{(\alpha_2+\alpha_3-\alpha_1)/2}(s_{12})^{(\alpha_1+\alpha_2-\alpha_3)/2} \ \equiv \ [s]^{\frac{1}{2}+\frac{1}{2}+\frac{1}{2}} \ = \ [s]^{\frac{3}{2}} \tag{5.100}$$

Since the contribution of any multi-reggeon state always carries the same transverse dimension dimension

$$\int \frac{d^2k_1d^2k_2 \ \cdots \delta^2(Q-k_1-k_2-\cdots)}{k_1^2k_2^2 \ \cdots} \ \equiv \ [Q]^{-2} \tag{5.101}$$

the difference in dimensions of (5.99) and (5.100) has to be compensated by a difference in the transverse momentum dimension of the accompanying reggeon vertex. If we anticipate that (as is the case) the dimension of the vertex accompanying (5.99) is the normal $[Q]^2$ for a reggeon vertex in QCD, then the vertex accompanying (5.100) will have the "anomalous dimension" of $[Q]$. This anomalous dimension allows the reggeon interaction vertices generated by $M^{\mathcal{C}_b}$ or $M^{\mathcal{C}_c}$ to potentially contain the anomaly of the four-dimensional triangle diagram - which is linear in it's momentum dimension and is independent of any other scale.

5.12 Multi-Regge Amplitudes and the Anomaly

Note that the amplitude for the process given by Fig. 4.15(a), that contains the anomaly, has no initial (s_{13}) or final ($s_{2'3'}$) state discontinuities. If we suppose that external G_i couplings can be chosen such that the anomaly in an amplitude of this kind does not cancel then the amplitude must be reproduced by a triple-regge amplitude with the anomaly in the six-reggeon vertex. In QCD we will find that a quantum number (color parity) prevents the anomaly from appearing in the triple-regge amplitude unless it effectively appears already in the G_i couplings, so that they violate color parity. If it does appear as a physical region singularity in the triple-regge amplitude, as in Fig. 4.15(a), we know from the last Section (and will see explicitly in the next Section) that it has to appear in an $M^{\mathcal{C}_c}$ and/or an $M^{\mathcal{C}_b}$ amplitude. It, therefore, has to appear in the regge cut analogue of the last term of (5.94) and/or the last term of (5.90) since these are the only terms without (s_{13}) or $(s_{2'3'})$ discontinuities. But, since the anomaly has to appear in a reggeon vertex, if it appears in any of the terms in (5.94) or (5.90) then it must appear in all of them. However, the multi-regge behavior in the first term of (5.90) already represents the maximum set of physical region cuts allowed by the Steinmann relations and so can not contain the anomaly. Consequently it can not appear in any of the terms in (5.90). We can also argue that it should appear in (5.94) as follows.

We can draw the quark loop of Fig. 4.10 as in Fig. 5.7(a) with the attached gluon lines labeled by the index for the corresponding external momentum entering or exiting the associated external coupling. The double discontinuity in s_{13} and $s_{2'3'}$ puts the hatched lines on-shell as illustrated in Fig. 5.7(a). The anomaly puts the remaining unhatched lines on-shell as discussed in Section 4.

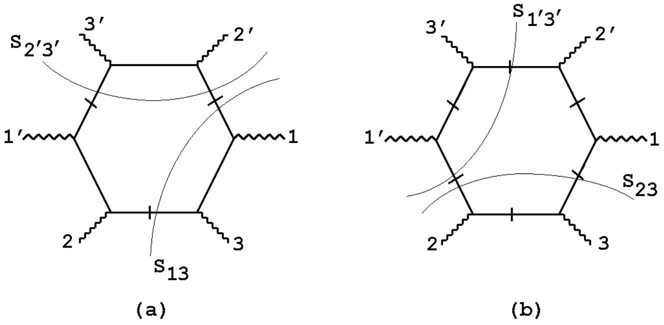

Fig. 5.7 The Quadruple Discontinuity.

As illustrated in Fig. 5.7(b) the remaining unhatched lines are also put on-shell by taking the double discontinuity in the asymptotically equivalent set of cuts $s_{1'3'}$ and s_{23}. The anomaly therefore occurs in combination with the asymptotic cuts of the triple-regge amplitude when there is a quadruple discontinuity in two sets of asymptotically equivalent cuts, in particular s_{13} and $s_{2'3'}$ together with $s_{1'3'}$ and s_{23}. (As we discuss in the next Section, the third discontinuity involved in triple-regge behavior is produced by the addition of a further gluon.) Either of the two sets of cuts can produce the anomaly while the other produces the asymptotic regge hehavior and, in fact, the two possibilities correspond to the two anomaly contributions of Fig. 4.8(a) and (b) discussed in Sections 2 and 4 that are related by a parity transformation.

Note that the chirality violating quark line is different in the two cases.

It is straightforward to determine, by comparing the asymptotic relations (5.3)-(5.8) with the light-cone formulae (3.3) and (3.4), that in the anomaly configuration $t_1 = t_2$ and $cos\ \omega_1 = cos\ \omega_2$ so that, asymptotically, $s_{13} = s_{23} = s_{1'3'} = s_{2'3'}$. This allows the quadruple discontinuity to appear in the asymptotic region. Because the Steinmann relations should be valid (asymptotically) in a physical region, the quadruple discontinuity can not approach the asymptotic region (as a function of the non-asymptotic variables) from within a physical region. It must do so from an unphysical region where, just because it is unphysical, it can contain a chirality transition. Indeed, from Fig. 5.7 it is clear that if all quark lines are on-shell then this can only be achieved in a region where there are also discontinuities in $s_{12'}$ and $s_{21'}$. This is the unphysical region where the triple discontinuity $\mathcal{C}_c$ occurs. In this region, the anomaly clearly can appear as a "physical region" singularity in combination with a triple discontinuity. If it then appears as a singularity in a reggeon interaction vertex, it can consistently appear in all four terms of (5.94), since all four represent unphysical triple discontinuities. The last term can contain the amplitude of Fig. 4.15(a) and, as will be come clear from the next Section, the initial calculation of Fig. 4.8(a) can be regarded as calculating the double discontinuity present in the first term of (5.94).

6. Multiple Discontinuities

In this Section we evaluate multiple discontinuities and look for the anomaly in reggeon interactions via the multi-regge formalism of the last Section. The writing of an asymptotic dispersion relation, without subtractions, depends[2, 14] on the feature that all asymptotic behavior originates from multi-regge singularities and our analysis implicitly assumes that all asymptotic contributions of a Feynman graph can be assigned to multi-regge amplitudes of some form.

6.1 The Simplest Diagrams

From the previos Section we know that the anomaly can only appear in amplitudes of the $M^{\mathcal{C}_c}$ form with triple discontinuities corresponding to tree diagrams of the form illustrated in Fig. 2.9(c). To count all triple discontinuities, and the diagrams that contribute to them, we first consider the initial and final state double discontinuities that are uniquely associated with each hexagraph. However, we then find that, in the triple-regge limit, the lowest-order graphs do not have a non-trivial third discontinuity that can be obtained by putting further propagators on-shell. Additional discontinuities of this kind, associated with triple-regge behavior, appear only as additional gluons are added and the reggeization effects appear as in (5.96) and (5.97).

An additional discontinuity can be trivially taken by using the equivalent of (2.3) but to strictly justify this again requires calculating the same reggeization effects. To carry out a complete study of how such triple discontinuities appear, therefore, we would need to go to at least the next order of perturbation theory. In the following we will do something in between. We know from the discussion of the previous Section that we should evaluate triple discontinuities of the form of Fig. 2.9(c). Having evaluated a double discontinuity, we will check diagrammatically that the appropriate additional discontinuity does indeed appear as additional gluons are added. We then appeal to (5.91)-(5.93), as applied to (5.97), and extract the reggeon interaction directly from the double discontinuity - in effect simply using (2.3).

A double discontinuity requires a minimum of two gluons exchanged in each t-channel. To obtain the double discontinuity in s_{13} and $s_{2'3'}$ that is associated with the first hexagraph of Fig. 5.2 we consider the diagrams of Fig. 6.1. The desired double discontinuity is obtained by putting the hatched quark lines on-shell. If we ignore gluon self-interactions, we can argue that these diagrams are a complete set as follows. The initial scattering process producing the s_{13} intermediate state is necessarily the production of a quark-antiquark pair and without loss of generality we can draw this process as in the bottom part of Fig. 6.1(a), provided we don't distinguish a quark direction on the exchanged quark line. Similarly the $s_{2'3'}$ intermediate state is associated with the reverse of this production process. The quark loop obtained by joining the amplitudes for these initial and final scatterings is either planar, as in the first six diagrams of Fig. 6.1, or it has a twist in it, as in the second six diagrams. The six diagrams of each kind are obtained by attaching the two gluons that do not participate in either the initial or final scattering process, in all possible ways.

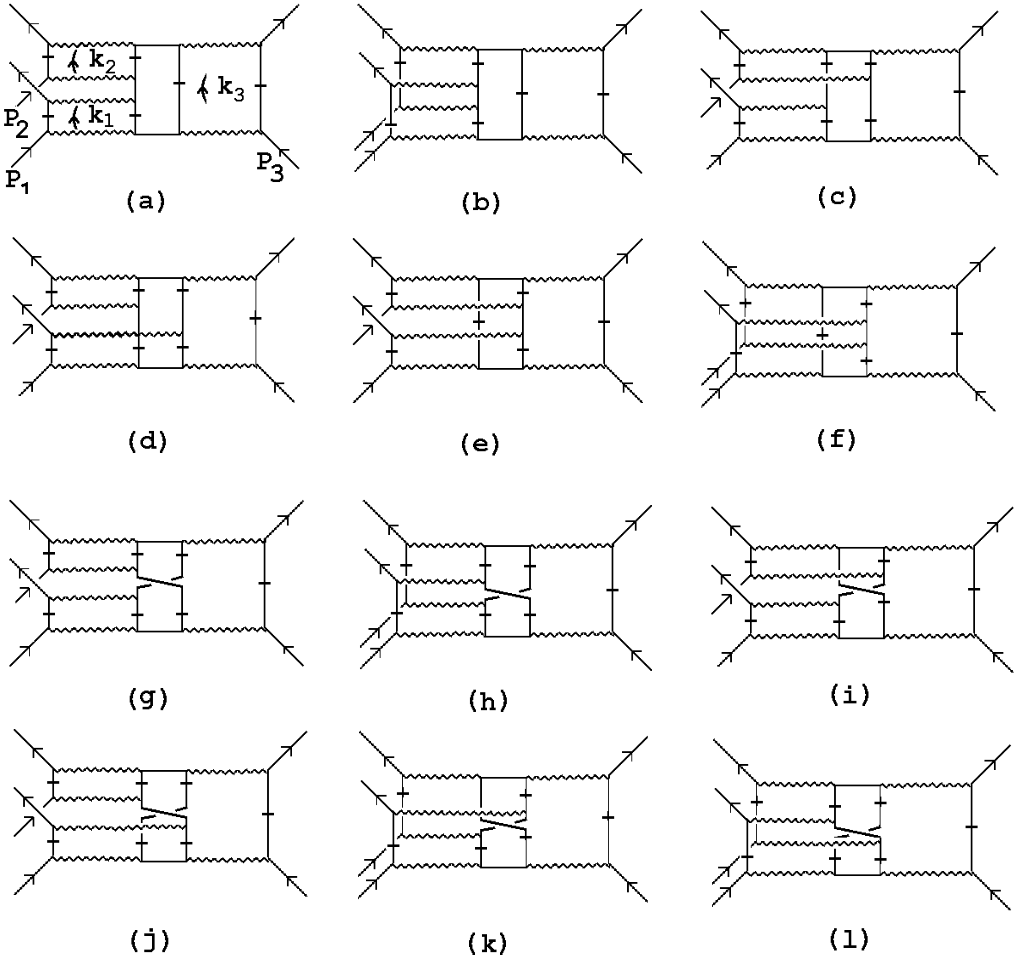

Fig. 6.1 Diagrams with Two Gluons in each t-channel.

Apart from the need to sum over the direction of the quark line around the loop, the diagrams of Fig. 6.1 are all of the lowest-order diagrams with both an s_{13} and an $s_{2'3'}$ discontinuity. We evaluate diagrams in the full triple Regge limit (3.1) in which the P_i become lightlike in distinct directions and the Q_i have the general form given in (3.1). In each case, the double discontinuity provides a sufficient number of δ-functions to perform all longitudinal integrations.

6.2 The Diagram of Fig. 6.1(a).

We have already discussed this diagram at length in sub-section 4.1. Indeed the hatched lines of Fig. 6.1(a), that are placed on-shell to obtain the double discontinuity, are the same as those of Fig. 4.2. Our previous analysis is, therefore, sufficient to determine that the anomaly is not present. There is, however, an important point concerning further discontinuities that we referred to above and applies to our analysis of all the remaining diagrams.

A-priori, there is an additional $s_{11'3}$ discontinuity which we can take by putting the only unhatched vertical line on shell. If we repeat our evaluation of Fig. 4.2 but instead use co-ordinates for the k_1 and k_2 integrations in which $\underline{n}_{1+}$ and $\underline{n}_{2+}$ are the basic light-like momenta, the longitudinal integrations will lead to the γ-matrix couplings shown in Fig. 6.2

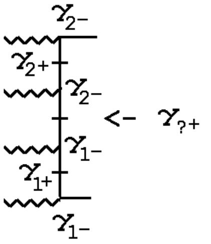

Fig. 6.2 γ-Matrix Couplings for Fig. 6.1(a)

If the middle quark line is to put be put on-shell and give a leading contribution, then it must be helicity-conserving with respect to both the upper and lower on-shell states. However, this is clearly not possible since both options give a product of γ-matrices that is zero.

As we will see below, this last point applies generally to all the diagrams we discuss. The triple-regge behavior we are looking for is inconsistent with taking a discontinuity through a remaining uncut quark line. For the diagram under discussion we note that while we can not introduce an $s_{11'3}$ discontinuity without cutting the forbidden quark line we can introduce an unphysical $s_{1'2}$ discontinuity by adding an extra gluon, as illustrated in Fig. 6.3.

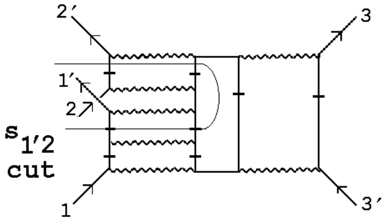

Fig. 6.3 An $s_{1'2}$ Discontinuity Introduced by Adding an Extra Gluon.

(The lines placed on-shell by the additional discontinuity are indicated by the hatches on the thin line showing how the discontinuity is taken.) In this way we can replace a single real gluon in the original diagram by the one-loop contribution to the reggeization of this gluon. We must, of course, remember that a cut gluon of this kind has necessarily to be considered as reggeized when we extract reggeon interactions.

In general we expect that the sum total of higher-order triple discontinuity contributions that produce reggeization effects will simply determine that the lower-order diagram is obtained as a generalised "real part". The reggeon vertex obtained from the original diagram, with no additional discontinuity taken, will then be obtained. The existence of the $s_{1'2}$ discontinuity implies that the reggeon interaction obtained from Fig.g 6.1(a) will appear in the triple regge amplitude associated with the triplet $\mathcal{C}_c$ discussed in the last Section. However, since only one set of cuts appears, we expect the arguments of Section 4 that the six-reggeon interaction computed from Fig. 6.1(a) will be zero when all-orders reggeization effects are included will be valid.

6.3 Isolating the Anomaly

In all of the remaining diagrams of Fig. 6.1, one or more of the k_i loop momenta flow through more than one line of the internal quark loop. Consequently, as we already saw in Section 4, the reduction of the k_i integrations to two dimensions is not as straightforward as it was for Fig. 6.1(a). The internal quark loop and the remaining two-dimensional k_i integrations are not, in general, coupled only by an effective point-coupling and the reggeon vertices generated are very complicated. As we have made clear already, we will not attempt to obtain complete expressions for the vertices generated by the remaining diagrams in Fig. 6.1. Rather we will concentrate on isolating contributions that might contain the anomaly.

Our search for the anomaly will, as in Section 4, be based on the discussion of Appendix A. We will look for effective vector-like point-couplings for the three vertices of a quark triangle diagram with an odd number of axial couplings. We will also look for the appropriate flow of a light-like momentum through the reggeon vertex. We will assume that the anomaly, if present in a diagram, can be found using any of the possible sets of light-cone variables discussed in Appendix B, provided we consider all choices for assigning particular quark propagators to particular longitudinal k_i integrations. As will become clear, the appropriate choice of variables will often enable us to see immediately whether a local coupling occurs or whether only non-local couplings arise.

6.4 The Diagram of Fig. 6.1(b).

At first sight this diagram has an s_{123} discontinuity obtained by cutting the remaining uncut vertical line in Fig. 6.1(b) However, as illustrated in Fig. 6.4, the helicity conservation problem again arises.

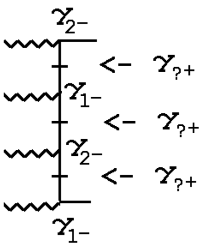

Fig. 6.4 γ-Matrix Couplings for Fig. 6.1(b)

There are two on-shell scatterings for which it is impossible to choose helicities such that both give the leading behavior. Instead we can introduce an s_{123} discontinuity by adding an extra gluon, as illustrated in Fig. 6.5(a).

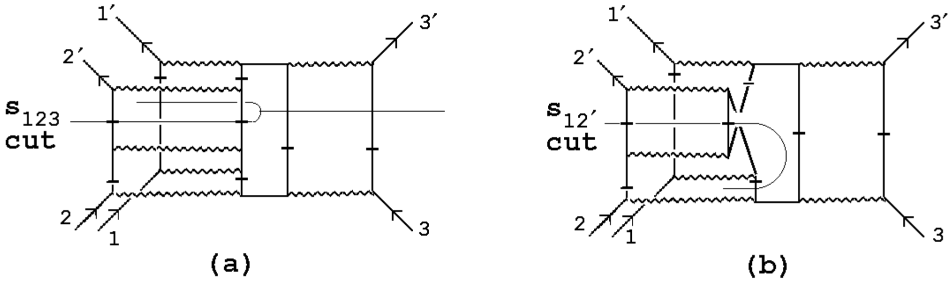

Fig. 6.5 Adding a Gluon to Fig. 6.1(b) to Give Additional Discontinuities.

Alternatively, adding a gluon line as in Fig. 6.5(b) gives an unphysical discontinuity in $s_{12'}$. (As before, the lines placed on-shell by the additional discontinuity are indicated by the hatches place directly on the thin line showing how the discontinuity is taken.) The two discontinuities are closely related, as anticipated in the previous Section. Again using the additional gluon loop to provide the reggeization of the gluon, the appropriate reggeon vertex is that given by the original diagram of Fig. 6.1(b) (apart from a normalization factor that we are not attempting to determine anyway).

The momentum flow through the internal quark loop of Fig. 6.1(b) and the γ matrices involved are shown in Fig. 6.6. As in our discussion of diagrams in Section 4, we use the light-cone co-ordinates $(k_{i1^-}, k_{i2^-}, \underline{\tilde{k}}_{i\perp})$ introduced in Appendix B to perform the k_1 and k_2 integrations and to evaluate the γ-matrix trace associated with the quark loop. For the k_3 integration, the choice of co-ordinates is not critical. For simplicity, we choose conventional light-cone co-ordinates $(k_{3^+}, k_{3^-}, k_{3\perp})$. Our evaluation of the integral I_i of Fig. 4.3 can be repeated to perform the k_{11^-}, k_{22^-} and k_{3^-} integrations using the δ-function associated with the correponding external quark line.

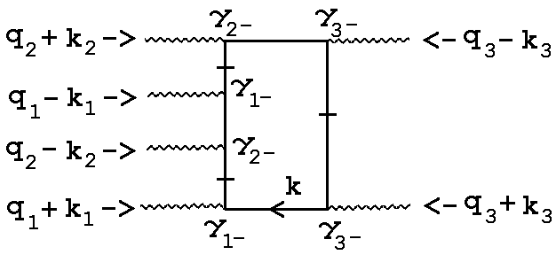

Fig. 6.6 The Quark Loop in Fig. 6.1(b).

To perform the remaining longitudinal integrations we first route the k_i momenta along the shortest path through the quark loop. This matches a unique on-shell (hatched-line) propagator in the loop with each k_i. As before, to look for a potential γ-matrix point-coupling, we look for that momentum factor within the numerator of the on-shell quark that is multiplied by the same momentum that is scaling the longitudinal momentum integrated over via the δ-function. In particular the k_{12-}-integration has the form

$$\begin{aligned}
&\int dk_{12-}\ \delta\Big((k_1+k+Q_1)^2-m^2\Big)\ \gamma_{1-}\ \Big((k_1+k+Q_1)\cdot\gamma-m\Big)\ \gamma_{2-}\times\quad\cdots \\
&\qquad=\ \int dk_{12-}\ \delta\Big((k_{11-}+k_{1-}+Q_{11-})k_{12-}+\cdots\Big) \\
&\qquad\qquad\times\gamma_{1-}\ \Big((k_{11-}+k_{1-}+Q_{11-})\cdot\gamma_{2-}+\cdots\Big)\ \gamma_{2-}\ \times\ \cdots \\
&\qquad=\ \gamma_{1-}\gamma_{2-}^2\ +\ \cdots \\
&\qquad=\ 0\ +\ \cdots
\end{aligned}\tag{6.1}$$

In this case the potential point-coupling from the $(k_{11-}+k_{1-}+Q_{11-})\gamma_{2-}$ term in the quark numerator is eliminated by one of the adjacent γ-matrices (c.f. our evaluation of Fig. 4.8(a) in sub-section 4.3). Since the k_{21-} integration has the same structure as the k_{12-} integration, performing each of these integrations will produce couplings of the form (C.19) rather than the point couplings necessary to produce the anomaly. In any alternative momentum flow and assignment of δ-functions, it is straightforward to show that either the k_{12-} or the k_{21-} integration gives an analagous result to (6.1), i.e. only non-local couplings remain. (Note that our choice of light-cone co-ordinates has enabled us to reach this conclusion rather simply).

6.5 The Diagrams of Fig. 6.1(c) and (d).

Because of the number of lines put on-shell by taking the s_{13} and $s_{2'3'}$ discontinuities, there are not three quark lines off-shell in either of these diagrams. As a result there is no possibility to generate the anomaly divergence.

6.6 The Diagram of Fig. 6.1(e).

This diagram is similar to that of Fig. 4.8(a) (which can be identified with Fig. 6.1(f) discussed next) and can be analysed similarly. In fact, as we discussed in Section 2 and discuss further below, the reggeon vertices obtained from Figs. 6.1(e) and (f) are related by reggeon Ward identities and so must have similar properties. We route the k_i momenta through the (unique) shortest path combination and again use the light-cone co-ordinates $(k_{i1^-}, k_{i2^-}, \tilde{\underline{k}}_{i\perp})$ together with conventional light-cone co-ordinates $(k_{3^+}, k_{3^-}, k_{3\perp})$. Integrating the longitudinal momenta and keeping local couplings produces the γ matrix assignment of Fig. 6.7(a). Comparing with Fig. 4.13 and the following analysis we see that the three γ_5 couplings generated are identical to those generated by Fig. 4.8(a) and Fig. 6.1(f). A momentum configuration for Fig. 6.1(e) that parallels Fig. 4.15(a) is shown in Fig. 6.7(b). This configuration has already appeared in Fig. 2.6(b).

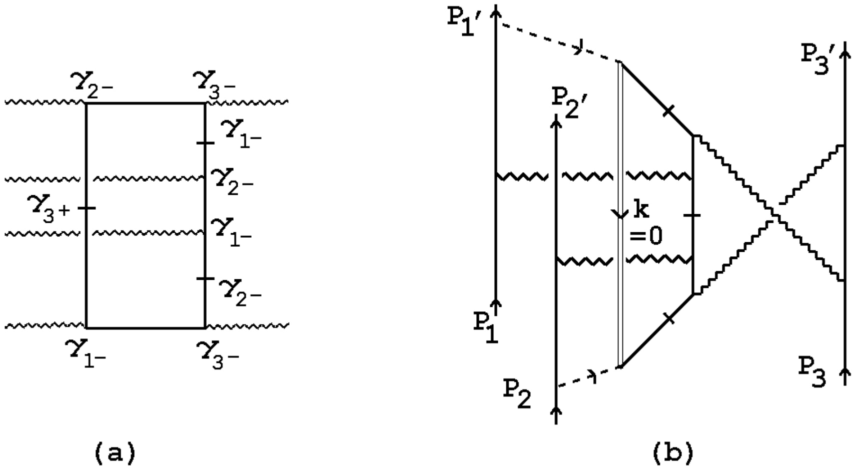

Fig. 6.7 (a) γ-Matrices and (b) Anomaly Momentum Configuration for Fig. 6.1(e).

As in Fig. 4.15(a), the scattering process containing the anomaly takes place in a part of the physical region where the original discontinuities used to evaluate the reggeon interaction vertex are no longer present. This is consistent with the discussion at the end of the last Section, provided the unphysical $s_{1'2}$ discontinuity is present so that the anomaly is associated with an unphysical triple discontinuity. The helicity conflict again prevents a further discontinuity being taken by cutting the remaining vertical quark line. Considering discontinuities obtained by cutting gluon lines we find that the unphysical $s_{1'2}$ discontinuity is indeed the only one that can be taken. We conclude that Fig. 6.1(e) does generate the anomaly, just as the reggeon Ward identity relationship that we discuss below requires.

A-priori, we might suspect that the contribution of Fig. 6.1(e) will not persist if all-orders reggeization effects are included. The lack of additional discontinuities can be traced to the essential planarity of the coupling to the t_3-channel gluon exchanges. As discussed in Section 4, this would be expected to allow a contour closing that will give zero as higher-order reggeization effects are added. However, as we discuss briefly in the next Section, the anomaly produces both ultra-violet and infra-red effects. If it is not canceled in the sum of all diagrams it's ultra-violet effects could prevent such contour closing arguments. Alternatively, if the contour closing arguments can be carried through it would imply that all properties of the anomaly and it's relationship to reggeon Ward identity zeroes would be contained in the maximally non-planar diagram.

6.7 The Diagram of Fig. 6.1(f).

This diagram has already appeared extensively in early Sections, as the maximally non-planar diagram of Figs. 2.2 and 2.4, and in Fig. 4.8(a) with the hatched lines put on-shell just as in Fig. 6.1(f). The extensive discussion in Section 4 showed that the the anomaly is present although, very importantly, the momentum configuration in which it appears occurs in a part of the physical region distinct from that in which the discontinuities are evaluated. In the previous Section we concluded that this is resolved by associating the anomaly with an unphysical triple discontinuity. The helicity mismatching encountered above again implies that to take additional discontinuities we must cut through gluon lines. In Fig. 6.8 we have shown that both an s_{123} discontinuity and $s_{1'2}$ discontinuity can be obtained.

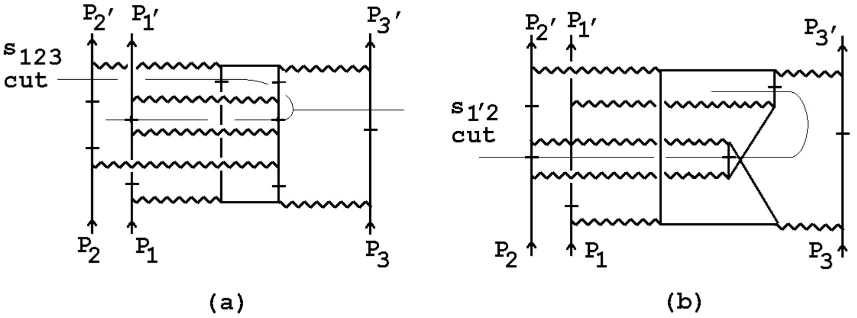

Fig. 6.8 Further Discontinuities of Fig. 6.1(f).

(The hatched lines directly on the thin line again indicate the on-shell particles producing the new discontinuity). This implies the diagram will continue to provide a six-reggeon interaction containing the anomaly as reggeization effects are added. According to the argument of the last Section, the anomaly has to go into the reggeon interaction vertex associated with the unphysical $s_{1'2}$ discontinuity.

Moving on to the twisted diagrams of Fig. 6.1, we will find that two of these diagrams contain the appropriate local couplings, but can not satisfy all the constraints on the momentum flow. These two diagrams are also related to Fig. 6.1(f) via reggeon Ward identities.

6.8 The Diagrams of Fig. 6.1(g) - (j).

The diagrams of Fig. 6.1(g) and (h) also appear in Fig. 4.6, except that an extra line is now on-shell. In Section 4 we argued that such diagrams do not contain the anomaly. With the extra line on-shell we again have only two quark lines off-shell and so clearly there is no triangle anomaly.

6.9 The Diagrams of Fig. 6.1(k) and (l).

The diagrams of Fig. 6.1(k) and (l) both have s_{123} and unphysical $s_{1'2}$ discontinuities that can be taken through a gluon line. Fig. 6.1(l) is simply obtained from Fig. 6.1(k) by time reversal of the scattering process and so has analagous properties. Therefore our discussion below of Fig. 6.1(k) will immediately extend to Fig. 6.1(l).

We can repeat much of the discussion of Fig. 6.1(e) and (f) for Fig. 6.1(k). We do this briefly as follows. For reasons that will soon become apparent we reverse the sign of k_2 and obtain the internal quark loop contribution shown in Fig. 6.9.

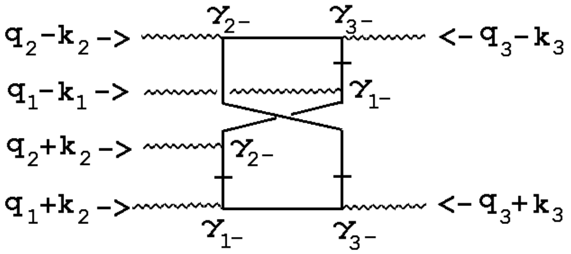

Fig. 6.9 The Quark Loop in Fig. 6.1(k).

If we take the shortest routes for each of the k_i momenta then we find that, in parallel with our discussion of Fig. 6.1(b), neither the k_{12^-} nor the k_{21^-} integrations give local couplings. The only δ-function assignment giving local couplings at all vertices is that shown in Fig. 6.10(a), with the corresponding momentum flow shown in Fig. 6.10(b).

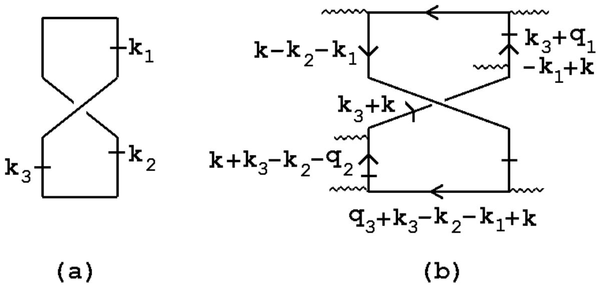

Fig. 6.10 Another (a) δ-function Assignment and (b) Momentum Flow for Fig. 6.9.

The calculation of local couplings proceeds as usual. The couplings generated differ from those of Fig. 4.13 only in that

$$\hat{\gamma}_{31} \;=\; \gamma_{3-}\gamma_{2-}\gamma_{1-} \;\rightarrow\; \hat{\gamma}_{13} \;=\; \gamma_{1-}\gamma_{2-}\gamma_{3-} \;=\; \gamma_{-,+,-} \;-\; i\,\gamma_{-,-,-}\,\gamma_5 \qquad (6.2)$$

and so the three γ_5 couplings needed for the anomaly are again present. The momentum flow and couplings in the corresponding triangle diagram are shown in Fig. 6.11.

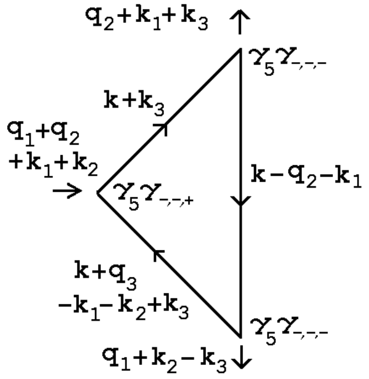

Fig. 6.11 The Triangle Diagram Generated by Fig. 6.1(k).

At this point we note that Fig. 6.11 is identical to Fig. 4.14, apart from a shift of the internal momentum

$$k \quad\rightarrow\quad k - q_2 - k_1 \qquad (6.3)$$

We would then expect the anomaly to appear in the limit (4.22), with $(q_1 + q_2 + k_1 + k_2) = 0$ and $(q_2 + k_1 + k_3)$ light-like in the limiting configuration. However, if the shift (6.3) is made, k_1 is routed along a different path and the δ-function assignment of Fig. 6.9(a) can no longer be made. Therefore, the momentum configurations of Fig. 6.11 must be kept. Since the anomaly has to be generated when the vertical momentum line of Fig. 6.10 carries stricyly zero momentum, in the limiting configuration we must also have

$$k = q_2 + k_1 \qquad (6.4)$$

and must combine this with the mass-shell δ-constraints determining k_{12-}, k_{21-} and k_{33+} that replace (4.23)-(4.25). Imposing (6.4), these constraints give

$$(k_3 + q_1 + k - k_1)^2 \;=\; (k_3 - q_3)^2 \;=\; 0 \qquad (6.5)$$

$$(k + k_1 + k_2)^2 \;=\; (q_2 + k_2 + 2k_1)^2 \;=\; (k_1 - q_1)^2 \;=\; 0 \qquad (6.6)$$

$$(k + k_3 - q_2 - k_2)^2 \;=\; (k_3 + k_1 - q_2)^2 \;=\; 0 \qquad (6.7)$$

From (6.5) we see immediately that the anomaly divergence associated with Fig. 6.1(k) can only coincide with that of Fig. 6.1(f) at $q_3 - k_3)^2 = 0$.

6.10 Reggeon Ward Identities

It is not an accident that the diagram of Fig. 6.1(k) contains the same γ-matrix structure as that of Fig. 6.1(f). In fact a reggeon Ward identity determines that it has to contribute equally (and, when color factors are appropriate, with opposite sign) at a zero momentum point, such as $(q_3 - k_3)^2 = 0$. Consider the two sets of amplitudes forming s_{13} discontinuities as in Fig. 6.12,

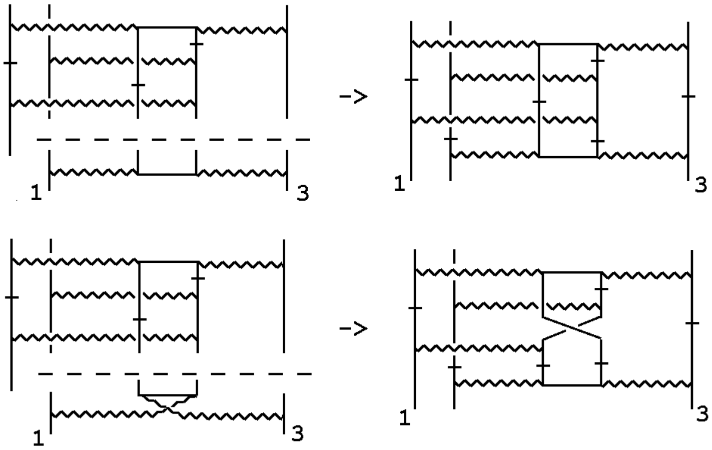

Fig. 6.12 Forming s_{13} Discontinuities

The upper set gives Fig. 6.1(f) while the lower set gives Fig. 6.1(k). The two lower production amplitudes that distinguish the diagrams are related by the reggeon Ward identity illustrated in Fig. C6. Therefore, when the central quark/antiquark pair carries zero color, the two diagrams must cancel at the zero momentum point. Fig. 6.1(l) is similarly related to Fig. 6.1(f) via final state amplitudes satisfying a reggeon Ward identity.

As we noted above, Fig. 6.1(e) is also related to Fig. 6.1(f) by a reggeon Ward identity. In this case the unphysical $s_{1'2}$ discontinuity has to be considered. The triple gluon diagram of Fig. C6 (the third diagram) can not contribute when the quark exchange exchange in the first two diagrams involves a zero momentum chirality transition, as is the case in the anomaly divergence. Therefore, when the quark/antiquark pair (involved in the $s_{1'2}$ discontinuity) carries octet color the anomaly contributions in Fig. 6.1(e) and (f) will not cancel and there will be no triple gluon contribution. The reggeon Ward identity will necessarily be violated when the light-cone momenta corresponding to the anomaly are present. That a reggeon Ward identity could fail for a quark loop in which all lines are are on-shell was emphasized in [12].

The reggeon Ward identity is, however, sufficient to ensure that if the anomaly in maximally non-planar diagrams cancels then so must the contribution of all diagrams having the form of Fig. 6.1(e). Note that for the contribution of the maximally non-planar diagram of Fig. 2.4 to other hexagraphs (such as that associated with the scattering processes of Fig. 4.9), the Feynman diagram corresponding to Fig. 6.1(k) actually plays the role of Fig. 6.1(e). We conclude, therefore, that we can focus only on Fig. 6.1(f) in Fig. 6.1. To discuss whether the anomaly cancels we have to consider only the sum of the double discontinuities of the form of Fig. 6.1(f), each of which is associated with a separate hexagraph. In Section 4, we have already discussed the kinematical symmetries that will produce a cancelation. We enlarge this with a discussion of color factors in the next Section.

6.11 Feynman Diagrams Versus Multiple Discontinuities

At the end of the previous Section we explained how it is that the anomaly can occur in physical region momentum configurations where the discontinuities associated with the propagators that are put on-shell are no longer present. To be clear we would like to reiterate the logic that we are employing. As we outlined in Section 2, in principle we can study Feynman diagrams directly and look for propagators that are placed on-shell (or close to on-shell) by the triple-regge limit. In part this is what we did in Section 4. The very large number of diagrams, as well as their complexity, makes it essentially impossible to apply this procedure to all diagrams. We have instead proceeded by using the multi-regge theory of the previous Section which tells us that the anomaly could appear in specific multi-regge amplitudes which have the discontinuities that we have calculated directly. We then extract the reggeon vertices calculated from the discontinuities and insert them back into the multi-regge formulae. In this way we obtain amplitudes that describe triple-regge scattering away from the discontinuities. If the anomaly divergence then occurs in a physical region within the multi-regge formula, for consistency it should occur in a corresponding way in some Feynman diagram. This is what we demonstrate when we show space-time scattering diagrams such as those of Fig. 4.15 and Fig. 6.7(b). We have emphasized, however, that the discontinuity structure given by the multi-regge amplitudes is not the same as is found in individual diagrams. Consequently, a multiple discontinuity and real anomaly configuration that appear in the same Feynman graph do not generally appear in the same multi-regge amplitude.

7. Color Factors, Cancelations and Divergences

We have narrowed down a discussion of the cancelation of the anomaly, at lowest-order, to contributions from double (or triple) discontinuities occurring in Feynman diagrams of the maximally non-planar type. In Section 4 we already discussed the kinematical symmetries that can produce a cancelation. As a result we need give only a minimal discussion of the role played by color quantum numbers and signature properties.

When signatured amplitudes are formed the two-reggeon state appears only in even signature channels. The reggeon interactions containing the anomaly that we have discussed couple two reggeized gluons in each t_i-channel and so all three channels have $\tau_i = 1$. Therefore the signature rule of Section 5 is immediately satisfied. To obtain an amplitude for which all signatures are positive we add the contributions from all eight of the hexagraphs in Fig. 5.3. This requires that we add the contributions of the twisted diagrams of the form of Fig. 4.16 to the untwisted contributions of Figs. 4.8(a) and (b).

To begin our discussion of color factors we first consider the external coupling of two gluons (or reggeons) to a scattering quark. The color factor that appears can be written as shown diagrammatically in Fig. 7.1.

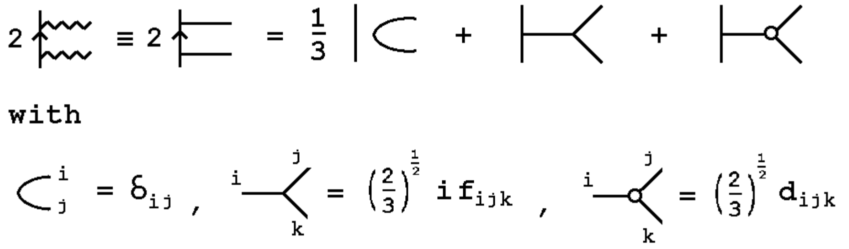

Fig. 7.1 Color Factors for Two Gluons Coupling to Two Quarks

f_{ijk} and d_{ijk} are the usual antisymmetric and symmetric tensors for SU(3) color. In lowest order, the G_h have no momentum dependence and so, in the even signature amplitude, only the symmetric δ_{ij} and d_{ijk} couplings survive. Therefore, the (two-gluon) two-reggeon state has to be in either a color zero state, or a "symmetric octet" (8_s) state. At this order it is obvious that a single scattering quark does not couple to an "anti-symmetric octet" (8_a) two-reggeon state.

It will be important to discuss the color parity of reggeon states. Color charge conjugation on gluon fields is defined by the transformation of gluon color matrices

$$A^i_{ab} \rightarrow \; - \; A^i_{ba} \qquad (7.1)$$

For SU(3) we can choose $A^i \sim \lambda^i$ so that

$$A^i \ \rightarrow \ -A^i \quad i=1,3,4,6,8 \ , \qquad A^i \ \rightarrow \ A^i \quad i=2,5,7 \ , \tag{7.2}$$

For a trace of gluon matrices the color charge conjugation reverses the trace order. In particular, in a space-time path-ordered integral of gluon fields it reverses the direction of the path integration. For gauge-invariant states involving such integrals there may be an inter-relation between color parity and space-time symmetry properties.

We consider the minus sign in (7.1) as defining the negative color parity of the gluon. The odd-signature reggeized gluon then has a color parity equal to it's signature. Color-zero combinations of color matrices also have a definite color parity, e.g.

$$\begin{gathered} \delta_{ij} \ A^i A^j \ \rightarrow \ \delta_{ij} \ A^i A^j \ , \qquad f_{ijk} \ A^i A^j A^k \ \rightarrow \ f_{ijk} \ A^i A^j A^k \ , \\ d_{ijk} \ A^i A^j A^k \ \rightarrow \ - \ d_{ijk} \ A^i A^j A^k \end{gathered} \tag{7.3}$$

i.e. the d-tensor provides a "color parity violating" coupling for gluon fields. Ultimately our main interest is in color zero multi-reggeon states and these can immediately be assigned a color parity. Also since

$$\begin{gathered} f_{ijk} \ A^j A^k \ / \ A^i \ \rightarrow \ f_{ijk} \ A^j A^k \ / \ A^i \ , \\ d_{ijk} \ A^j A^k \ / \ A^i \ \rightarrow \ - \ d_{ijk} \ A^j A^k \ / \ A^i \end{gathered} \tag{7.4}$$

we can assign negative and positive color parities, respectively, to the 8_a and 8_s states discussed above. We can also assign color parities to multi-reggeon states with color factors containing combinations of f- and d- tensors. Any reggeon state, and in particular an even-signature 8_a two-reggeon state, has "anomalous color parity" if it has a color parity not equal to it's signature. We will argue below that, in general, anomalous color parity reggeon states do not couple to a scattering quark.

Color charge conjugation invariance implies color charge parity conservation and so, after summing over quark directions, the quark loop color factor must contain an even number of d-tensors. Given the color structure of the external couplings, the possible color couplings for the Γ_6 reggeon interaction extracted from the lowest-order diagrams are those shown in Fig. 7.2

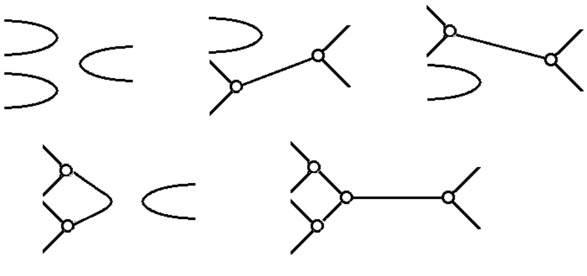

Fig. 7.2 Color Factors for the Lowest-Order Reggeon Interaction

In lowest-order, therefore, both the color factors and the remaining k_i-integrations are symmetric with respect to the two reggeons in each of the t_i channels. From Section 4 we know that this implies the anomaly is canceled.

In higher-orders, helicity conserving couplings $G_h(q_i, k_i)$ that appear within multiple discontinuities, need not be symmetric under $k_i \leftrightarrow -k_i$. Therefore, the 8_a two-reggeon state could appear in such discontinuities. However, as explained in Section 5, a positive signatured amplitude can be obtained either by adding hexagraph amplitudes or by adding full amplitudes related by a CPT transformation applied selectively to external states. For an external (left-handed) scattering quark q_L, the second procedure gives directly that the full signatured coupling is as shown in Fig. 7.3. Because of helicity conservation, the two vertices in Fig. 7.3 are also related by a CP transformation. Therefore, since CP is conserved, their equality in lowest-order must extend to all orders. Consequently, the two-reggeon coupling remains symmetric to all orders and the 8_a state does not couple.

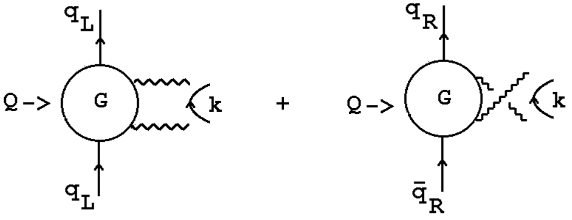

Fig. 7.3 The Signatured Two-Reggeon Coupling to a Quark

More generally, even signature implies that the external "state" formed by the initial and final scattering particles is even under CPT. Therefore, the internal two-reggeon state must similarly be even. Since the reggeon state lies entirely in the transverse plane, it is independent of the T transformation. Therefore, it must be even under CP. (The same conclusion could be reached by working in the t-channel.) The antisymmetry in the k_i integrations required for the anomaly is equivalent to requiring $P = -1$ for the two-reggeon state, which must, therefore carry anomalous color parity, i.e. $C = -1$.

A-priori, the necessary parity antisymmetry for the two-reggeon state could appear if there is helicity non-conservation. If we consider scattering gluons then helicity-flip vertices coupling a reggeized gluon do appear in next-to-leading order[6]. However, parity conservation, applied when the reggeized gluon goes on-shell, implies there is a change of sign when the gluon helicity is reversed. This determines that the "anomalous color parity" 8_a two-reggeon state again decouples in all orders. More generally, we anticipate that no reggeon states with anomalous color parity couple to scattering quarks (or gluons). By appealing to instanton interactions we could introduce hypothetical external couplings that are helicity non-conserving and that violate CP conservation. However, our belief is that the anomaly will ultimately force a choice of scattering states in order to satisfy unitarity. Therefore, we wish to first determine whether there is a level at which the anomaly does cause a problem if we use the quark and gluon states of perturbation theory.

The parity asymmetry needed to couple the anomalous color parity two-reggeon state can be obtained if we add an extra particle (or particles) to the initial or final state as in Fig. 7.4.

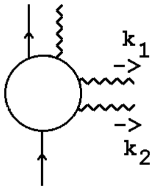

Fig. 7.4 A Two-Reggeon Coupling with an Additional Final State Gluon.

This coupling can be directly studied in the two-to-four amplitude[14] where the novel signature properties produced by an imbalance between discontinuities is well-known. Nevertheless, even if all three external couplings have the required asymmetry between initial and final states, a triple-regge amplitude containing the anomaly still can not exist, because of the conservation of color parity. An equivalent way of stating this is to say that for the anomaly to appear in the coupling of three 8_a two-reggeon states, a d-tensor coupling is required that violates color parity conservation. Unless the external couplings for two-reggeon states violate color parity conservation (or, equivalently, an analogue of the anomaly appears in the external couplings) overall color parity conservation will force the cancelation of the triple-regge anomaly amplitude.

We can outline how we anticipate the anomaly does appear in amplitudes as follows, although more explicit verification is clearly required. In a ditriple regge limit reggeon diagrams, of the form illustrated in Fig. 7.5, containing two anomaly vertices can appear. A single d-coupling can be present for each anomaly vertex while the full amplitude conserves color parity.

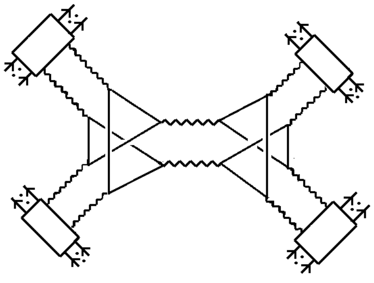

Fig. 7.5 A Ditriple-Regge Limit Amplitude.

It is then important to note that the external coupling will have reggeon Ward identity zeroes[12] (which follow from gauge invariance). For example, the coupling of Fig. 7.4 has a zero when either k_1 or $k_2 \to 0$. The anomaly divergence occurs at just such points. If the corresponding zeroes are present in all four of the external couplings of Fig. 7.5, the linear divergence of the anomaly will always be compensated by at least two Ward identity (linear) zeroes and this will be sufficient to prevent an infra-red divergence of the full amplitude. (The logarithmic divergences due to zero mass gluon propagators do not affect this argument.)

We anticipate that all reggeon states coupling to anomaly vertices will have anomalous color parity to compensate for the antisymmetric parity properties of the anomaly. For example, reggeon interactions containing the anomaly will appear in any amplitude of the form of Fig. 7.6

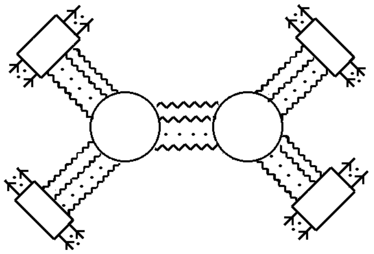

Fig. 7.6 A General Ditriple-Regge Reggeon Amplitude

provided that there is sufficient imbalance between the initial and final states that anomalous color parity reggeon states appear and provided that the signature conservation rule is satisfied. Reggeon Ward identity zeroes will continue to prevent the occurrence of divergences in full amplitudes.

In general multi-regge limits, reggeon diagrams containing any number of pairs of anomalous vertices will similarly appear[12]. Even though infra-red divergences will not appear, the ulltraviolet presence of the anomaly (that must accompany it's infra-red appearance) most likely still causes problems. We expect the large momentum region of the triangle graph to give behavior of the form of (4.42) but with $l \sim p_1, p_2, p_3 \ \to \infty$ When embedded in diagrams such as that of Fig. 7.6 we expect this behavior to produce a powerlike enhancement of the asymptotic behavior that ultimately conflicts with unitarity. In [12] we proposed to avoid this conflict by introducing large (but finite) mass fermion Pauli-Villars regulators at finite (but small) physical quark mass. If the "physical" reggeon S-Matrix is obtained, as we anticipate, by taking the quark mass to zero and extracting infra-red divergent contributions from anomaly amplitudes, the regulator fermions will not appear. To produce infra-red divergent amplitudes, however, we have to introduce external reggeon couplings that produce a reggeon condensate. This is essentially equivalent to introducing the anomaly directly in external couplings. This is the program, mentioned in the Introduction, that is outlined at length in [12] and that we plan to return to in succeeding papers.

Essentially the correct phenomenon is outlined in [12]. However, there are some differences. In particular, because of the signature conservation for anomalous amplitudes, there is no triple anomalous odderon vertex, as we assumed. Instead, the anomaly divergence occurs within the primary momentum carrying interactions of a reggeon diagram and not just in accompanying vertices as was suggested in [12]. This is possible because, as we now understand, the anomaly divergence occurs when only some of the interacting reggeized gluons carry zero transverse momentum. As we noted above, a very important consequence of the signature rule is that it promises to explain the even signature of the pomeron - a property that previously we had not clearly seen the origin of. We will not describe the infra-red divergence phenomenon any further in this paper, but simply note that in Fig. 2.8 we have already portrayed the general phenomenon that we expect to occur.

Acknowledgements

I am grateful to both Jochen Bartels and Lev Lipatov for very useful discussions on the contents of this paper.

Appendix A. The Infra-Red Triangle Anomaly and Chirality Violation

It has been known[23] for a long time that the triangle anomaly is not only an ultra-violet phenomena but is also manifest in the infra-red region when the fermions involved are massless. This was elaborated in detail by Coleman and Grossman[10] in the context of establishing 't Hooft's anomaly matching condition for confining theories. Closely related results were also obtained in [25].

In the body of the paper we use the infra-red properties of the anomaly to establish it's presence in particular reggeized gluon interactions. The Coleman and Grossman analysis establishes that the vertex function for three axial vector currents has a singularity when the quark fields involved are massless. As we describe below, the maximal divergence is obtained when all the spacelike momenta flowing through the vertex are scaled uniformly to zero while a finite light-like momentum remains. The presence of the light-like momentum is a crucial ingredient.

In the notation of Fig. A1, J^a is the axial current and

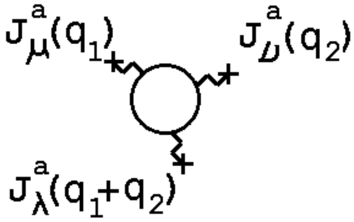

Fig. A1 The Three-point Function

the three current vertex function $\Gamma^{\mu\nu\lambda}$ can be decomposed in terms of invariant amplitudes as follows

$$\Gamma^{\mu\nu\lambda}(\mathsf{q}_1,\mathsf{q}_2) \;=\; A\,\epsilon^{\nu\lambda\alpha\beta}\mathsf{q}_{1\alpha}\mathsf{q}_{2\beta}\mathsf{q}_1^{\mu} \;+\; \cdots \;+\; B\,\epsilon^{\mu\nu\lambda\alpha}\mathsf{q}_{1\alpha} \;+\; \cdots \qquad (A.1)$$

The omitted terms are obtained from those shown explicitly by appropriate permutations. The crucial result from [10] is that the anomaly equation

$$\mathsf{q}_{1\mu}\,\Gamma^{\mu\nu\lambda}(\mathsf{q}_1,\mathsf{q}_2) \;=\; \tilde{A}\,\epsilon^{\nu\lambda\alpha\beta}\mathsf{q}_{1\alpha}\mathsf{q}_{2\beta} \qquad (A.2)$$

implies that, when $\mathsf{q}_1^2 \sim \mathsf{q}_2^2 \sim (\mathsf{q}_1+\mathsf{q}_2)^2 \sim \mathsf{q}^2 \to 0$ the invariant amplitude A has a pole at $\mathsf{q}_1^2 = 0$ with the coefficient $\tilde{A}$ given by the anomaly. Therefore, as $\mathsf{q}^2 \to 0$ we have

$$\Gamma^{\mu\nu\lambda}(\mathsf{q}_1,\mathsf{q}_2) \;=\; \tilde{A}\,\epsilon^{\nu\lambda\alpha\beta}\,\frac{\mathsf{q}_{1\alpha}\mathsf{q}_{2\beta}\mathsf{q}_{1\mu}}{\mathsf{q}_1^2} \;+\; \cdots \qquad (A.3)$$

The ultra-violet anomaly appears also in the vertex function for one axial current and two vector currents and in Ref. [25] it is shown how the corresponding Ward identities similarly imply the presence of the divergence (A.3) when the quarks involved are massless. We also refer to this result in our discussion of reggeon vertices.

If the chiral symmetry associated with the axial current J^a_μ is spontaneously-broken by a quark condensate, the pole at $\mathsf{q}_1^2 = 0$ is associated with the corresponding Goldstone boson. In our case, the anomaly equation (A.2) for the $U(1)$ current is invalidated by non-perturbative, non-trivial topological, gluon field configurations - instantons in particular[‡‡]. However, our initial purpose is to first discover a "perturbative" contribution of the anomaly within reggeon diagrams and only later determine it's dynamical significance. In this case we can use a divergence of the form (A.3) as a signal of the anomaly.

If we simply take all components of q_1 and q_2 to scale with q then (A.3) gives the (dimensional) result

$$\Gamma^{\mu\nu\lambda} \underset{\mathsf{q} \to 0}{\sim} \mathsf{q} \qquad (A.4)$$

We obtain more singular behavior as follows. First, choose μ to be a light-cone index "+" and choose

$$\mathsf{q}_1^\mu = \mathsf{q}_1^+ = \mathsf{q}_{1-} = \mathsf{p} \not\to 0 \, , \quad \mathsf{q}_1^- = \mathsf{q}_{1+} = 0 \qquad (A.5)$$

Choosing q_2, and all spacelike momenta flowing through the diagram, to be $O(\mathsf{q})$ and to lie in a spacelike plane orthogonal to the space component of q_1^+, we obtain from (A.3)

$$\Gamma^{++\lambda}(\mathsf{q}_1, \mathsf{q}_2) \underset{\mathsf{q}^2 \to 0}{\sim} \tilde{A} \, \epsilon^{+\lambda-\beta} \frac{\mathsf{q}_{2\beta} \; \mathsf{q}_{1-} \mathsf{q}_1^+}{\mathsf{q}^2} \sim \tilde{A} \, \mathsf{q}_2^\beta \frac{\mathsf{p}^2}{\mathsf{q}^2} \sim \tilde{A} \, \frac{\mathsf{p}^2}{\mathsf{q}} \qquad (A.6)$$

Note that if we leave the spacelike momenta unchanged but instead choose

$$\mathsf{q}_1^\mu = \mathsf{q}_1^- = \mathsf{q}_{1+} = \mathsf{p} \not\to 0 \, , \quad \mathsf{q}_1^+ = \mathsf{q}_{1-} = 0 \qquad (A.7)$$

then we obtain

$$\Gamma^{--\lambda}(\mathsf{q}_1, \mathsf{q}_2) \underset{\mathsf{q}^2 \to 0}{\sim} \tilde{A} \, \epsilon^{-\lambda+\beta} \frac{\mathsf{q}_{2\beta} \; \mathsf{q}_{1+} \mathsf{q}_1^-}{\mathsf{q}^2} \sim - \tilde{A} \, \frac{\mathsf{p}^2}{\mathsf{q}} \qquad (A.8)$$

The change of sign compared to (A.6) has very important consequences for our discussion of the cancellation of the anomaly in Sections 4 and 7. Clearly we could equally well have changed the sign of $\mathbf{q}_{2\beta}$ while keeping the same light-cone space component. In either case there is a form of parity transformation involved and the antisymmetry of the anomaly is a direct consequence of the chirality violation discussed below. Note that the structure of the anomaly divergence involves each of the four dimensions of Minkowski space in distinct roles. This is, in part, why a triple-Regge limit which fully utilises all four dimensions is necessary to see the anomaly appear.

[‡‡] In 't Hooft's solution[21] of the U(1) problem, instantons produce a quark interaction (an η' mass term) that moves the "perturbative" η' pole away from $\mathsf{q}_1^2 = 0$. In our regge limit analysis, it is not clear how such an interaction could contribute.

The infra-red behavior (A.6) arises directly from a combination of normal thresholds and the Landau triangle singularity (or anomalous threshold) in the quark triangle diagram shown in Fig. A2, i.e.

$$\Gamma^{\mu\nu\lambda}(\mathbf{q}_1,\mathbf{q}_2) = i\int \frac{d^4k\ Tr\{\gamma_5\gamma^{\mu}\ \not{k})\ \gamma_5\gamma^{\nu}\ (\not{\mathbf{q}}_2+\not{k})\ \gamma_5\gamma^{\lambda}\ (-\not{\mathbf{q}}_1+\not{k})\}}{k^2(\mathbf{q}_2+k)^2(k-\mathbf{q}_1)^2} \qquad (A.9)$$

The triangle diagram singularity can be thought of as due to a space-time scattering as indicated by the arrows in Fig. A2. $\mathbf{q}_2$ is a spacelike momentum transfered by the $J^{a\nu}$ current and $\mathbf{q}_1$ has the light-like component necessary to produce an initial pair of massless particles.

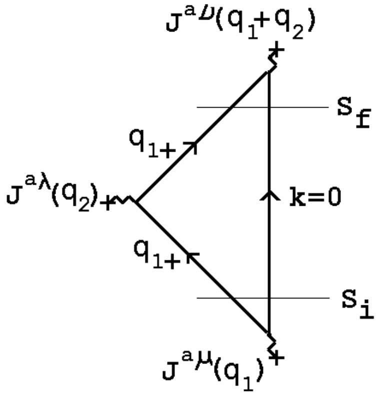

Fig. A2 The Triangle Diagram

Therefore, the vertices where the lightlike momenta enters and leaves are respectively associated with the production and annihilation of a pair of massless fermions.

When $q_1^2 \sim (q_1+q_2)^2 \rightarrow 0$ all momenta become parallel and the thresholds at $q_1^2=0$ and $(q_1+q_2)^2=0$ can enhance the triangle singularity. However, when the helicities of the fermions are determined[10] it is found that the situation is symmetric in that in both intermediate states (the produced and annihilated states) there is a net fermion chirality, i.e. a fermion/antifermion state with the same sign center-of-mass helicities (opposite sign spin components). The axial-vector coupling implies that the two possible alignments for the helicities involved give contributions that add rather than cancel, as they would do for a vector coupling (i.e. for a vector coupling intermediate states with non-zero chirality are not present). Since the spacelike current $J^{a\lambda}$ flips the helicity of the fermion that it scatters, the unscattered fermion must also flip it's helicity. This is only possible if this fermion carries strictly zero momentum so that it's helicity is undefined (as is indeed the case[10]). The finite light-like momentum is carried by the scattered fermion. That the unscattered fermion carries zero momentum implies that both propagator poles are involved in producing (A.6), thus allowing the chirality transition.

In effect the coincindence of both propagator poles for a zero momentum fermion and the resulting chirality transition is the essence of the infra-red occurrence of the anomaly. It is the chirality transition that produces the pseudotensorial asymmetry with respect to light-cone components discussed above. It is also the "chirality violation" that we refer to often in the main text. Clearly the alignment of helicities producing this violation has to be an asymptotic effect of the multi-regge limit, which is not present at finite momentum. The antisymmetry in going from (A.6) to (A.8) is the feature that we expect to lead to cancellation of the anomaly, unless there is some background asymmetry accompanying the reggeon interaction.

Coleman and Grossman also argued for the infra-red equivalent of the "non-renormalization" theorem that holds for the ultra-violet manifestation of the anomaly. They argued that Feynman diagrams with a Landau singularity and helicity structure other than that of the triangle diagram with a chirality transition, can not reproduce the behaviour (A.6). In our case the reggeon vertices we obtain will not contain the full Lorentz tensor amplitude (A.9) but rather will contain only particular light-cone related momenta and γ-matrix components. We will show, however, that we do have all the necessary components to produce the infra-red divergence (A.6). The argument of Coleman and Grossman then determines that the infra-red divergence we find can not be canceled by the contribution of other diagrams to the reggeon vertices we discuss.

It will also be important for our analysis to discuss the momenta k involved in generating the pole at $\mathbf{q}^2 = 0$ in (A.9). The numerator in (A.9) gives directly the numerator in (A.6) and so we can write

$$\Gamma^{++\lambda}(\mathbf{q}_1, \mathbf{q}_2) \underset{\mathbf{q}^2 \to 0}{\sim} \tilde{A}\, \epsilon^{+\lambda-\beta}\ \mathbf{q}_{2\beta}\ {\mathbf{q}_+}^2 \int \frac{d^4k}{k^4(k^2 - \mathbf{q}_+ k_-)} \qquad (A.10)$$

Superficially this integral depends on $\mathbf{q}_+$ and so might be expected to be $O(1/\mathbf{q}\mathbf{q}_+)$. However, it is straightforward to make the scaling

$$k_+ \ \to\ \Lambda\, k_+\ , \qquad k_-\ \to\ \Lambda^{-1}\, k_- \qquad (A.11)$$

so that

$$\int \frac{d^4k}{k^4(k^2 - \mathfrak{q}_+ k_-)} = \int \frac{dk_+ dk_- d^2k_\perp}{k^4(k^2 - \mathfrak{q}_+ k_-)} \to \int \frac{d^4k}{k^4(k^2 - \mathfrak{q}_+ k_-/\Lambda)} \qquad (A.12)$$

showing that the integral is independent of $\mathfrak{q}_+$. (In the limit $\Lambda \to \infty$ the $\mathfrak{q}_+$ dependence can be scaled out of the integral altogether, the only trace being the location of the integration contour.) Therefore we can write

$$\int \frac{d^4k}{k^4(k^2 - \mathfrak{q}_+ k_-)} \sim \int \frac{d^4k}{k^6} \sim \frac{1}{\mathfrak{q}^2} \qquad (A.13)$$

and take all components of k to be $O(\mathfrak{q})$.

Appendix B. Light Cone Kinematics

Regge limits are conventionally related to light-cone momenta by writing a general 4-momentum $p^\mu = (p_0, p_1, p_2, p_3)$ in the form

$$p^\mu = \tfrac{1}{2}\, p_{1^+}\, \underline{n}_{1^+} + \tfrac{1}{2}\, p_{1^-}\, \underline{n}_{1^-} + \underline{p}_{1\perp} \qquad (B.1)$$

where $\underline{n}_{1^+} = (1,1,0,0)$ and $\underline{n}_{1^-} = (1,-1,0,0)$ are and $\underline{p}_{1\perp}$ is a two-dimensional "transverse momentum" orthogonal to both $\underline{n}_{1^+}$ and $\underline{n}_{1^-}$. It is simple to determine that

$$p_{1^+} = p_0 + p_1 \ , \quad p_{1^-} = p_0 - p_1 \ , \quad \underline{p}_{1\perp} = (p_2, p_3) \qquad (B.2)$$

We regard $\underline{n}_{1^+}$ as euclidean vectors and form Minkoski space products by introducing

$$p_\mu = \tfrac{1}{2}\, p_{1^+}\, \underline{n}_{1^-} + \tfrac{1}{2}\, p_{1^+}\, \underline{n}_{1^-} - \underline{p}_{1\perp} \qquad (B.3)$$

The euclidean product $p^\mu p_\mu$ then, as usual, gives the Minkowski product. Clearly we can similarly define $p_{2^+}, p_{2^-}, \underline{p}_{2\perp}$ and $p_{3^+}, p_{3^-}, \underline{p}_{3\perp}$ by, respectively, projecting on vectors $\underline{n}_{2^+} = (1,0,1,0)$ and $\underline{n}_{2^-} = (1,0,-1,,0)$ or vectors $\underline{n}_{3^+} = (1,0,0,1)$ and $\underline{n}_{3^-} = (1,0,0,-1,)$.

In this paper we make use of alternative, but formally parallel, decompositions of the form

$$p^\mu = p_{2^-}\, \underline{n}_{1^+} + p_{1^-}\, \underline{n}_{2^+} + \underline{p}_{12+} \qquad (B.4)$$

where $\underline{p}_{12+}$ is now a two-dimensional vector orthogonal to both $\underline{n}_{1^+}$ and $\underline{n}_{2^+}$. This determines that

$$\underline{p}_{12+} = p_{12-}\, \underline{n}_{12+} + p_3\, \underline{n}_3 \ , \qquad p_{12-} = p_1 + p_2 - p_0 \qquad (B.5)$$

where $\underline{n}_{12+} = (1,1,1,0)$ and $\underline{n}_3 = (0,0,0,1)$ are again euclidean vectors. We can also write

$$p_\mu \;=\; p_{2-}\;\underline{n}_{1-} \;+\; p_{1-}\;\underline{n}_{2-} \;+\; p_{12-}\underline{n}_{12-} - p_3\underline{n}_3 \qquad (B.6)$$

where $\underline{n}_{1-} = (1,-1,0,0)$, $\underline{n}_{2-} = (1,0,-1,0)$. and $\underline{n}_{12-} = (1,-1,-1,0)$. $p^\mu p_\mu$ is, of course, again the Minkowski product and if $\underline{q}$ is a second four-momentum

$$p \cdot q \;=\; p^\mu q_\mu \;=\; p_{1-}q_{2-} \;+\; p_{2-}q_{1-} \;-\; p_{12-}q_{12-} \;-\; p_3 q_3 \qquad (B.7)$$

The analagous decomposition to (B.4) for γ-matrices is

$$\begin{aligned} \gamma^\mu \;&=\; \gamma_{2-}\;\underline{n}_{1+} \;+\; \gamma_{1-}\;\underline{n}_{2+} \;+\; \underline{\gamma}_{12+} \\ &=\; \gamma_{2-}\;\underline{n}_{1+} \;+\; \gamma_{1-}\;\underline{n}_{2+} \;+\; \gamma_{12-}\;\underline{n}_{12-} \;+ \gamma_3\;\underline{n}_3 \end{aligned} \qquad (B.8)$$

where

$$\begin{aligned} &\gamma_{1-} = \gamma_0 - \gamma_1\;, \quad \gamma_{2-} = \gamma_0 - \gamma_2\;, \\ &\gamma_{12-} = \gamma_1 + \gamma_2 - \gamma_0 \end{aligned} \qquad (B.9)$$

Similarly

$$\gamma_\mu \;=\; \gamma_{2-}\;\underline{n}_{1-} \;+\; \gamma_{1-}\;\underline{n}_{2-} \;+\; \gamma_{12-}\underline{n}_{12-} - \gamma_3\underline{n}_3 \qquad (B.10)$$

The γ-matices introduced in this way then satisfy

$$\begin{aligned} &\gamma_{1-}^2 \;=\; \gamma_{2-}^2 \;=\; 0\;, \qquad \gamma_{12-}^2 \;=\; \gamma_3^2 \;=\; -1\;, \\ &\gamma_{1-}\gamma_{2-} \;+\; \gamma_{2-}\gamma_{1-} \;=\; 2\;, \qquad \gamma_3\gamma_{1-} \;+\; \gamma_{1-}\gamma_3 \;=\; 0\;, \\ &\gamma_3\gamma_{2-} \;+\; \gamma_{2-}\gamma_3 \;=\; \gamma_{12-}\gamma_{1-} \;+\; \gamma_{1-}\gamma_{12-} \;=\; 0\;, \\ &\gamma_{12-}\gamma_{2-} \;+\; \gamma_{2-}\gamma_{12-} \;=\; \gamma_{12-}\gamma_3 \;+\; \gamma_3\gamma_{12-} \;=\; 0\;. \end{aligned} \qquad (B.11)$$

Clearly all the usual algebraic properties of both four-momenta and γ-matrices in terms of conventional light-cone coordinates are the same in the "new light-cone coordinates".

For our discussion of the anomaly it is useful to note that the ϵ-tensor can also be expressed in the new co-ordinates, i.e. we can write

$$\epsilon^{\mu\nu\gamma\delta}P_\mu Q_\nu R_\gamma S_\delta \;=\; p_{2-}q_{1-}r_{12-}s_3 \;-\; p_{1-}\;q_{2-}\;r_{12-}\;s_3 \;+\; \cdots$$

where there is a term corresponding to each permutation of $(2^-, 1^-, 12-, 3)$, with the sign determined by the usual antisymmetry property of the ϵ-tensor.

Finally we note that we can use any two (non-parallel) light-cone momenta and introduce appropriate "light-cone co-ordinates". In particular we can obviously choose n_{1^+} and n_{3^+}, or n_{2^+} and n_{3^+}, instead of n_{1^+} and n_{2^+} , and trivially repeat all of the above discussion.

Appendix C. Regge Limit Calculations

In this Appendix we discuss some simple Regge limit calculations using the light-cone variables introduced in the previous Appendix. We consider first two quarks scattering via single gluon exchange as illustrated in Fig. C1.

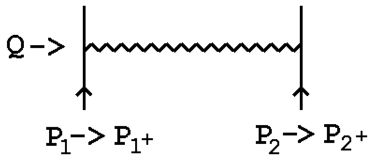

Fig. C1 Single Gluon Exchange

We consider the Regge limit in which

$$\begin{aligned} P_1 &\rightarrow\ P_{1+} = p_{12-}\ \underline{n}_{1+}\ , \qquad p_{12-} \rightarrow \infty \\ P_2 &\rightarrow\ P_{2+} = p_{21-}\ \underline{n}_{2+}\ , \qquad p_{21-} \rightarrow \infty \\ Q &\rightarrow\ \underline{Q}_{12+} \end{aligned} \tag{C.1}$$

This is, perhaps, a counter-intuitive way to discuss high-energy forward scattering. Nevertheless, we can proceed in complete parallel with conventional calculations.

The spinor $\psi(P)$ for an on-shell quark satisfies

$$\begin{aligned} m\ \psi(P)\ &=\ (\ p_{2-}\gamma_{1-} + p_{1-}\gamma_{2-} - \underline{p}_{12+}\cdot\underline{\gamma}_{12+})\ \psi(P) \\ &\underset{P \rightarrow P_{1+}}{\longrightarrow}\quad p_{2-}\ \gamma_{1-}\ \psi(p) \end{aligned} \tag{C.2}$$

Therefore the vertex for such a fast quark to couple to a single gluon carrying momentum transfer $\underline{Q}_{12+}$ is given by

$$\begin{aligned} \frac{p_{2-}\gamma_{1-}}{m}\ \gamma_\mu\ \frac{(p_{2-}\gamma_{1-} - \underline{Q}_{12+}\cdot\underline{\gamma}_{12+})}{m} \ &=\ \frac{p_{2-}\gamma_{1-}}{m}\left(\frac{p_{2-}}{m}\ \delta_{2-,\mu}\ -\ \frac{\gamma_\mu\ \underline{Q}_{12+}\cdot\underline{\gamma}_{12+}}{m}\right) \\ &=\ \frac{p_{2-}}{m}\ \delta_{2-,\ \mu}(1\ +\ O(1/p_{2-})) \end{aligned} \tag{C.3}$$

where we have used the formulae of Appendix B and have reused (C.2) to obtain the last equality. Using this result for the P_1 vertex and the analagous result for the P_2 vertex, we obtain the familiar result for the full amplitude

$$A(s,t)\ \underset{s\rightarrow\infty}{\sim}\ \frac{p_{12-}\ g^{2^-,1^-}\ p_{21-}}{Q^2}\ \sim\ \frac{s}{t} \tag{C.4}$$

Moving on to the two-gluon exchange diagram illustrated in Fig. C2,

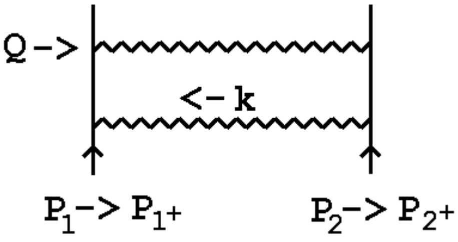

Fig. C2 Two Gluon Exchange

we calculate the imaginary part by first writing

$$\int d^4k \;=\; \int dk_{1^-}dk_{2^-}d^2\underline{k}_{12+} \tag{C.5}$$

Then, for the internal quark propagator along which P_1 flows, we write

$$\begin{aligned}\frac{\gamma\cdot(P+k)+m}{(P+k)^2-m^2} \quad &\underset{p_{2^-}\,\to\,\infty}{\sim} \quad \frac{\gamma_{1^-}p_{2^-}+\cdots}{2p_{2^-}k_{1^-}-\underline{k}^2_{12+}-m^2}\\ &\equiv \quad \frac{\gamma_{1^-}\,+\,0(1/p_{2^-})}{\left[k_{1^-}-(\underline{k}^2_{12+}-m^2)/p_{2^-}\right]}\end{aligned} \tag{C.6}$$

Putting this quark on-shell by performing the k_{1-} integration, the vertex for two gluons to couple to the fast quark is then

$$\frac{p_{12^-}\gamma_{1^-}}{m}\,(\gamma_\mu\;\gamma_{1^-}\;\gamma_\nu)\,\frac{p_{12^-}\gamma_{1^-}}{m} \;=\; \frac{p_{12^-}}{m}\,\delta_{2^-,\mu}\,\delta_{2^-,\nu} \tag{C.7}$$

where we have again used (C.2). The essential feature here, is that the infinite momentum limit leads to the exchange of gluons that will couple to a second scattering quark with a γ_{1^-} -coupling only. Note that this feature would be the same if we had used conventional light-cone co-ordinates (or, in fact, any other light-cone co-ordinates).

Using the analagous result for $P_2\to P_{2^+}$, to perform the k_{2^-} integration, the kinematic part of the full result, is

$$p_{12^-}\delta_{2^-,\mu}\delta_{2^-,\nu}g^{\mu\alpha}g^{\nu\beta}\delta_{\alpha,1^-}\delta_{\beta,1^-}{p'}_{21^-}\int\frac{d^2\underline{k}_{12+}}{\underline{k}^2_{12+}(\underline{k}_{12+}+\underline{Q}_{12+})^2} = s\int\frac{d^2\underline{k}_{12+}}{\underline{k}^2_{12+}(\underline{k}_{12+}+\underline{Q}_{12+})^2} \tag{C.8}$$

showing that the familiar tranverse momentum integral is simply replaced by an integral over the new "transverse momentum" $\underline{k}_{12+}$. Since

$$\int \frac{d^2\underline{k}_{12+}}{\underline{k}_{12+}^2(\underline{k}_{12+}+\underline{Q}_{12+})^2} = J_1(Q^2) = \int \frac{d^2\underline{k}}{\underline{k}^2(\underline{k}+\underline{Q})^2} \qquad (C.9)$$

this is a relatively trivial modification. Nevertheless is important for the arguments made in the body of the paper that the same result is clearly obtained whatever light-cone co-ordinates are used.

It is also interesting to calculate the Regge limit of Fig. B2 keeping P_2 finite. In this case the choice of "light-cone co-ordinates" is not determined by the large momenta in the problem, since there is only one. We can equally well use the conventional choice (B.3), or the novel co-ordinates utilised above. In either case we can arrive rapidly at the correct answer by arguing as follows. We again use (C.6) to perform one longitudinal momentum integration (k_{1^-}). The two exchanged gluons then couple to the P_2 quark via

$$\gamma_{1^-}\, \frac{\gamma\cdot(P_2-k)}{(P_2-k)^2-m^2}\, \gamma_{1^-} = \gamma_{1^-}\, \frac{\gamma_{1^+}(P_2-k)_{1^-} \ + \ \cdots}{k_{1^+}(P_2-k)_{1^-} \ + \ \cdots}\, \gamma_{1^-} = \frac{\gamma_{1^-}}{(k_{1^+} \ + \ \cdots)}$$

or

$$= \gamma_{1^-}\, \frac{\gamma_{2^-}(P_2-k)_{1^-} \ + \ \cdots}{k_{2^-}(P_2-k)_{1^-} \ + \ \cdots}\, \gamma_{1^-} = \frac{\gamma_{1^-}}{(k_{2^-} \ + \ \cdots)} \qquad (C.10)$$

in either case, we use this last pole to carry out a second longitudinal momentum integration (k_{1^+} or k_{2^-}) and obtain the corresponding two-dimensional transverse integral. (Whether k_{1^+} or k_{2^-} is used, the exchanged gluon propagators become independent of this variable as $P_1 \to P_{1^+}$.) We then use the Dirac equation, as in (C.2), to write either

$$\gamma_{1^-} = \gamma_{1^-}\, \frac{\gamma\cdot p}{m} = p_{1^+}/m \ + \ \cdots \qquad (C.11)$$

or

$$\gamma_{1^-} = \gamma_{1^-}\, \frac{\gamma\cdot p}{m} = p_{1^-}/m \ + \ \cdots \qquad (C.12)$$

and argue that only the first term, shown explicitly, is capable of forming a Lorentz invariant with the momentum of the fast quark. The result is then either the conventional transverse momentum integral or (C.8). We conclude that when a fast quark scatters off a quark carrying finite momentum we can calculate using any light-cone co-ordinates. The result will be the same, but will be expressed in terms of transverse momenta that depend on the co-ordinates chosen.

We consider next some double-Regge and triple-regge amplitudes. The main results are not used directly in the text but they are instructive and some of the intermediated results are used. We briefly discuss the kinematics of single particle (gluon) production first. We can parallel our elastic scattering discussion using the notation of Fig. C3.

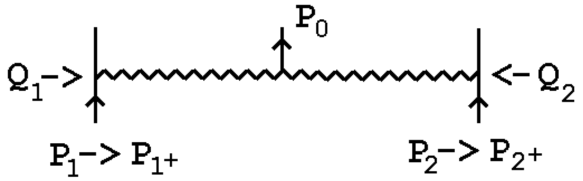

Fig. C3 Double Regge Kinematics

We take $P_1 \rightarrow P_{1+}$ and $P_2 \rightarrow P_{2+}$ as before and also

$$\begin{aligned} Q_1 &\rightarrow (q_{11-}, q_{12-}, q_{112-}, q_{13}) \ \equiv (q, 0, \tilde{q}, q_{13}) \\ Q_2 &\rightarrow (q_{21-}, q_{22-}, q_{212-}, , q_{23}) \ \equiv (0, q, -\tilde{q}, q_{23}) \end{aligned} \qquad (C.13)$$

with $P_0 = Q_1 + Q_2$. In this notation we have six independent variables, $p_{2-}, p'_{1-}, q, \tilde{q}, q_{13}$ and q_{23}. The necessary reduction to five variables is achieved by putting P_0 on mass-shell. This determines q in terms of q_{13} and q_{23}.

Consider now the double-regge amplitude shown in Fig. C4 for producing a quark-antiquark pair via gluon exchange.

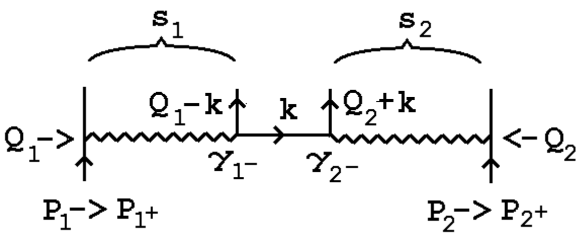

Fig. C4 Quark-antiquark Production in the Double-Regge Limit

We define $\underline{k}$ to be the four-momentum flowing along the exchanged quark propagator and use the same notation for Q_1 and Q_2 as in (C.13), except that we take $q_{11-} \neq q_{22-}$. We can then fix both of q_{11-} and q_{22-} by putting both produced particles on shell.

By applying (C.2) to the fast particles we determine that, as illustrated, the gluons couple to the quark-antiquark pair via γ_{1-} and γ_{2-} couplings. This implies that only the transverse part of the exchanged quark propagator contributes, i.e.

$$\gamma_{1^-} \ \frac{\underline{k} \cdot \underline{\gamma} - m}{\underline{k}^2 - m^2} \ \gamma_{2^-} \quad = \quad \gamma_{1^-} \ \frac{- \ \underline{k} - 12+ \cdot \underline{\gamma} 12+ - m}{k^2 - m^2} \ \gamma_{2^-} \qquad (C.14)$$

The full amplitude for Fig. C4 is then

$$A(p_{12-},p_{21-},\tilde{q},q_{13},q_{23},\underline{k}_{12+},k_{1-}k_{2-}) = \frac{p_{12-}p_{21-}\ \gamma_{1-}\ (-\underline{k}_{12+}\cdot\underline{\gamma}_{12+}-m)\ \gamma_{2-}}{m^2(\tilde{q}^2+q_{13}^2)(\tilde{q}^2+q_{23}^2)(k^2-m^2)} \quad (C.15)$$

As must be the case, the amplitude is a function of eight independent variables.

To extract an amplitude expressed in terms of invariants consider, in particular, the case in which the produced quark and antiquark spin dependence contributes similarly to (C.2), i.e. we write

$$\begin{aligned} m\ \bar{\psi}(Q_1-k) &= k_{1-}\ \gamma_{2-}\ \bar{\psi}(Q_1-k)\ +\ \cdots \\ m\ \psi(Q_2+k) &= k_{2-}\ \gamma_{1-}\ \psi(Q_2+k)\ +\ \cdots \end{aligned} \quad (C.16)$$

and keep only the spinor components shown explicitly. In this case the production amplitude of Fig. C4 has the simple form

$$\frac{s\ s'}{m^2Q_1^2Q_2^2}\ \ \frac{-\ \underline{k}_{12+}\cdot\underline{\gamma}_{12+}-m}{(k^2-m^2)} \quad (C.17)$$

Note that with the polarizations of the produced pair given by (C.16), the diagram of Fig. C5 does not contribute.

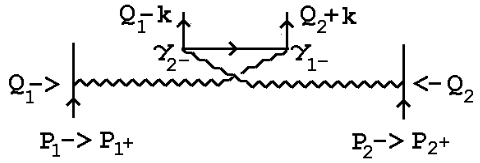

Fig. C5 An Alternative Gluon Coupling

A reggeon Ward identity requires that when all diagrams are summed the central reggeon amplitude (contained in the square brackets of (C.17)) should vanish when either Q_1 or Q_2 vanish. This is achieved by adding the three diagrams of Fig. C6.

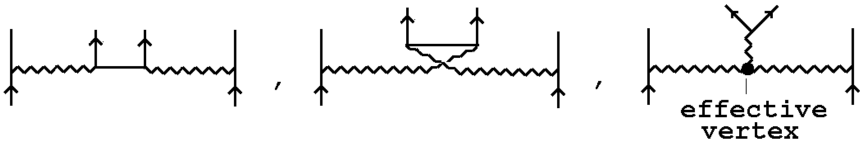

Fig. C6 Diagrams Required for the Reggeon Ward Identity.

The third diagram involves an effective regge limit vertex[7] rather than the gauge coupling. The quark/antiquark state can be written as a sum of symmetric and antisymmetric combinations that, when color factors are introduced, respectively carry zero and octet color. The third diagram appears only in the color octet channel. For the special polarizations given by (C.16) it directly cancels the first when Q_1 or $Q_2 \to 0$.

Consider next the diagram of Fig. C7 in which an additional gluon is exchanged in the Q^2 channel.

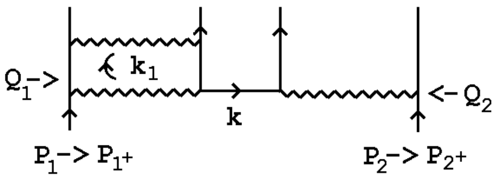

Fig. C7 An Additional Gluon Exchanged

We can calculate the discontinuity in s_1, or simply carry out two longitudinal integrations, by repeating the analysis that we applied to Fig. C2, we obtain

$$A(p_{12-}, p_{21-}, \tilde{q}, q_{13}, q_{23}, \tilde{\underline{k}}_{\perp}, k_{1-}k_{2-})$$
$$= \frac{p_{12-}p'_{21-}}{m^2Q_2^2} \int \frac{d^2\underline{k}_{112+}}{\underline{k}^2_{112+}(\underline{k}_{112+} - \underline{Q}_{12+})^2} \frac{\gamma_{1-}(-\underline{k}_{12+} \cdot \underline{\gamma}_{12+} - m)\gamma_{2-}}{(k^2 - m^2)}$$
$$= \frac{p_{12-}p_{21-}}{m^2Q_2^2} J_1(Q_1^2) \; \frac{\gamma_{1-}(-\underline{k}_{12+} \cdot \underline{\gamma}_{12+} - m)\gamma_{2-}}{(k^2 - m^2)} \qquad (C.18)$$

Comparing with (C.15), we see that the additional gluon has simply replaced one gluon transverse momentum propagator by a transverse momentum integral. The integral also has a γ_{1-} "point-coupling" to the central vertex. The pointlike nature of this coupling is, of course, essential if Fig. C7 is to be added to Fig. C3 and the $J_1(Q_1^2)$ is to produce the reggeization of the gluon in the Q_1^2 channel. However, there will also be a pointlike coupling when the quantum numbers in the Q^2 channel are such that each of the two gluons involved in the loop integral in Fig. C7 reggeize separately and the two reggeon cut appears.

If the additional gluon is attached to the outgoing quark as in Fig. C8 (rather than to the antiquark as in Fig. C7) then we no longer obtain a point-coupling for the two-gluon exchange in the Q_1 channel.

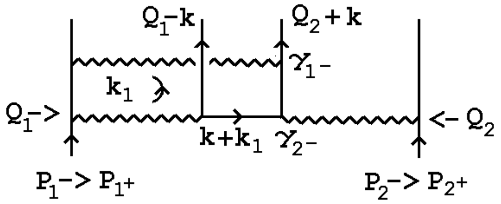

Fig. C8 An Additional Gluon Exchange Giving no Point Coupling.

The contribution of the on mass-shell hatched quark line and the adjacent γ-couplings to the k_1 integral is now

$$
\begin{aligned}
&\int dk_{12^-}\ \delta\Big((k_1+k+Q_2)^2-m^2\Big)\gamma_{2^-}\ \Big((k_1+k+Q_2)\cdot\gamma-m\Big)\ \gamma_{1^-}\\
&=\int dk_{12^-}\ \delta\Big(k_{12^-}(k_1+k+Q_2)_{1^-}\ \cdots\Big)\gamma_{2^-}\ \Big(-\ (\underline{k}_{112+}+\underline{k}_{12+}+\underline{Q}_{212+})\cdot\underline{\gamma}_{12+}-m\Big)\ \gamma_{1^-}\\
&=\quad\frac{\gamma_{2^-}\ \Big(-\ (\underline{k}_{112+}+\underline{k}_{12+}+\underline{Q}_{212+})\cdot\underline{\gamma}_{12+}-m\Big)\ \gamma_{1^-}}{(k_1+k+Q_2)_{1^-}}
\end{aligned}
\qquad (C.19)
$$

We do not obtain a point-like coupling because (unlike in (C.10), for example) the argument of the δ-function contains an integrated longitudinal momentum multiplied by a momentum factor that does not multiply a γ-matrix appearing in the numerator of the propagator. The relevant part of the propagator numerator is eliminated by the surrounding γ matrices.

Finally we move on to the process that is of central interest in the main body of the paper. This is the triple Regge scattering illustrated in Fig. C9.

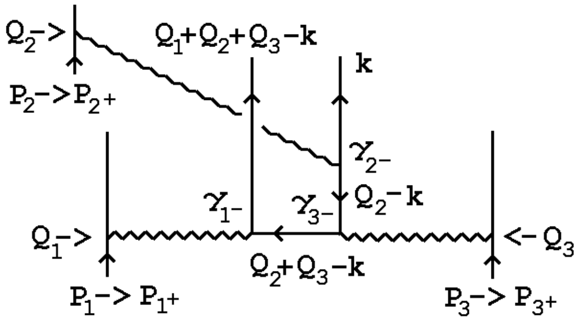

Fig. C9 A Triple Regge Amplitude.

A triple-Regge limit can be defined as $P_i\ \rightarrow P_{i+},\ i=1,2,3$ with the Q_i kept finite. We will not give a complete description of the quark-antiquark intermediate state in this limit since it will not be needed in the body of the paper. The important point for our purposes is that to directly obtain the triple discontinuities studied in Sections 5 and 6, the amplitude in Fig. C9 should be combined with another amplitude of the same form and all three of the Q_i integrated over. We do not do this in Section 6 but instead discuss only double discontinuities explicitly. However, we can make the following comment on the direct construction of triple discontinuities.

The reduction of Q_i integrations to two-dimensional integrals is achieved by using all the longitudinal integrations to put on-shell all quark lines involved in the multiple discontinuity. In particular, the internal quark propagator in Fig. C9 carrying momentum $Q_2 - k$ should be placed on-shell. If we use the Q_2 integration to put this line on-shell, and also use the 1^-,2^-, ... co-ordinates of Appendix B, the combination of the γ_{2^-} and γ_{3^-} factors with the on-shell propagator produces the effective coupling

$$\begin{aligned} &\int dQ_{21^-}\ \delta\Big(Q_{21^-}(Q_{22^-}-k_{2^-})\ -\ \cdots\Big)\ \gamma_{2^-}\ (\not{Q}_2-\not{k})\ \gamma_{3^-} \\ &= \int\ dQ_{22^-}\ \delta\Big(Q_{22^-}(Q_{21^-}-k_{1^-})\ -\ \cdots\Big)\ \gamma_{2^-}\ \Big(\gamma_{1^-}(Q_{21^-}-k_{1^-})\ -\ \cdots\Big)\ \gamma_{3^-} \\ &\qquad = \ \gamma_{2^-}\gamma_{1^-}\gamma_{3^-}\ +\ \cdots \end{aligned} \tag{C.20}$$

Using the identity

$$\gamma_\alpha\gamma_\beta\gamma_\lambda\ =\ g_{\alpha\beta}\gamma_\lambda\ +\ g_{\beta\lambda}\gamma_\alpha\ -\ g_{\alpha\lambda}\gamma_\beta + i\epsilon_{\mu\alpha\beta\gamma}\gamma^\mu\gamma_5 \tag{C.21}$$

we obtain

$$\gamma_{2^-}\gamma_{1^-}\gamma_{3^-}\ =\ \gamma_0+\gamma_1-\gamma_2-\gamma_3\ +\ i\gamma_5\ (\gamma_0+\gamma_1+\gamma_2+\gamma_3) \tag{C.22}$$

showing that the coupling (C.20) contains the effective γ_5-coupling shown in Fig. C10

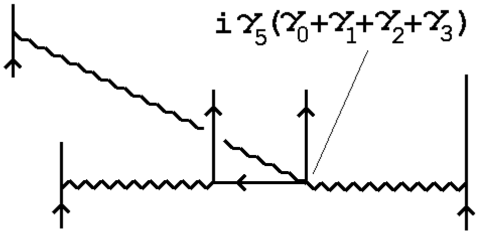

Fig. C10 The γ_5-coupling Generated by Fig. C9

This illustrates how the triple-Regge limit introduces sufficient orthogonality for the large momenta to produce an effective γ_5-coupling.

Appendix D. Angular Variables

To introduce angular variables for a six-particle amplitude it is necessary to define a set of six standard Lorentz frames $\mathcal{F}_1, \mathcal{F}_2, \mathcal{F}_3, \tilde{\mathcal{F}}_1, \tilde{\mathcal{F}}_2, \tilde{\mathcal{F}}_3$. These frames are associated with the vertices of the Toller diagram, as indicated in Fig. D1, by requiring that the momenta meeting at a vertex take a standard form. For each internal vertex there are three frames, in each of which one of the momenta lies either along the t-axis or the z-axis. As we will see, once the standard frames are defined, the angular variables parametrize "little group" Lorentz transformations between the frames.

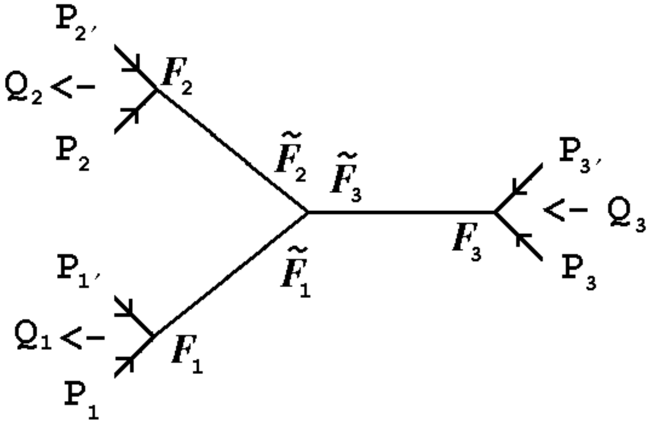

Fig. D1 Special Frames

Not surprisingly, the definition of the standard frames, together with the little groups involved (and their parametrization) depend on the physical region discussed. Since the multi-regge theory we develop in Section 5 effectively moves backwards and forwards between various t and s-channels we need to determine how the variables introduced in different channels are analytically related. For this purpose we explicitly calculate below, expressions for invariants in terms of angular variables in each of the channels we discuss. We take the mass of all external particles to be m. We can then distinguish the three t-channels and four s-channels that we study as follows. In the t_i-channel ($i = 1, 2, 3$), $|Q_i| \geq |Q_j| + |Q_k|$ ($i \neq j \neq k$) with $Q_j^2, Q_k^2 \geq 4m^2$. In the s-shannels the $t_i = Q_i^2$ are all negative. The four channels are that in which the particles with momenta P_1, P_2 and P_3 scatter, with final momenta P_1', P_2' and P_3' respectively, and those in which one of the P_i' is exchanged with the corresponding P_i.

In Fig. D2 we have shown (topographically) the three t_i-channels and one of the s-channels. In this figure, we have also indicated that a single s-channel breaks up into four distinct sub-regions. There are three "$s-t$" sub-regions in which one of the transverse momenta has longer length than the sum of the other two. In these regions the plane containing the Q_i must have a timelike component. In the "$s-s$" sub-region the Q_i satisfy euclidean inequalities and can be taken to have only spacelike components. We will discuss how the variables introduced in all regions are related by analytic continuation.

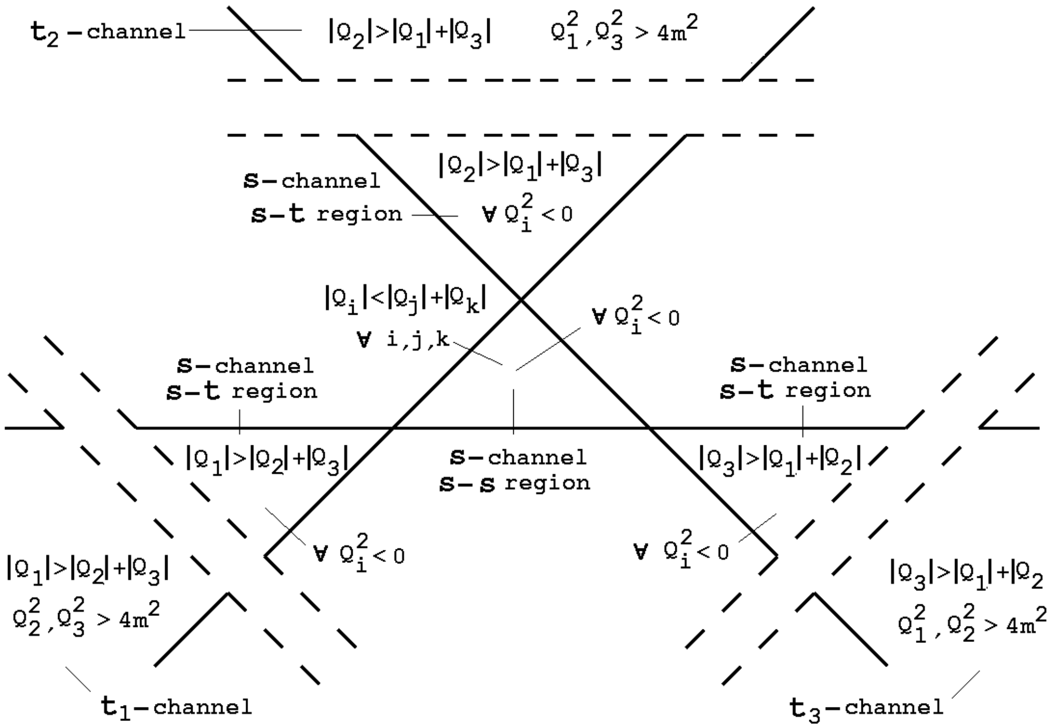

Fig. D2 Physical Regions

We consider first the t_3-channel, illustrated in Fig. D1, in which two initial state particles, 3 and $3'$, scatter into four final state particles $2, 2', 3, 3'$. In this case $Q_1^2, Q_2^2 \geq 4m^2$, $\forall i$, and $|Q_3| \geq |Q_1| + |Q_2|$. The frames $\mathcal{F}_i$, $i = 1, 2, 3$, can be defined by requiring that

$$Q_i = (Q_i, 0, 0, 0) \qquad \begin{array}{l} P_i = (m cosh\xi_i, 0, 0, m sinh\xi_i) \\ P_i' = (m cosh\xi_i, 0, 0, -m sinh\xi_i) \end{array} \qquad (D.1)$$

where $cosh\xi_i = Q_i/2m$. Clearly we could easily interchange the roles of P_i and P_i' by setting $\xi_i \to -\xi_i$ $\forall i$. As long as the theory is parity invariant, amplitudes can not depend on this choice. For frame $\tilde{\mathcal{F}}_1$ we require that

$$Q_1 = (Q_1, 0, 0, 0) \qquad \begin{array}{l} Q_2 = (Q_2 cosh\zeta_{21}, 0, 0, Q_2 sinh\zeta_{21}) \\ Q_3 = (Q_3 cosh\zeta_{31}, 0, 0, Q_3 sinh\zeta_{31}) \end{array} \qquad (D.2)$$

where

$$cosh\zeta_{21} = \frac{Q_3^2 - Q_2^2 - Q_1^2}{2Q_1Q_2} \ , \qquad cosh\zeta_{31} = \frac{Q_3^2 + Q_1^2 - Q_2^2}{2Q_1Q_3} \qquad (D.3)$$

For the frames $\tilde{\mathcal{F}}_2$ and $\tilde{\mathcal{F}}_3$ we make the analagous requirements so that in $\tilde{\mathcal{F}}_3$, for example,

$$Q_3 = (Q_3, 0, 0, 0) \qquad \begin{array}{l} Q_1 = (Q_1 cosh\zeta_{13}, 0, 0, Q_1 sinh\zeta_{13}) \\ Q_2 = (Q_2 cosh\zeta_{23}, 0, 0, Q_2 sinh\zeta_{23}) \end{array} \qquad (D.4)$$

where

$$sinh\zeta_{13} \ = \ - \, sinh\zeta_{31} \ = \ \left(\frac{(Q_3^2 + Q_1^2 - Q_2^2)^2 - 4Q_1^2Q_3^2}{4Q_1^2Q_2^2} \right)^{\frac{1}{2}} \ = \ - \, \frac{\lambda^{\frac{1}{2}}(t_1, t_2, t_3)}{2\, \sqrt{t_1}\, \sqrt{t_3}} \quad (D.5)$$

and

$$sinh\zeta_{23} \ = \ \frac{\lambda^{\frac{1}{2}}(t_1, t_2, t_3)}{2\, \sqrt{t_1}\, \sqrt{t_3}} \qquad (D.6)$$

where $\lambda(t_1, t_2, t_3)$ is the familiar function

$$\begin{aligned} \lambda(t_1, t_2, t_3) \ &= \ t_1^2 + t_2^2 + t_3^2 - 2t_1t_2 - 2t_2t_3 - 2t_3t_1 \\ &= (\sqrt{t_1} + \sqrt{t_2} + \sqrt{t_3})(\sqrt{t_1} - \sqrt{t_2} - \sqrt{t_3})(-\sqrt{t_1} + \sqrt{t_2} - \sqrt{t_3})(-\sqrt{t_1} - \sqrt{t_2} + \sqrt{t_3}) \end{aligned} \qquad (D.7)$$

Clearly we have to take opposite signs for $\lambda^{\frac{1}{2}}(t_1, t_2, t_3)$ in defining $sinh\zeta_{13}$ and $sinh\zeta_{23}$. Conversely we can reverse this sign by interchanging the form of Q_1 and Q_2 in the t_3-channel standard frames. In the next paragraph we will discuss further the ambiguity in making this choice, together with the remaining ambiguity in fixing the frames $\mathcal{F}_i$ and the frames $\tilde{\mathcal{F}}_i$. It is linked, of course, to the ambiguity in the choice of the $sinh\xi_i$.

$\tilde{\mathcal{F}}_1$ and $\mathcal{F}_1$ are related by a Lorentz transformation g_1 that leaves Q_1 unchanged, i.e. g_1 belongs to the little group of Q_1, which is $SO(3)$. We can parametrize $SO(3)$ in the form

$$g_1 = u_z(\mu_1) u_x(\theta_1) u_z(\nu_1) \qquad 0 \leq \theta < \pi \ , \ \ 0 \leq \nu, \ \mu \leq 2\pi \qquad (D.8)$$

where u_z and u_x are, respectively, rotations about the z and x axes. If we take g_1 to transform from $\mathcal{F}_1$ to $\tilde{\mathcal{F}}_1$, g_2 to transform from $\mathcal{F}_2$ to $\tilde{\mathcal{F}}_2$ and g_3 to transform from $\mathcal{F}_3$ to $\tilde{\mathcal{F}}_3$, then we can absorb the $u_z(\mu_i)$ in our definition of the frames $\mathcal{F}_i$ so that, effectively, we set $\mu_i = 0,\ i = 1,2,3$. Apart from the choice of sign for $sinh\xi_i$, this removes the remaining ambiguity in the definition of the $\mathcal{F}_i$ frames after (D.1) is satisfied. Because the $u_z(\nu_i)$ commute with the boosts $a_z(\zeta_{ij})$ along the z-axis, invariants can depend only on differences between the three ν_i - so that only two parameters are actually involved. If we insist on both the parametrization (D.8) and this last commutativity property then the $\tilde{\mathcal{F}}_i$ frames are determined up to a reflection - an overall sign change for all the $sinh\zeta_{ij}$. Again, amplitudes can not depend on this choice of sign because of parity invariance. Nevertheless, the parity transformation that produces this overall sign change plays an important role in the discussion of Section 5.

In general, to calculate invariants we transform all the momenta involved from frames in which they take a simple form to a common frame where the invariant is most easily evaluated. For.example, we transform P_1 from $\mathcal{F}_1$ to $\mathcal{F}_3$ via $\tilde{\mathcal{F}}_1$ and $\tilde{\mathcal{F}}_3$ as follows. In $\tilde{\mathcal{F}}_1$

$$P_1 = (mcosh\xi_1,\ -msinh\xi_1 sin\theta_1 sin\nu_1,\ -msinh\xi_1 sin\theta_1 cos\nu_1,\ msinh\xi_1 cos\theta_1) \quad (D.9)$$

In $\tilde{\mathcal{F}}_3$

$$\begin{aligned} P_1 = (&mcosh\xi_1 cosh\zeta_{31} - msinh\xi_1 cos\theta_1 sinh\zeta_{31},\ \ -msinh\xi_1 sin\theta_1 sin\nu_1, \\ &-msinh\xi_1 sin\theta_1 cos\nu_1,\ msinh\xi_1 cos\theta_1 cosh\zeta_{31} - mcosh\xi_1 sinh\zeta_{31}) \end{aligned} \quad (D.10)$$

In $\mathcal{F}_3$

$$\begin{aligned} P_1 = (&mcosh\xi_1 cosh\zeta_{31} - msinh\xi_1 cos\theta_1 sinh\zeta_{31}, msinh\xi_1 sin\theta_1 sin(\nu_1-\nu_3), \\ &msinh\xi_1 sin\theta_1 cos(\nu_1-\nu_3) cos\theta_3 - msinh\xi_1 cos\theta_1 cosh\zeta_{31} sin\theta_3 \\ &-mcosh\xi_1 sinh\zeta_{31} sin\theta_3,\ \ -msinh\xi_1 sin\theta_1 cos(\nu_1-\nu_3) sin\theta_3 \\ &+msinh\xi_1 cos\theta_1 cosh\zeta_{31} cos\theta_3 - mcosh\xi_1 sinh\zeta_{31} cos\theta_3) \end{aligned} \quad (D.11)$$

Alternatively we can transform P_1 to $\tilde{\mathcal{F}}_2$ and to $\mathcal{F}_2$ as follows. In $\tilde{\mathcal{F}}_2$

$$\begin{aligned} P_1 = (&mcosh\xi_1 cosh\zeta_{21} - msinh\xi_1 cos\theta_1 sinh\zeta_{21},\ \ -msinh\xi_1 sin\theta_1 sin\nu_1, \\ &-msinh\xi_1 sin\theta_1 cos\nu_1,\ msinh\xi_1 cos\theta_1 cosh\zeta_{21} - mcosh\xi_1 sinh\zeta_{21}) \end{aligned} \quad (D.12)$$

In $\mathcal{F}_2$

$$\begin{aligned} P_1 = (&mcosh\xi_1 cosh\zeta_{21} + msinh\xi_1 cos\theta_1 sinh\zeta_{21}, \ \ - msinh\xi_1 sin\theta_1 sin(\nu_1 - \nu_2), \\ &msinh\xi_1 sin\theta_1 cos(\nu_1 - \nu_2) cos\theta_2 + msinh\xi_1 cos\theta_1 cosh\zeta_{21} sin\theta_2 \\ &- mcosh\xi_1 sinh\zeta_{21} sin\theta_2, \ \ - msinh\xi_1 sin\theta_1 cos(\nu_1 - \nu_2) sin\theta_2 \\ &+ msinh\xi_1 cos\theta_1 cosh\zeta_{21} cos\theta_2 - mcosh\xi_1 sinh\zeta_{21} cos\theta_2) \end{aligned} \qquad (D.13)$$

From the above expressions for P_1 we can already calculate several invariants. In $\tilde{\mathcal{F}}_1$, for example, Q_3 has the form (D.2) and so

$$P_1.Q_3 \ = \ mQ_3 \ [cosh\xi_1 cosh\zeta_{31} - sinh\xi_1 sinh\zeta_{31} cos\theta_1] \qquad (D.14)$$

In $\mathcal{F}_3$, similarly, P_3 has the form (D.1) and so

$$\begin{aligned} P_1.P_3 \ = \ m^2 \ [&cosh\xi_1 cosh\xi_3 cosh\zeta_{31} - sinh\xi_1 cosh\xi_3 sinh\zeta_{31} cos\theta_1 \\ &- sinh\xi_1 sinh\xi_3 sin\theta_1 sin\theta_3 cos(\nu_1 - \nu_3) - sinh\xi_1 sinh\xi_3 cosh\zeta_{31} cos\theta_1 cos\theta_3 \\ &+ cosh\xi_1 sinh\xi_3 sinh\zeta_{31} cos\theta_3] \end{aligned} \qquad (D.15)$$

while, in $\mathcal{F}_2$, P_2 has the form (D.1) and so

$$\begin{aligned} P_1.P_2 \ = \ m^2 \ [&cosh\xi_1 cosh\xi_2 cosh\zeta_{21} - sinh\xi_1 cosh\xi_2 sinh\zeta_{21} cos\theta_1 \\ &- sinh\xi_1 sinh\xi_2 sin\theta_1 sin\theta_2 cos(\nu_1 - \nu_2) - sinh\xi_1 sinh\xi_2 cosh\zeta_{21} cos\theta_1 cos\theta_2 \\ &+ cosh\xi_1 sinh\xi_2 sinh\zeta_{21} cos\theta_2] \end{aligned} \qquad (D.16)$$

(D.15) and (D.16) differ only by the interchange of 1 and 2. It is straightforward to calculate all other invariants in a similar manner. If we write $z_i = cos\theta_i$ and $u_{ij} = e^{i(\nu_i - \nu_j)}$ then we can take any two of the u_{ij}, together with the z_i and the t_i, as eight independent variables.

We see from the above formulae that a change of sign of $sinh\xi_1$ is equivalent to a change of sign of both $cos\theta_1$ and $sin\theta_1$ ($\theta \rightarrow \theta + \pi$). A change of sign of the $sinh\zeta_{ij}$ is equivalent to a change of sign of all the $cos\theta_i$ which, in turn, is equivalent to a change of sign of all the $sinh\xi_i$. It is also interesting to write (D.14) and (D.15) explicitly in terms of the t_i and z_1, i.e.

$$4 \ P_1.Q_3 \ = \ t_3 + t_1 - t_2 \ - \ \left(\frac{t_1 - 4m^2}{t_1}\right)^{\frac{1}{2}} \lambda^{\frac{1}{2}}(t_1, t_2, t_3) \ z_1 \qquad (D.17)$$

and

$$\begin{aligned} 8\ P_1.P_3 \ &= \ t_3 + t_1 - t_2 \ - \ \lambda^{\frac{1}{2}}(t_1,t_2,t_3)\Big[\frac{(t_1-4m^2)^{\frac{1}{2}}}{\sqrt{t_1}}z_1 \ - \ \frac{(t_3-4m^2)^{\frac{1}{2}}}{\sqrt{t_3}}z_3\Big] \\ &- \ (t_1-4m^2)^{\frac{1}{2}}(t_3-4m^2)^{\frac{1}{2}}\Big[(1-z_1^2)^{\frac{1}{2}}(1-z_3^2)^{\frac{1}{2}}\Big(u_1+\frac{1}{u_1}\Big)+\frac{t_3+t_1-t_2}{\sqrt{t_1}\sqrt{t_3}}z_1z_3\Big] \end{aligned} \qquad (D.18)$$

From these expressions we see that we will encounter analytic continuation problems at the thresholds $t_i = 4m^2$, at $t_i = 0$, and at $\lambda(t_1,t_2,t_3) = 0$. In particular, when $t_i < 0$ and also $\lambda(t_1,t_2,t_3) < 0$ the real relationship between the z_i and the invariants is necessarily lost.

Consider now the s-channel in which $1, 2$ and 3 are the three initial state particles and consider the $s-t$ region in which $Q_i^2 < 0, \forall i$ and $|Q_3| \geq |Q_1| + |Q_2|$. The frames $\mathcal{F}_i$, $i = 1, 2, 3$ are now defined by requiring that

$$Q_i = (0,0,0,q_i) \qquad \begin{aligned} P_i &= (mcosh\xi_i, 0, 0, msinh\xi_i) \\ P_i' &= (-mcosh\xi_i, 0, 0, msinh\xi_i) \end{aligned} \qquad (D.19)$$

where $sinh\xi_i = q_i/2m$ and $q_i = |Q_i| = [-t_i]^{\frac{1}{2}}$ (so that $sinh\xi_i \equiv i\ cosh\xi_i$ if we consider the analytic continuation of $cosh\xi_i$ defined by (D.1)). The obvious redefinition of the frame $\tilde{\mathcal{F}}_1$ is to require

$$Q_1 = (0,0,0,q_1) \qquad \begin{aligned} Q_2 &= (q_2 sinh\zeta_{21}, 0, 0, q_2 cosh\zeta_{21}) \\ Q_3 &= (q_3 sinh\zeta_{31}, 0, 0, q_3 cosh\zeta_{31}) \end{aligned} \qquad (D.20)$$

where

$$cosh\zeta_{21} = \frac{q_3^2 - q_2^2 - q_1^2}{2q_1q_2}\ , \qquad cosh\zeta_{31} = \frac{q_3^2 + q_1^2 - q_2^2}{2q_1q_3} \qquad (D.21)$$

These last expressions are simple analytic continuations of the expressions given in (D.3). The frames $\tilde{\mathcal{F}}_2$ and $\tilde{\mathcal{F}}_3$ are redefined analagously. Note, however, that there is again an overall ambiguity in the choice of sign for the $sinh\zeta_{ij}$. Now the reflection involved is not a parity transformation since it applies to the time axis. If any of the Q_i were timelike and associated with a particle state (as in a normal multi-regge production process) this sign would be determined. In the present case we will see that we must use both signs to fully cover the physical region.

$\tilde{\mathcal{F}}_i$ and $\mathcal{F}_i$ are again related by a Lorentz transformation g_i that leaves Q_i unchanged, but now $g_i \in SO(2,1)$. Since the Q_i triangle has a timelike component it is simplest to use the parametrization of $SO(2,1)$ that is closely related to that used above for $SO(3)$, i.e.

$$g_1 = u_z(\mu_1)a_x(\beta_1)u_z(\nu_1) \qquad -\infty \leq \beta < \infty \quad 0 \leq \nu,\ \mu \leq 2\pi \tag{D.22}$$

where $a_x(\beta_1)$ is a boost along the x-axis. With this parametrization, we can again choose the $\mathcal{F}_i$ such that $\mu_i = 0,\ i = 1,2,3$ and the $u_z(\nu_i)$ commute with the boosts $a_z(\zeta_{ij})$.

Repeating the transformation of P_1 from $\mathcal{F}_1$ to $\mathcal{F}_3$ gives the following. In $\tilde{\mathcal{F}}_1$

$$P_1 = (mcosh\xi_1 cosh\beta_1,\ mcosh\xi_1 sinh\beta_1 cos\nu_1,\ -mcosh\xi_1 sinh\beta_1 sin\nu_1,\ msinh\xi_1) \tag{D.23}$$

In $\tilde{\mathcal{F}}_3$

$$\begin{aligned} P_1 = (&mcosh\xi_1 cosh\beta_1 cosh\zeta_{31} - msinh\xi_1 sinh\zeta_{31},\ mcosh\xi_1 sinh\beta_1 cos\nu_1, \\ &- mcosh\xi_1 sinh\beta_1 sin\nu_1,\ msinh\xi_1 cosh\zeta_{31} - mcosh\xi_1 cosh\beta_1 sinh\zeta_{31}) \end{aligned} \tag{D.24}$$

In $\mathcal{F}_3$

$$\begin{aligned} P_1 = (&mcosh\xi_1 cosh\beta_1 cosh\beta_3 cosh\zeta_{31} - msinh\xi_1 sinh\zeta_{31} cosh\beta_3 \\ &- mcosh\xi_1 sinh\beta_1 sinh\beta_3 cos(\nu_1 - \nu_3),\ - mcosh\xi_1 cosh\beta_1 sinh\beta_3 cosh\zeta_{31} \\ &msinh\xi_1 sinh\zeta_{31} sinh\beta_3 + mcosh\xi_1 sinh\beta_1 cosh\beta_3 cos(\nu_1 - \nu_3), \\ &- mcosh\xi_1 sinh\beta_1 sin(\nu_1 - \nu_3),\ msinh\xi_1 cosh\zeta_{31} - mcosh\xi_1 cosh\beta_1 sinh\zeta_{31}) \end{aligned} \tag{D.25}$$

Calculating in $\tilde{\mathcal{F}}_1$, we now obtain

$$P_1.Q_3 \ = \ mq_3\ [cosh\xi_1 sinh\zeta_{31} cosh\beta_1 - sinh\xi_1 cosh\zeta_{31}] \tag{D.26}$$

and in $\mathcal{F}_3$ (arranging terms to compare with (D.15))

$$\begin{aligned} P_1.P_3 \ = \ m^2\ [&-sinh\xi_1 sinh\xi_3 cosh\zeta_{31} + cosh\xi_1 sinh\xi_3 sinh\zeta_{31} cosh\beta_1 \\ &- cosh\xi_1 cosh\xi_3 sinh\beta_1 sinh\beta_3 cos(\nu_1 - \nu_3) \\ &+ cosh\xi_1 cosh\xi_3 cosh\zeta_{31} cosh\beta_1 cosh\beta_3 - sinh\xi_1 cosh\xi_3 sinh\zeta_{31} cosh\beta_3] \end{aligned} \tag{D.27}$$

Comparing (D.26) and (D.27) with (D.14) and (D.15) we see that, if we identify $cos\theta_i \leftrightarrow cosh\beta_i = z_i$, the two sets of formulae are directly related by analytic continuation. All terms have changed sign as a result of $cosh\xi_i/sinh\xi_i \ \rightarrow \ i\ sinh\xi_i/cosh\xi_i$ and $Q_i \rightarrow i\ Q_i$, apart from that containing $sin\theta_1 sin\theta_2$, which contains an extra minus sign via $sin\theta_i \rightarrow i\ sinh\beta_i$.

In this last discussion we have effectively made the analytic continuation choice that the $sinh\zeta_{ij}$ do not change sign, yet we have emphasized that there is an overall sign ambiguity for these quantities. To see the significance of this ambiguity we note that (calculating in frame $\tilde{\mathcal{F}}_3$ for simplicity)

$$P_3.Q_1 \;=\; mq_1 \; [cosh\xi_3 sinh\zeta_{13} cosh\beta_3 - sinh\xi_3 cosh\zeta_{13}] \qquad (D.28)$$

and

$$P_3.Q_2 \;=\; mq_2 \; [cosh\xi_3 sinh\zeta_{23} cosh\beta_3 - sinh\xi_2 cosh\zeta_{23}] \qquad (D.29)$$

where if we choose $sinh\zeta_{13}$ to be positive then we must choose $sinh\zeta_{23}$ to be negative. This in turn will imply that, for large $cosh\beta_3$, $P_3.Q_1$ is positive, while $P_3.Q_2$ is negative. However, the part of the physical region we are discussing is completely symmetric with repect to 1 and 2. Therefore, to cover the full physical region, we must take both sign conventions for the $sinh\zeta_{ij}$. This would appear to prevent the full description of s-channel physical regions using angular variables defined by analytic continuation from the t_i-channels since it implies, in particular, that we must choose both signs for $\lambda^{\frac{1}{2}}(t_1, t_2, t_3)\ z_1$ in (D.17). Fortunately, as we remarked earlier, and can be seen directly from (D.26),(D.27),(D.28), and (D.29), changing the sign of the $sinh\zeta_{ij}$ is equivalent to changing the sign of the three $z_i = cosh\beta_i$. Therefore, to cover the $s-t$ part of the s-channel that we are discussing, using z_i variables defined by anaytic continuation from a t-channel, we must use both $z_1, z_2, z_3, \geq 1$ and $z_1, z_2, z_3, \leq -1$. This is a very important point for the discussion of dispersion theory and signature in the body of the paper.

Finally we consider the $s-s$ region of the same s-channel. In this case the three Q_i lie entirely in a spacelike plane so that $Q_i^2 < 0, \forall i$ and $|Q_i| \leq |Q_j| + |Q_k| \;\; \forall\ i, j, k$. The $\mathcal{F}_i$ frames are again defined so that

$$Q_i = (0, 0, 0, q_i) \qquad \begin{array}{l} P_i = (mcosh\xi_i, 0, 0, msinh\xi_i) \\ P_i' = (-mcosh\xi_i, 0, 0, msinh\xi_i) \end{array} \qquad (D.30)$$

with $sinh\xi_i = q_i/2m$. However, the frame $\tilde{\mathcal{F}}_1$ is now defined so that

$$Q_1 = (0, 0, 0, q_1) \qquad \begin{array}{l} Q_2 = (0, 0, q_2 sin\zeta_{21}, q_2 cos\zeta_{21}) \\ Q_2 = (0, 0, q_3 sin\zeta_{31}, q_3 cos\zeta_{31}) \end{array} \qquad (D.31)$$

where

$$cos\zeta_{21} = \frac{q_2^2 + q_1^2 - q_3^2}{2q_1q_2}\ , \qquad cos\zeta_{31} = \frac{q_3^2 + q_1^2 - q_2^2}{2q_1q_3} \qquad (D.32)$$

Now there is a change of sign of $cos\zeta_{21}$ compared to the definition of $cosh\zeta_{21}$ in (D.3). Also the ambiguity in the choice of sign for the $\sin\zeta_{ij} = i\lambda^{\frac{1}{2}}(t_1, t_2, t_3)/2q_iq_j$ persists. The frames $\tilde{\mathcal{F}}_2$ and $\tilde{\mathcal{F}}_3$ are redefined analagously.

$\tilde{\mathcal{F}}_i$ and $\mathcal{F}_i$ are again related by a Lorentz transformation $g_i \in SO(2,1)$. However, to proceed as in the previous cases, we have to use a different parametrization of $SO(2,1)$, i.e.

$$g_i = u_z(\mu_i)a_y(\beta_i)a_x(\gamma_i) \qquad\qquad -\infty < \beta_i,\, \gamma_i < \infty \quad 0 \le \mu_i \le 2\pi \qquad\qquad (D.33)$$

where a_x and a_y are boosts in the $x-t$ and $y-t$ planes respectively. With this parametrization (provided we take g_i to transform from $\mathcal{F}_i$ to $\tilde{\mathcal{F}}_i$) we can once again absorb the $u_z(\mu_i)$ in our definition of the frames $\mathcal{F}_i$ and also have the $a_x(\gamma_i)$ commute with the rotations $u_x(\zeta_{21})$ and $u_x(\zeta_{31})$.

Repeating, for a final time, the calculation of P_1 in the various frames.

In $\tilde{\mathcal{F}}_1$

$$P_1 = (mcosh\xi_1cosh\beta_1cosh\gamma_1,\ mcosh\xi_1cosh\beta_1,\ mcosh\xi_1sinh\beta_1sinh\gamma_1,\ msinh\xi_1) \qquad (D.34)$$

In $\tilde{\mathcal{F}}_3$

$$\begin{aligned} P_1 = (&mcosh\xi_1cosh\beta_1cosh\gamma_1,\ mcosh\xi_1cosh\beta_1sinh\gamma_1,\ mcos\zeta_{31}cosh\xi_1sinh\beta_1 \\ &- msin\zeta_{31}sinh\xi_1, msin\zeta_{31}cosh\xi_1sinh\beta_1sinh\gamma_1 - mcos\zeta_{31}sinh\xi_1) \end{aligned} \qquad (D.35)$$

In $\mathcal{F}_3$

$$\begin{aligned} P_1 = (&mcosh\xi_1cosh\beta_1cosh\beta_3cosh(\gamma_1-\gamma_3) - msinh\beta_3cos\zeta_{31}cosh\xi_1sinh\beta_1 \\ &+ msinh\beta_3sin\zeta_{31}sinh\xi_1,\ mcosh\xi_1cosh\beta_1sinh(\gamma_1-\gamma_3), \\ &- mcosh\xi_1cosh\beta_1sinh\beta_3cosh(\gamma_1-\gamma_3) + mcosh\beta_3cos\zeta_{31}cosh\xi_1sinh\beta_1 \\ &- mcosh\beta_3sin\zeta_{31}sinh\xi_1,\ msin\zeta_{31}cosh\xi_1sinh\beta_1 - mcos\zeta_{31}sinh\xi_1) \end{aligned} \qquad (D.36)$$

The evaluation of invariants now gives, using $\tilde{\mathcal{F}}_1$,

$$P_1.Q_3 \ = \ mq_3\ [-sin\zeta_{31}cosh\xi_1sinh\beta_1 - cos\zeta_{31}sinh\xi_1] \qquad (D.37)$$

and in $\mathcal{F}_3$,

$$\begin{aligned} P_1.P_3 \ = \ m^2\ [&cosh\xi_1cosh\xi_3cosh\beta_1cosh\beta_3cosh(\gamma_1-\gamma_3) \\ &- cosh\xi_1cosh\xi_3cos\zeta_{31}sinh\beta_3sinh\beta_1 + msinh\xi_1cosh\xi_3sin\zeta_{31}sinh\beta_3 \\ &- cosh\xi_1sinh\xi_3sin\zeta_{31}sinh\beta_1 + sinh\xi_1sinh\xi_3cos\zeta_{31} \end{aligned} \qquad (D.38)$$

Now we see some more significant changes. Comparing (D.37) with (D.14) and (D.26) we see that $cosh\beta_1$ has been replaced by $sinh\beta_1$ (in conjunction with

$sinh\zeta_{31} \to sin\zeta_{31}$). We recognize that the change of sign of $\lambda(t_1, t_2, t_3)$ produced by going from the $s-t$ to the $s-s$ region has, as anticipated, destroyed the real relationship between the z_i defined in the t_i channels and invariants of the form $P_i.Q_j$, so that now $z_i \leftrightarrow isinh\beta_i$. In Fig. D3 we have shown the location of the relevant physical regions in the z_i-planes, for the various values of the t_i.

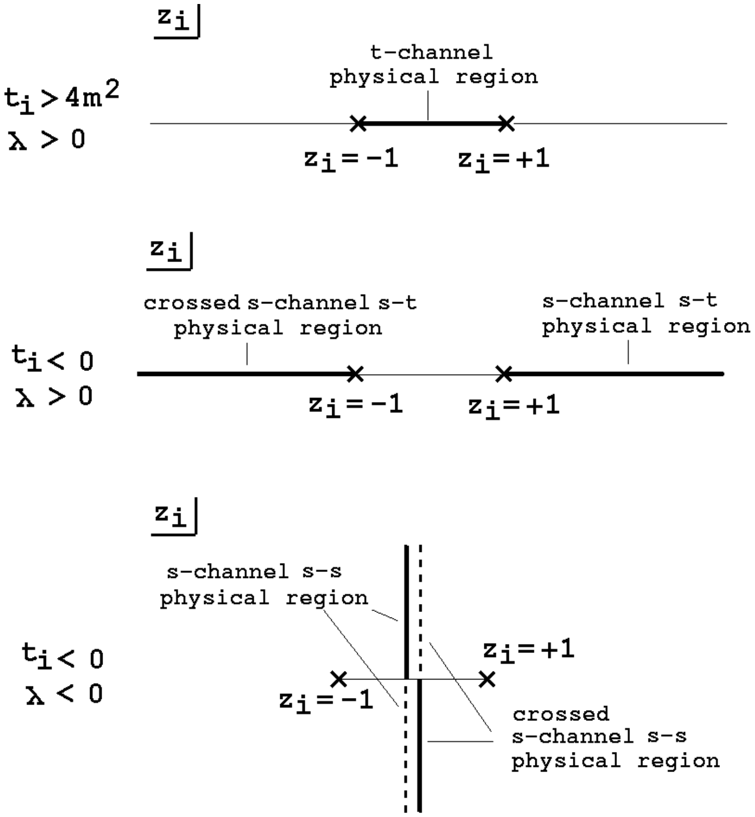
z_i
t-channel physical region
t_i > 4m^2
λ > 0
z_i = -1
z_i = +1
z_i
crossed s-channel s-t physical region
s-channel s-t physical region
t_i < 0
λ > 0
z_i = -1
z_i = +1
z_i
s-channel s-s physical region
t_i < 0
λ < 0
z_i = +1
z_i = -1
crossed s-channel s-s physical region

Fig. D3 Physical Regions in the z_i-planes

The $s-s$ part of one physical region fills the complete imaginary axis in each of the z_i-planes. However, the invariants also depend on $cosh\beta_i = \sqrt{z_i^2 - 1}$, which should change sign as we go from one s-channel physical region to a crossed physical region. This implies that, in the $s-s$ region, there are two physical sheets for each z_i-plane separated by branch-cuts connecting the branch-points at $z_i = \pm 1$. Crossing an incoming particle into an outgoing particle takes us from one sheet to the other in the corresponding z_i plane. Note that the same crossing can also be achieved by changing the sign of u_{ij} and u_{ik}, while leaving $\sqrt{z_i^2 - 1}$ unchanged. Therefore the second z_i-planes can alternatively be identified as the original z_i-plane but with a change of sign for u_{ij} and u_{ik}. (Note that if we have chosen $u_1 = u_{31} = u_{13}^{-1}$ and $u_2 = u_{23}$ as independent variables then changing the sign of u_{13} and $u_{12} = u_2/u_1$ corresponds to changing the sign of u_1 but not u_2.) This is important, of course, for the introduction of signature for complex helicity continuations. Finally we note that changing the signs of all the $sin\zeta_{ij}$ again corresponds to changing the signs of all the $cosh\beta_i$.

As we stated in Section 5, the asymptotic dispersion relation that we use should be initially written in an $s-t$ region of the s-channels. It is straightforward to continue it directly to any of the t_i channels. In the $s-s$ region it corresponds to using a combination of the upper and lower z_i half-planes (from the two sheets). Of course, that the $s-s$ physical region lies along the imaginary z_i-axes is very important for discussing the phases obtained from the S-W representation, particularly since it is only in this region that limits in which the u_{ij} are taken large (whether or not the z_i are large) are physical region limits.

References

[1] V. N. Gribov, I. Ya. Pomeranchuk and K. A. Ter-Martirosyan, *Phys. Rev.* **139B**, 184 (1965).

[2] A. R. White, Int. J. Mod. Phys. **A11**, 1859 (1991); A. R. White in *Structural Analysis of Collision Amplitudes*, proceedings of the Les Houches Institute, eds. R. Balian and D. Iagolnitzer (North Holland, 1976); H. P. Stapp ibid.

[3] E. A. Kuraev, L. N. Lipatov, V. S. Fadin, *Sov. Phys. JETP* **45**, 199 (1977).

[4] J. B. Bronzan and R. L. Sugar, *Phys. Rev.* **D17**, 585 (1978). This paper organizes into reggeon diagrams the results from H. Cheng and C. Y. Lo, Phys. Rev. **D13**, 1131 (1976), **D15**, 2959 (1977).

[5] V. S. Fadin and V. E. Sherman, Sov. Phys. JETP **45**, 861 (1978).

[6] V. S. Fadin and L. N. Lipatov, *Nucl. Phys.* **B406**, 259 (1993)

[7] V. S. Fadin and L. N. Lipatov, *Nucl. Phys.* **B477**, 767 (1996) and further references therein.

[8] J. Bartels, *Z. Phys.* **C60**, 471 (1993) and references therein.

[9] A. R. White, *Int. J. Mod. Phys.* **A8**, 4755 (1993).

[10] S. Coleman and B. Grossman, *Nucl. Phys.* **B203**, 205 (1982).

[11] P. Goddard and A. R. White, *Nucl. Phys.* **B17**, 1, 45 (1970).

[12] A. R. White, *Phys. Rev.* **D58**, 074008 (1998), see also Lectures in the Proceedings of the Theory Institute on Deep-Inelastic Diffraction, Argonne National Laboratory (1998).

[13] A. R. White, hep-ph 9910459 (ANL-HEP-PR-99-108) - to be revised.

[14] H. P. Stapp and A. R. White, *Phys. Rev.* **D26**, 2145 (1982). See also [18] below.

[15] A. A. Migdal, A. M. Polyakov and K. A. Ter-Martirosyan, *Zh. Eksp. Teor. Fiz.* **67**, 84 (1974); H. D. I. Abarbanel and J. B. Bronzan, *Phys. Rev.* **D9**, 2397 (1974).

[16] G. V. Frolov, V. N. Gribov and L. N. Lipatov, Phys. Lett. **B31**, 34 (1970), H. Cheng and T. T. Wu, Phys. Rev. Letts. **24**, 1456 (1970).

[17] I. Halliday and C. T. Sachrajda, *Phys. Rev.* **D8**, 3598 (1973).

[18] A. R. White, “The Past and Future of S-Matrix Theory”, ANL-HEP-PR-00-011, to be published in “Scattering”, edited by E. R. Pike and P. Sabatier.

[19] K. E. Cahill and H. P. Stapp *Ann. Phys.* **90**, 438 (1975).

[20] R. C. Brower, C. E. DeTar and J. H. Weis, *Phys. Rpts* **14C**, 257 (1974), C. E. DeTar and J. H. Weis, *Phys. Rev.* **D4**, 3141 (1971).

[21] G. ’t Hooft, *Phys. Rpts.* **142**, 357 (1986).

[22] G. ’t Hooft, *Nucl. Phys.* **B33**, 173 (1971).

[23] A. D. Dolgov and V. I. Zakharov, *Nucl. Phys.* **B27**, 525 (1971).

[24] G. ’t Hooft, in Recent Developments in Gauge Theories, ed. G. ’t Hooft et al. (Plenum, N.Y., 1980)

[25] T. Banks, Y. Frishman, A. Schwimmer and S. Yankielowicz, *Nucl. Phys.* **B177**, 157 (1981).

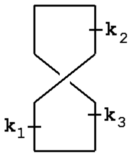

(a)

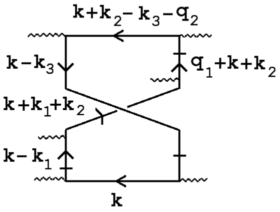

(b)

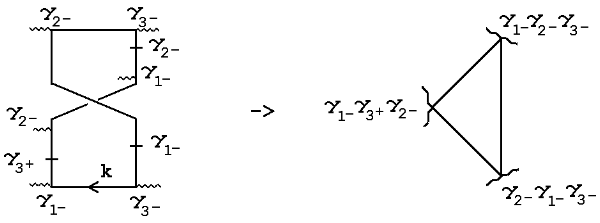

Υ2−
Υ3−
Υ2−
Υ1−
Υ2−
Υ1−
Υ3+
k
Υ1−
Υ3−
->
Υ1−Υ2−Υ3−
Υ1−Υ3+Υ2−
Υ2−Υ1−Υ3−

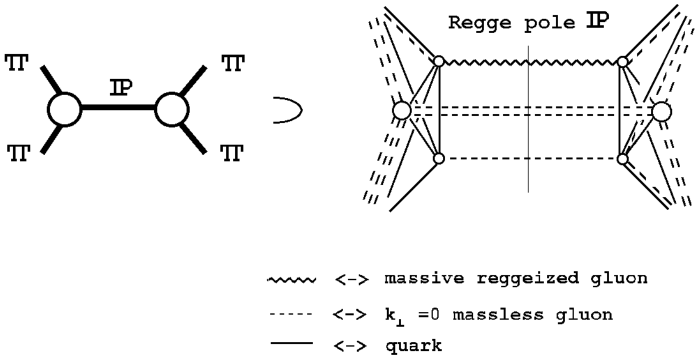
π
π
IP
π
π
⊃
Regge pole IP
<-> massive reggeized gluon
<-> $k_\perp$ =0 massless gluon
<-> quark